

Plasma deposition : investigations on a new approach

Citation for published version (APA):

Kroesen, G. M. W. (1988). *Plasma deposition : investigations on a new approach*. [Phd Thesis 1 (Research TU/e / Graduation TU/e), Applied Physics and Science Education]. Technische Universiteit Eindhoven.
<https://doi.org/10.6100/IR280381>

DOI:

[10.6100/IR280381](https://doi.org/10.6100/IR280381)

Document status and date:

Published: 01/01/1988

Document Version:

Publisher's PDF, also known as Version of Record (includes final page, issue and volume numbers)

Please check the document version of this publication:

- A submitted manuscript is the version of the article upon submission and before peer-review. There can be important differences between the submitted version and the official published version of record. People interested in the research are advised to contact the author for the final version of the publication, or visit the DOI to the publisher's website.
- The final author version and the galley proof are versions of the publication after peer review.
- The final published version features the final layout of the paper including the volume, issue and page numbers.

[Link to publication](#)

General rights

Copyright and moral rights for the publications made accessible in the public portal are retained by the authors and/or other copyright owners and it is a condition of accessing publications that users recognise and abide by the legal requirements associated with these rights.

- Users may download and print one copy of any publication from the public portal for the purpose of private study or research.
- You may not further distribute the material or use it for any profit-making activity or commercial gain
- You may freely distribute the URL identifying the publication in the public portal.

If the publication is distributed under the terms of Article 25fa of the Dutch Copyright Act, indicated by the "Taverne" license above, please follow below link for the End User Agreement:

www.tue.nl/taverne

Take down policy

If you believe that this document breaches copyright please contact us at:

openaccess@tue.nl

providing details and we will investigate your claim.

**PLASMA DEPOSITION:
INVESTIGATIONS ON A NEW APPROACH**

G.M.W. Kroesen

**PLASMA DEPOSITION:
INVESTIGATIONS ON A NEW APPROACH**

PROEFSCHRIFT

ter verkrijging van de graad van doctor aan de
Technische Universiteit Eindhoven, op gezag van
de rector magnificus, prof. dr. F.N. Hooge, voor
een commissie aangewezen door het college van
decanen in het openbaar te verdedigen op vrijdag
18 maart 1988 te 16.00 uur

door

**GERARDUS MARIA WILHELMUS
KROESEN**

geboren te Heerlen

Dit proefschrift is goedgekeurd door de promotoren

prof. dr.ir. D.C. Schram

en

prof. dr. F.J. de Hoog.

These investigations in the program of the Foundation for Fundamental Research on Matter (FOM) have been supported by the Netherlands Technology Foundation (STW).

Aan mijn ouders

CONTENTS

SUMMARY	1
1 INTRODUCTION	4
2 MODEL	7
2.1 Introduction	7
2.2 Basic equations	7
2.3 The arc plasma	11
2.3.1 Heating and ionization	11
2.3.2 Injection of methane	14
2.4 Expansion of the seeded plasma	18
2.4.1 Introduction	18
2.4.2 The nozzle	18
2.4.3 Shock wave	22
2.4.4 Subsonic relaxation	23
2.5 Deposition rates	24
3 EXPERIMENT	25
3.1 Introduction	25
3.2 The reactor	26
3.2.1 The cascaded arc	26
3.2.2 Vacuum system and gas handling	29
3.2.3 The auxiliary discharge	32
3.3 The optical system	33
3.4 Implementation of ellipsometry	37
3.4.1 Experimental setup	37
3.4.2 Data reduction	41

4	DIAGNOSTICS	44
4.1	Introduction	44
4.2	Plasma diagnostics	44
4.2.1	Broadening and shift of spectral lines	44
4.2.2	Line to continuum ratio	46
4.2.3	Plasma conductivity	47
4.3	Ellipsometry	49
4.3.1	Reflection of light on stratified structures	49
4.3.2	Fundamentals of the setup	52
5	RESULTS AND DISCUSSION	56
5.1	Introduction	56
5.2	The cascaded arc	57
5.3	The expansion	70
5.4	<i>In-situ</i> ellipsometry	82
5.5	Film quality	87
6	CONCLUSIONS	94
	REFERENCES	98
	SAMENVATTING	104
	DANKWOORD	107
	CURRICULUM VITAE	110

SUMMARY

Since about 20 years plasmas are of an increasing importance in a number of industrial processes. In many cases these processes are applied for the processing of surfaces of substrates. One of these processes is plasma deposition. This technique, which involves the growth of a thin film of a certain material on a substrate, is distinctly different from the more conventional chemical vapour deposition (CVD) processes. In CVD the original material (mostly a gas mixture) is dissociated by pyrolysis at heated substrates, whereas in plasma deposition this is done by electron impact. In most cases an RF or DC glow discharge is used. The disadvantage of these two configurations is that one discharge has to provide for three functions: dissociation and ionization of the original material, transport of the produced reactive particles towards the substrate and the creation of surface conditions that favour an efficient incorporation of the supplied particles in the growing film. In general it will not be possible to increase the effectivity of all three functions at the same time in one discharge.

Therefore, in the reactor that is described in this thesis, the three mentioned functions (dissociation and ionization, transport and deposition) are spatially separated, and each of them is optimized separately. A cascaded arc plasma in argon is used to dissociate and ionize the injected methane and acetylene molecules. The produced reactive particles are transported efficiently towards the substrate by means of a supersonic expansion into vacuum and a subsonic plasma beam. On the substrate an amorphous carbon film is growing.

The flowing plasma in the cascaded arc is analyzed with diagnostics and models. The electron density and the electron temperature are measured as a function of position in the arc by means of Stark broadening of the hydrogen H_{β} -line (486.1 nm) and the ratio of continuum- and line emission respectively. Together with the measured axial pressure profiles these measurements have been used to calculate the profiles of the gas temperature from a best fit of the quasi one-dimensional model to the experimental profiles. Then the overpopulation of the neutral argon ground level has been calculated. In the beginning of the arc channel this overpopulation amounts to a factor 40, independent of the gas flow. Energy considerations have shown that a large amount of the dissipated electrical energy (about 60%) is used to heat the originally cold argon gas. The ionization of argon atoms takes the other 40%. Therefore the total number of electrons (and hence the

electron density) hardly depends on the gas flow. The arc length should be at least 2 cm to be able to heat the gas until its temperature equals the electron temperature (about 12000 K).

The pressure drop over the arc channel is associated with viscous friction between the arc wall and the plasma. The flow has been analyzed numerically using the conservation laws for mass, momentum and energy. The obtained relation between the friction factor and the Reynolds number has a strong resemblance to the theoretical curve for laminar flow through a perfectly smooth duct.

The dissociation of the injected methane is analyzed using the conservation laws for mass and energy. The calculations indicate that an arc length of 2 cm after injection of the methane is sufficient to establish complete dissociation and ionization. The carbon atoms are ionized mainly by charge transfer from argon ions.

In the supersonic expansion the gas velocity, the gas temperature and the electron density are measured by means of Doppler shift, Doppler broadening and Stark broadening of the hydrogen β -line respectively. The gas velocity increases from 1700 m/s in the anode nozzle to about 4000 m/s after 50 mm. Meanwhile the temperature drops from 12000 K to less than 2000 K. Therefore the plasma composition is frozen: the ratios of the densities of the several species present in the plasma hardly change. Three particle recombination of argon ions causes the electron temperature to remain higher than the gas temperature. Again the conservation laws for mass, momentum and energy are used to describe the supersonically expanding plasma. The agreement between model and measurements is good.

A shock wave occurs at an axial position of about 50 mm. The kinetic energy of the highly directed motion is now converted partially into thermal energy. The velocity decreases to 2000 m/s, and the temperature increases (to 6000K). After the shock wave has been crossed, a subsonic, but fastly flowing (1000 m/s) plasma beam is created. The argon ions are eliminated by charge transfer to carbon atoms. Then the created carbon ions recombine fast. In this way the carbon ion density remains constant until all argon ions have been eliminated. Then also the carbon ion density decreases. Lowering the background pressure causes this process to slow down.

The growth of the amorphous carbon coatings is studied by means of *in situ* He-Ne ellipsometry. This technique, that uses the changes in polarizing properties of a growing film, provides the growth rate, but also the real and imaginary parts of the refractive index of the deposited material. The implementation that has been used for the experiments described in this thesis has an accuracy that allows the

detection of a film thickness of 10 pm. Spectroscopic ellipsometry has been used to analyze the optical properties of the films over a large spectral range. Finally the hardness of the films is estimated by means of scratch tests.

The quality of the deposited film is dominantly determined by the amount of energy per carbon atom that the plasma delivers to the surface. If this energy is small, then the refractive index is high (2.4), the optical bandgap is narrow (0.5 eV) and the hardness is large (30 GPa). Then the film is called "diamond-like". If this energy is large, then the film becomes "polymer-like". The refractive index is decreased to 1.5, the bandgap widens to 1.5 eV and the hardness decreases to less than 5 GPa. This trend might indicate that the growth of the film is in this case dominated by carbon atoms and carbon ions instead of, as is the case in conventional processes, by radicals.

The deposition rates obtained exceed the highest values (for amorphous carbon coatings) reported in the literature so far by a factor of 30. One can conclude that the new process for plasma deposition, as it is described in this thesis, offers a drastic increase of the deposition rate while the quality of the deposited films is at least as good as the ones obtained by more conventional processes.

1 INTRODUCTION

The subject of this thesis is the description of the physics of the processes that occur when amorphous carbon coatings are deposited by decomposition of hydrocarbons in a new type of plasma reactor. In this reactor the dissociation and ionization of the original material take place in the thermal, high density plasma of a cascaded arc. The hot arc plasma is cooled by allowing it to expand supersonically into a large vacuum system. In this expansion very high particle velocities are attained. This ensures that the plasma composition does not change substantially before the substrate is reached. At the substrate an amorphous carbon film is deposited. The quality of this film, determined by parameters like refractive index, hardness, absorption coefficient in the infrared spectral region, resistivity against oxidation, adhesion to the substrate, and internal stress, is strongly dependent on the plasma parameters, and can be influenced by controlling the intensity and nature of the particle flux impinging on the substrate.

Amorphous carbon coatings have a number of industrial and scientific applications. Because of the low absorption coefficient in the infrared region they are frequently used in anti-reflex and/or protective coatings for that spectral range [ENK-85, HOL-79, BUB-83]. Their (generally) high refractive index makes them applicable where an index gradient is required like optical fibers used for data transport. Also as protective coatings for solar cells or integrated circuits they can be interesting [BUB-83], although in many applications of this kind the internal stress of some kinds of the material inhibits use on thin silicon slices. In tribological applications carbon coatings strongly enhance the surface hardness of treated parts in machines and turbines [ENK-85].

Since about 1970 many different discharge types have been explored for their applicability in the field of plasma surface modification in general and of plasma deposition in particular. By far the most widespread deposition process comprises the use of a low pressure R.F. or DC glow discharge in a mixture of a noble gas like argon, hydrocarbons and sometimes oxygen [BOR-86], contacting the surface to be treated. Often the sample support is negatively biased to increase the intensity of the ion bombardment. The hydrocarbons are dissociated in the plasma glow and are transported towards the substrate by means of diffusion. Among others Matsushita

et al [MAT-84], Donahue et al [DON-85] and Vanier and coworkers [VAN-84] use glow discharges and attain deposition rates ranging from 0.3 to 3 nm/s which are in this case mainly limited by the effectivity of the transportation of the particles towards the area where the coating is formed, but also by the effectivity of the production of these reactive particles. This process is usually called "plasma deposition".

Wong et al [WON-85] makes use of a nozzle beam, whereas Ebihara [EBI-85] and Sokolowski [SOK-81] have investigated a pulsed discharge. In industrial processes ion plating has gained much interest recently, see e.g. Umeda [UME-84], especially for coatings that require a large energy flux impinging on the surface. Of course evaporation (thermal or electron beam induced) has to be mentioned. This technique is applied in a number of commercially available reactors. Shindo [SHI-84] reports good results with a modified evaporation process using a reactive gas. Afterglows of inert gases can also be used to dissociate and (sometimes) ionize (fragments of) the reactive gas, see e.g. Toyoshima and Watanabe [TOY-85, WAT-86]. Usually the metastable atoms play a dominant role in the reaction kinetics. Hollow cathode glow discharges are used to sputter material from a solid reactant [MAT-85]. A more energetic version of this discharge type, a hollow cathode arc, is used for the same purpose by Lunk et al [LUN-86]. Zarowin [ZAR-86] has developed a method based on chemical vapor transport of particles evaporated from solid material. Even multipole discharges are used for the production of coating of various materials [RUT-86, PER-83]. The industry often uses microwaves to dissociate the gas [KIE-84].

Another technique, called "Ion Beam Epitaxy" (IBE) uses a beam of ions (sometimes produced in a weak gas discharge) that is accelerated on its way to the substrate [YAM-87]. The deposition rates obtainable with this technique are strongly dependent on the reactor geometry, but usually also value around 0.1-1 nm/sec. In this case the limit is primarily set by the production of the reactive particles (ions).

If the transport properties of an ion beam can be combined with the dissociative and ionizing power of a dense discharge without losing much of the plasma volume by collimation, the deposition rate specifically can be increased substantially and the control of the process is improved. The process described in this thesis and outlined above exactly does this.

The cascaded arc plasma is very suitable as a source of reactive particles. At relatively high current densities (40–70 Amps in 4 mm diam.) and at normal working pressures ($p > 0.5$ bar) there are only minor deviations from local thermodynamical equilibrium (LTE) at a temperature of about 11000 K [TIM-84]. In this plasma each injected molecular particle is dissociated almost immediately and in many cases ionized quickly. At lower currents (5–25 A) the deviations from LTE become more substantial, and in low pressure arcs ($p < 0.2$ bar) the gas temperature can be significantly lower than the, then higher, electron temperature. If the reactive gas is not injected directly into the arc plasma but at the location of the supersonic expansion or even further downstream, the plasma beam is strongly quenched and molecular species can survive. By carefully selecting arc pressure, gas flow, arc current and injection location the composition of the plasma beam on one hand and its potential and kinetic energy on the other hand can be influenced independently. The kinetic energy of the ions impinging on the surface can be increased by applying an auxiliary discharge. In this way this plasma can provide the optimum surface environments and particle fluxes for the deposition of a wide range of materials on almost any substrate. The experiment has been carried out with hydrocarbons to produce amorphous hydrogenated carbon films (a:C-H) but the setup is not limited to this material. By choosing another starting material (SiH_4 , TiCl_4 and N_2 , etc) semiconductor and/or metallic alloy films can be produced.

In chapter 2 a model is presented which describes the plasma flow both in the arc and in the expansion area. The experimental setup and the implementation of the various diagnostic techniques are discussed in chapter 3. In chapter 4 the physical principles of the used diagnostics will be reviewed. Chapter 5 depicts the results of diagnostics and models. Finally, in chapter 6, some conclusions will be drawn.

2 MODEL

2.1 Introduction

This chapter presents a model that describes the evolution of a flowing cascade arc plasma which is seeded with hydrocarbon molecules and then expands into vacuum. In the arc channel a description according to partial local thermodynamical equilibrium (PLTE) is used. According to this concept the deviations from complete local thermodynamical equilibrium (LTE) [GRI-64, TIM-84, EDD-87] may comprise temperature differences between several species present in the plasma and also an over- or underpopulation of the ground level. The basic equations will be given in section 2.2.

The electrons and the heavy particles are all assumed to have Maxwellian energy distributions, each at their own temperature. The gas temperature and the electron density gradually approach their equilibrium values while the plasma flows through the arc channel. This relaxation will be described in section 2.3 using the transport equations. Consequently the evolution of the plasma following the injection of cold hydrocarbon gas is described. Furthermore an attempt is made to use the models developed by De Haas [HAA-86] to explain the experimentally observed large pressure drop in the arc channel.

Section 2.4 deals with the supersonic expansion of the arc plasma into vacuum. Especially the evolution of the densities and temperatures are investigated because those parameters essentially determine the chemical composition and development of the seeded plasma. The supersonic expansion is limited by a shock front. After passing this discontinuity the plasma keeps flowing with a large systematic axial velocity. Finally, in section 2.5 the calculated densities and velocities will be interpreted in terms of deposition rates.

2.2 Basic equations

As a starting point the Boltzmann equation will be used:

$$\frac{\partial f_a}{\partial t} + \underline{v}_a \cdot \nabla_r f_a + \frac{q_a}{m_a} (\underline{E} + \underline{v}^* B) \cdot \nabla_v f_a = \left[\frac{\partial f_a}{\partial t} \right]_{coll} \quad (2.1)$$

This equation describes the evolution in space and time of the distribution function $f_a(\underline{r}, \underline{v}, t)$ of species a . The right hand side (rhs) of it represents the variations of f_a induced by elastic and inelastic collisions with other species. The transport equations for mass, momentum and energy are obtained by taking the first three velocity moments of equation (2.1) [BRA-65]. If the velocity \underline{v} is decomposed into a mean component, the drift velocity \underline{w} and a random component $\underline{v}_r = \underline{v} - \underline{w}$ according to

$$\underline{w} = \frac{\int \underline{v} f d\underline{v}}{\int f d\underline{v}} \quad \text{and} \quad \langle \underline{v}_r \rangle = \frac{\int \underline{v}_r f d\underline{v}}{\int f d\underline{v}} = 0, \quad (2.2)$$

the continuum equation (zeroth moment) reads:

$$\frac{dn}{dt} = \frac{\partial n}{\partial t} + \nabla \cdot (n\underline{w}) = \int_v C_{\text{coll}} d\underline{v} \quad (2.3)$$

where the rhs describes the particle production and elimination caused by interaction with other particles. For simplicity the subscript a has been omitted.

The first moment gives the momentum equation:

$$\frac{\partial}{\partial t}(nm\underline{v}) + \nabla \cdot (nm\underline{v}\overline{v}) - qn(\underline{E} + \underline{w}^* \underline{B}) = \int_v m\underline{v} C_{\text{coll}} d\underline{v}, \quad (2.4)$$

where \overline{v} denotes averaging of \underline{v} over the velocity distribution, whereas the energy equation is obtained from the second moment:

$$\frac{\partial}{\partial t}(\frac{1}{2}nm\underline{v}^2) + \nabla \cdot (\frac{1}{2}nm\underline{v}^2 \overline{v}) - qn \underline{E} \cdot \underline{w} = \int_v \frac{1}{2}m\underline{v}^2 C_{\text{coll}} d\underline{v}. \quad (2.5)$$

Usually the equations (2.3) to (2.5) are transformed to a set of intrinsic equations by substitution. The intrinsic momentum and energy equations read

$$nm \frac{\partial \underline{w}}{\partial t} + nm(\underline{w} \cdot \nabla) \underline{w} + \nabla p + \nabla \cdot \underline{\pi} - qn(\underline{E} + \underline{w}^* \underline{B}) = \int m \underline{v}_r C_{\text{coll}} d\underline{v} \quad (2.6)$$

and

$$\frac{\partial}{\partial t}(\frac{3}{2}nkT) + \nabla \cdot (\frac{3}{2}nkT \underline{w}) + nkT \nabla \cdot \underline{w} + \underline{\pi} : \nabla \underline{w} + \nabla \cdot \underline{q} = \int \frac{1}{2}m\underline{v}^2 C_{\text{coll}} d\underline{v} \quad (2.7)$$

respectively, where k is Boltzmann's constant. The definitions of several macroscopic quantities appearing in the equations (2.3) to (2.7) are tabulated in table 2.1.

TABLE 2.1: definition of macroscopic quantities		
$n(\underline{r})$	$= \int f(\underline{r}, \underline{v}, t) d\underline{v}$: density
T	$= m \langle v_r^2 \rangle / 3k$: temperature
\underline{q}	$= \int \frac{1}{2} n m v^2 \underline{v}_r d\underline{v} = -\kappa \nabla T$: thermal heat flux
$\underline{\pi}$	$= \int n m \underline{v}_r \underline{v}_r d\underline{v} - p \underline{I}$: viscosity tensor

In the following sections these transport equations (especially eqs. (2.3) and (2.7)) will be used for a variety of particles. The source term of each equation will be evaluated. Table 2.2 lists the symbols that are used to represent the several densities and temperatures.

Furthermore we will use the equation of state:

$$p = \sum_x n_x k T_x . \quad (2.8)$$

The modified Saha equation describes the equilibrium relation between neutral and ionized species of the same kind [HSU-82]:

$$n_e \left(\frac{n_x^+}{n_x} \right) T_h / T_e = \frac{g_e W_x^+}{W_x} \left(\frac{2\pi m_e k T_e}{h} \right)^{3/2} \exp\left(-\frac{E_{ix} - \Delta E_{ix}}{k T_e}\right) , \quad (2.9)$$

where W_x represents the partition function of the neutral system and E_{ix} is the ionization energy of species x . ΔE_{ix} is the ionization potential lowering.

Arrhenius' law describes the ratio of densities and rate coefficients in the case of chemical equilibrium. For the reaction



the ratio K of the forward and reverse reaction rates (k_f and k_r) is given by:

TABLE 2.2: list of symbols

n_{ar}	:	density of argon atoms
n_{ar^+}	:	" " argon ions
n_c	:	" " carbon atoms
n_{c^+}	:	" " carbon ions
n_h	:	" " hydrogen atoms
n_{h^+}	:	" " hydrogen ions
n_{chx}	:	" " CH_x radicals
n_e	:	electron density
n_{ys}	:	density of species y according to Saha-eq.
w_y	:	velocity of species y
T_e	:	electron temperature
T_h	:	temperature of the argon atoms and ions
T_x	:	temperature of the injected particles
\underline{u}	:	velocity of the plasma: $\sum_i n_i m_i \underline{w}_i / \sum_i n_i m_i$
p_y	:	partial pressure of particle y
p	:	total system pressure
\underline{e}_x	:	axial unity vector

$$K = \frac{k_f}{k_r} = \frac{n_b n_c}{n_a} = A / (kT) \exp(-E/kT) \quad (2.10)$$

where A is the frequency factor ratio [BEN-70] and E the reaction enthalpy. The factor kT converts the listed values [KON-72] from the pressure standard state to the density standard state. The frequency factor A (in the pressure standard state) can be expressed as

$$A = \exp(\Delta S_i^\ddagger / R) \quad (2.11)$$

where R is the specific gas constant, and ΔS_i^\ddagger represents the change of the molar standard state entropy caused by the reaction.

2.3 The arc plasma

2.3.1 Heating and ionization

To analyze the evolution of the initially relatively cold, flowing arc plasma in the arc channel, a set of differential equations will be constructed that describes the development of the electron density and the gas temperature. The plasma consists of argon atoms, argon ions and electrons. The physical phenomena that will be taken into account are: direct or indirect ionization by electron impact, three particle recombination, radiative recombination and energy exchange between different species by means of elastic collisions. It has been shown [TIM-84] that for sufficiently large electron densities almost every excitation of an atom in an arc plasma eventually leads to ionization. Therefore excitation will be treated as ionization.

The neutral argon atoms and the argon ions will be treated together as far as their transport equations are concerned. The heavy particle density n_h is defined by

$$n_h = n_{ar} + n_{ar^+} . \quad (2.12)$$

Since ionization and recombination do not change the total heavy particle density n_h , the combined mass balance reads

$$\frac{dn_h}{dt} = \frac{\partial n_h}{\partial t} + \nabla \cdot (n_h \underline{w}_h) = 0 . \quad (2.13)$$

In the case of a stationary plasma

$$\nabla \cdot (n_h \underline{u}) = 0 . \quad (2.14)$$

This can be transformed to

$$\nabla \cdot \underline{u} = \underline{u} \cdot \left(\frac{\nabla T_h}{T_h} - \frac{p}{p_h} \frac{\nabla p}{p} + \frac{p_e}{p_h} \frac{\nabla p_e}{p_e} \right) . \quad (2.15)$$

In this case we can neglect the last term, because the gradient lengths for electron pressure and total system pressure are comparable and $p_e \ll p$, $p \approx p_h$.

The number balance for the electrons reads

$$\frac{dn_e}{dt} = \frac{\partial n_e}{\partial t} + \nabla \cdot (n_e \underline{w}_e) = K_{1+} n_e (n_{ar} - n_{ars}) - n_e n_{ar}^+ (K_{+1} \Lambda) \quad (2.16)$$

where K_{1+} represents the combined rate coefficient for excitation and ionization, and $(K_{+1} \Lambda)$ is the rate coefficient for radiative recombination corrected for local absorption. Three particle recombination is taken into account in eq. (2.16) by applying the method of detailed balancing [MIT-73]:

$$n_e^2 n_{ar}^+ K_{+1}^3 = n_e n_{ars} K_{1+} \quad (2.17)$$

Since we consider a stationary situation, $\nabla \cdot \underline{j} = 0$. If $\underline{w}_e \neq \underline{w}_{ar} \simeq \underline{w}_{ar}^+ \simeq \underline{u}$ then still

$$\nabla \cdot (n_e \underline{w}_e) = \nabla \cdot (n_e \underline{u}) - \nabla \cdot \underline{j} / e = \nabla \cdot (n_e \underline{u}) \quad (2.18)$$

The left hand side (lhs) of eq. (2.16) can be written as

$$\frac{\partial n_e}{\partial t} + \nabla \cdot (n_e \underline{u}) = \frac{\partial n_e}{\partial t} + \underline{u} \cdot \nabla n_e + n_e (\nabla \cdot \underline{u}) \quad (2.19)$$

The one dimensional, stationary continuity equation for n_e now results from the combination of the equations (2.15), (2.16) and (2.19):

$$\begin{aligned} \frac{\partial n_e}{\partial x} = \frac{1}{u} & (K_{1+} n_e (n_{ar} - n_{ars}) - n_e n_{ar}^+ (K_{+1} \Lambda)) + \\ & + n_e \left(\frac{1}{p} \frac{\partial p}{\partial x} - \frac{1}{T_h} \frac{\partial T_h}{\partial x} \right). \end{aligned} \quad (2.20)$$

The energy equation of the heavy particles reads

$$\begin{aligned} \frac{\partial}{\partial t} \left(\frac{3}{2} n_h k T_h \right) + \nabla \cdot \left(\frac{3}{2} n_h k T_h \underline{w}_h \right) + n_h k T_h \nabla \cdot \underline{w}_h + \underline{\pi}_h \cdot \nabla \underline{w}_h + \nabla \cdot \underline{q}_h = \\ = 3 \frac{m_e}{m_{ar}} n_e \left(\frac{1}{\tau_{ei}} + \frac{1}{\tau_{eo}} \right) k (T_e - T_h) \end{aligned} \quad (2.21)$$

where the collision times are given by

$$\tau_{ei} = \frac{3 \sqrt{m_e} (k T_e)^{3/2} (4 \pi \epsilon_0)^2}{4 \sqrt{2} \pi e^4 \ln \Lambda n_e} \quad (2.22)$$

$$\tau_{eo} = \frac{1}{n_o \cdot \langle \sigma v \rangle_{eo}} \quad (2.23)$$

Here e is the elementary charge, $\langle \sigma v \rangle_{eo}$ is the cross section for electron-neutral collisions weighed with the Maxwellian electron velocity distribution and $\ln \Lambda$ represents the Coulomb logarithm [BRA-64] which can be approximated by

$$\ln \Lambda \cong \ln(9 n_e \frac{4}{3} \pi \lambda_d^3) \quad , \quad (2.24)$$

using the Debye-length λ_d :

$$\lambda_d = \left[\frac{\epsilon_o k T_e}{n_e e^2} \right]^{\frac{1}{2}} \quad (2.25)$$

We have implicitly used the fact that the energy exchange between ions and neutrals is more effective than the direct energy transfer from electrons to ions or from electrons to neutrals. This can be shown by calculating the ratio of the elastic energy exchange (Q_{ab}/n_a) and the temperature difference ($T_a - T_b$) for the cases of electron-ion (e-i), electron-neutral (e-o) and ion-neutral (i-o) interaction. If we take

$$Q_{ab} = 3 \frac{m_a}{m_b} n_a \frac{1}{\tau_{ab}} k (T_a - T_b) \quad , \quad (2.26)$$

the result for a typical case ($n_e = 10^{22} \text{ m}^{-3}$, $n_{ar} = 3 \cdot 10^{23} \text{ m}^{-3}$, $T_e = 12000 \text{ K}$, $T_h = 8000 \text{ K}$) is:

interaction	e-i	e-n	i-n
$Q/n\Delta T \text{ [JK}^{-1}\text{s}^{-1}\text{]}$	$4.8 \cdot 10^{-17}$	$2.3 \cdot 10^{-17}$	$3.18 \cdot 10^{-16}$

Using (2.15), equation (2.21) can be rewritten as

$$\begin{aligned} \frac{\partial}{\partial t} \left(\frac{3}{2} n_h k T_h \right) + \frac{3}{2} k T_h \nabla \cdot (n_h \underline{w}_h) + \frac{3}{2} k n_h \underline{w}_h \cdot \nabla T_h + n_h k T_h \underline{u} \cdot \left(\frac{1}{T_h} \nabla T_h - \frac{1}{p} \nabla p \right) + \\ \underline{\pi}_h \cdot \nabla \underline{w}_h + \nabla \cdot \underline{q}_h = 3 \frac{m_e}{m_{ar}} n_e \left(\frac{1}{\tau_{ei}} + \frac{1}{\tau_{eo}} \right) k (T_e - T_h) \quad . \end{aligned} \quad (2.27)$$

Neglecting the effects of viscosity and heat conduction for the heavy particles and using eq. (2.14) the one-dimensional, stationary equation for T_h reads

$$\frac{\partial T_h}{\partial x} = \frac{2}{5n_h k u} \left(3 \frac{m_e}{m_{ar}} n_e \left(\frac{1}{\tau_{ei}} + \frac{1}{\tau_{eo}} \right) k (T_e - T_h) + \frac{n_h k T_h u}{p} \frac{\partial p}{\partial x} \right). \quad (2.28)$$

The equations 2.20 and 2.28 describe the evolution of the electron density and the heavy particle temperature as a function of the axial position in the arc. They can be solved numerically by Runge-Kutta integration.

2.3.2 Injection of methane

When methane is injected into the arc channel it will get partially dissociated and ionized by collisions with argon atoms and ions or electrons. The temperature of the thus formed radicals will gradually approach the electron temperature. Assuming that all radicals, molecules and ions originating from methane or its fragments have the same temperature T_x , the energy equation for the injected particles reads

$$\frac{\partial T_x}{\partial x} = \frac{2}{3n_x k u} \left(3 \frac{m_{ar}}{m_{chx}} n_{ar} n_{k_1} k (T_h - T_x) + n_x k T_x u \left(\frac{1}{p} \frac{\partial p}{\partial x} - \frac{1}{T_h} \frac{\partial T_h}{\partial x} \right) \right), \quad (2.29)$$

where k_1 represents the rate coefficient for elastic collisions between argon atoms and injected radicals; n_x is the total density of injected molecules containing carbon atoms:

$$n_x = n_{ch4} + n_{ch3} + n_{ch2} + n_{ch} + n_c + n_{c^+}. \quad (2.30)$$

For the argon atoms and ions eq. (2.28) has to be adapted to

$$\begin{aligned} \frac{\partial T_h}{\partial x} = & \frac{2}{5n_h k u} \left(3 \frac{m_e}{m_{ar}} n_e \left(\frac{1}{\tau_{ei}} + \frac{1}{\tau_{eo}} \right) k (T_e - T_h) + \right. \\ & \left. - 3 \frac{m_{ar}}{m_{chx}} n_{ar} n_x k_1 k (T_h - T_x) + \frac{n_h k T_h u}{p} \frac{\partial p}{\partial x} \right) - Q_{diss}, \end{aligned} \quad (2.31)$$

where Q_{diss} represents the energy lost by the argon atoms while dissociating methane fragments. Direct heating of the injected radicals by elastic collisions with electrons can be neglected because the mass of argon atoms is much larger than the

mass of an electron. Furthermore the electron density is lower than the argon density.

A number of chemical reactions play a dominant role in the process of dissociation and ionization of methane post its injection in the arc channel. The reactions listed in table 2.3 will be included in the calculations.

The rate coefficients for dissociation of CH_4 radicals by collisions with argon atoms are adapted from Kondratiev [KON-72] and from Benson [BEN-70]. The rate coefficient for dissociation of methane by electron impact is calculated from a cross section measured by Winters [WIN-75].

The rates for the reverse reactions are estimated from the rates of the forward reactions and the chemical equilibrium constants [KON-72]. The rates for dissociation of CH_3 , CH_2 and CH are estimated from k_2 [CAT-81], taking into account the reaction enthalpy [PRI-62].

Dimerization reactions are neglected. The rates for direct ionization of CH molecules and radicals are about a factor 10 smaller than the rate for dissociation.

TABLE 2.3 : Chemical reactions included in the calculations

Reaction	Rate	Rate reverse reaction
$\text{CH}_4 + \text{Ar} \rightarrow \text{CH}_3 + \text{H} + \text{Ar}$	k_2	k_3
$\text{CH}_4 + e \rightarrow \text{CH}_3 + \text{H} + e$	k_4	k_5
$\text{CH}_3 + \text{Ar} \rightarrow \text{CH}_2 + \text{H} + \text{Ar}$	k_6	k_7
$\text{CH}_3 + e \rightarrow \text{CH}_2 + \text{H} + e$	k_8	k_9
$\text{CH}_2 + \text{Ar} \rightarrow \text{CH} + \text{H} + \text{Ar}$	k_{10}	k_{11}
$\text{CH}_2 + e \rightarrow \text{CH} + \text{H} + e$	k_{12}	k_{13}
$\text{CH} + \text{Ar} \rightarrow \text{C} + \text{H} + \text{Ar}$	k_{14}	k_{15}
$\text{CH} + e \rightarrow \text{C} + \text{H} + e$	k_{16}	k_{17}
$\text{C} + e \rightarrow \text{C}^+ + e + e$	k_{18}	k_{19}
$\text{H} + e \rightarrow \text{H}^+ + e + e$	k_{20}	k_{21}
$\text{Ar}^+ + \text{C} \rightarrow \text{C}^+ + \text{Ar}$	k_{22}	
$\text{Ar}^+ + \text{H} \rightarrow \text{H}^+ + \text{Ar}$	k_{23}	

Furthermore the produced radical ions will probably be eliminated efficiently by dissociative recombination [KRA-79, MAI-83]. Ionization leading to molecular ions could therefore be interpreted as indirect dissociation, and the effect it has on the total decomposition of methane can in this case be neglected. The rate coefficients for charge exchange between Ar and H are calculated from a cross section given by Hasted [HAS-72]. For $\text{Ar}^+\text{-C}$ charge exchange the cross section is estimated from a similar case mentioned by Hasted.

Now the mass balances for the various species present in the plasma can be constructed.

$$\begin{aligned} \frac{\partial n_{\text{ch4}}}{\partial x} = & \frac{1}{u} (-n_{\text{ar}}n_{\text{ch4}}k_2 - n_{\text{e}}n_{\text{ch4}}k_4 + n_{\text{ar}}n_{\text{ch3}}n_{\text{h}}k_3 + \\ & + n_{\text{e}}n_{\text{ch3}}n_{\text{h}}k_5) + n_{\text{ch4}}\left(\frac{1}{T_{\text{h}}}\frac{\partial T_{\text{h}}}{\partial x} + \frac{1}{p}\frac{\partial p}{\partial x}\right) \end{aligned} \quad (2.32)$$

$$\begin{aligned} \frac{\partial n_{\text{ch3}}}{\partial x} = & \frac{1}{u} (-n_{\text{ar}}n_{\text{ch3}}k_6 - n_{\text{e}}n_{\text{ch3}}k_8 + n_{\text{ar}}n_{\text{ch2}}n_{\text{h}}k_7 + n_{\text{e}}n_{\text{ch2}}n_{\text{h}}k_9 \\ & + n_{\text{ar}}n_{\text{ch4}}k_2 + n_{\text{e}}n_{\text{ch4}}k_4 - n_{\text{ar}}n_{\text{ch3}}n_{\text{h}}k_3 + \\ & - n_{\text{e}}n_{\text{ch3}}n_{\text{h}}k_5) + n_{\text{ch3}}\left(\frac{1}{T_{\text{h}}}\frac{\partial T_{\text{h}}}{\partial x} + \frac{1}{p}\frac{\partial p}{\partial x}\right) \end{aligned} \quad (2.33)$$

$$\begin{aligned} \frac{\partial n_{\text{ch2}}}{\partial x} = & \frac{1}{u} (-n_{\text{ar}}n_{\text{ch2}}k_{10} - n_{\text{e}}n_{\text{ch2}}k_{12} + n_{\text{ar}}n_{\text{ch}}n_{\text{h}}k_{11} + n_{\text{e}}n_{\text{ch}}n_{\text{h}}k_{13} \\ & + n_{\text{ar}}n_{\text{ch3}}k_6 + n_{\text{e}}n_{\text{ch3}}k_8 - n_{\text{ar}}n_{\text{ch2}}n_{\text{h}}k_7 + \\ & - n_{\text{e}}n_{\text{ch2}}n_{\text{h}}k_9) + n_{\text{ch2}}\left(\frac{1}{T_{\text{h}}}\frac{\partial T_{\text{h}}}{\partial x} + \frac{1}{p}\frac{\partial p}{\partial x}\right) \end{aligned} \quad (2.34)$$

$$\begin{aligned} \frac{\partial n_{\text{ch}}}{\partial x} = & \frac{1}{u} (-n_{\text{ar}}n_{\text{ch}}k_{14} - n_{\text{e}}n_{\text{ch}}k_{16} + n_{\text{ar}}n_{\text{c}}n_{\text{h}}k_{15} + n_{\text{e}}n_{\text{c}}n_{\text{h}}k_{17} \\ & + n_{\text{ar}}n_{\text{ch2}}k_{10} + n_{\text{e}}n_{\text{ch2}}k_{12} - n_{\text{ar}}n_{\text{ch}}n_{\text{h}}k_{11} + \\ & - n_{\text{e}}n_{\text{ch}}n_{\text{h}}k_{13}) + n_{\text{ch}}\left(\frac{1}{T_{\text{h}}}\frac{\partial T_{\text{h}}}{\partial x} + \frac{1}{p}\frac{\partial p}{\partial x}\right) \end{aligned} \quad (2.35)$$

$$\begin{aligned} \frac{\partial n_{\text{h}}}{\partial x} = & \frac{1}{u} (n_{\text{ar}}n_{\text{ch4}}k_2 + n_{\text{e}}n_{\text{ch4}}k_4 - n_{\text{ar}}n_{\text{ch3}}n_{\text{h}}k_3 - n_{\text{e}}n_{\text{ch3}}n_{\text{h}}k_5 + \\ & + n_{\text{ar}}n_{\text{ch3}}k_6 + n_{\text{e}}n_{\text{ch3}}k_8 - n_{\text{ar}}n_{\text{ch2}}n_{\text{h}}k_7 - n_{\text{e}}n_{\text{ch2}}n_{\text{h}}k_9 + \\ & + n_{\text{ar}}n_{\text{ch2}}k_{10} + n_{\text{e}}n_{\text{ch2}}k_{12} - n_{\text{ar}}n_{\text{ch}}n_{\text{h}}k_{11} - n_{\text{e}}n_{\text{ch}}n_{\text{h}}k_{13} + \\ & + n_{\text{ar}}n_{\text{ch}}k_{14} + n_{\text{e}}n_{\text{ch}}k_{16} - n_{\text{ar}}n_{\text{c}}n_{\text{h}}k_{15} - n_{\text{e}}n_{\text{c}}n_{\text{h}}k_{17} + \\ & - n_{\text{e}}n_{\text{h}}k_{20} + n_{\text{e}}n_{\text{e}}n_{\text{h}}^+k_{21} - n_{\text{ar}}^+n_{\text{h}}k_{23}) + \\ & + n_{\text{h}}\left(\frac{1}{T_{\text{h}}}\frac{\partial T_{\text{h}}}{\partial x} + \frac{1}{p}\frac{\partial p}{\partial x}\right) \end{aligned} \quad (2.36)$$

$$\begin{aligned} \frac{\partial n_c}{\partial x} = & \frac{1}{u} (n_{ar}n_{ch}k_{14} + n_en_{ch}k_{16} - n_{ar}n_cn_hk_{15} - n_en_cn_hk_{17} + \\ & + n_en_ck_{18} - n_en_en_c^+k_{19} - n_{ar}^+n_ck_{22}) + \\ & + n_c \left(\frac{1}{T_h} \frac{\partial T_h}{\partial x} + \frac{1}{p} \frac{\partial p}{\partial x} \right) \end{aligned} \quad (2.37)$$

$$\begin{aligned} \frac{\partial n_c^+}{\partial x} = & \frac{1}{u} (n_en_ck_{18} - n_en_en_c^+k_{19} + n_{ar}^+n_ck_{22}) + \\ & + n_c^+ \left(\frac{1}{T_h} \frac{\partial T_h}{\partial x} + \frac{1}{p} \frac{\partial p}{\partial x} \right) \end{aligned} \quad (2.38)$$

$$\begin{aligned} \frac{\partial n_h}{\partial x} = & \frac{1}{u} (n_en_hk_{20} - n_en_en_h^+k_{21} + n_{ar}^+n_hk_{23}) + \\ & + n_h^+ \left(\frac{1}{T_h} \frac{\partial T_h}{\partial x} + \frac{1}{p} \frac{\partial p}{\partial x} \right) \end{aligned} \quad (2.39)$$

The equations (2.20), (2.29) and (2.31) to (2.39) determine the evolution of the densities of most of the species present in the plasma if the pressure gradient is known. They are solved numerically by (Runge–Kutta) integration.

De Haas recently developed a model to describe the flow of a fully equilibrated argon plasma in a cascaded arc [HAA–86]. If the continuum, momentum and energy equations are summed over all species present in the plasma, they read (one–dimensional)

$$\frac{\partial \rho}{\partial t} + \frac{\partial}{\partial x}(\rho u) = 0 \quad , \quad (2.40)$$

$$\rho \frac{\partial u}{\partial t} + \rho u \frac{\partial u}{\partial x} + \frac{\partial p}{\partial x} = -\frac{1}{4} \rho u^2 \frac{f}{D} \quad , \quad (2.41)$$

and

$$\frac{\partial h}{\partial t} + u \frac{\partial h}{\partial x} + u \frac{\partial u}{\partial t} + u^2 \frac{\partial u}{\partial x} - \frac{1}{\rho} \frac{\partial p}{\partial t} = q \quad (2.42)$$

respectively, where ρ is the mass density, D is the diameter of the arc channel, f is the wall friction factor, h is the specific enthalpy and q is the source term for the total energy balance. The equations (2.40) to (2.42) can be transformed into a set of linear differential equations in p , ρ and T . If the boundary conditions are taken into account this set can be solved numerically, again by Runge–Kutta integration.

2.4 Expansion of the seeded plasma

2.4.1 Introduction

At the end of the arc channel the plasma is accelerated to sonic conditions. As soon as the diameter of the channel increases the flow will become supersonic. In the diverging nozzle a quasi one-dimensional approach will be followed to describe the evolution of the plasma (section 2.4.2). It appears that the nozzle exit pressure only differs from the experimental background pressure by a factor of 2. Therefore the quasi one-dimensional calculations can be continued [OWC-64]. The Rankine-Hugoniot relations describe the overall changes of the flow parameters when a shock wave is passed. In section 2.4.3 they will be modified for this particular case. After the shockwave is passed, the quasi one-dimensional calculations are again continued assuming that the divergence of the subsonic plasma beam is determined by ambipolar diffusion (section 2.4.4).

2.4.2 The nozzle

If we again consider a stationary situation ($\nabla \cdot \underline{j} = 0$) then the number balances for electrons, radicals and argon atoms and ions read

$$\nabla \cdot (n_e \underline{u}) = n_e (n_{ar} - n_{ars}) K_1, \quad (2.43)$$

$$\nabla \cdot (n_x \underline{u}) = S_x \quad (2.44)$$

and

$$\nabla \cdot (n_h \underline{u}) = 0 \quad (2.45)$$

respectively. If the momentum balances of all species present in the plasma are added, the result is:

$$\rho(\underline{u} \cdot \nabla) \underline{u} + \nabla p = 0. \quad (2.46)$$

Assuming the heavy particles all have the same temperature T_h the total energy balance for all heavy particles reads

$$\nabla \cdot \left(\frac{3}{2} n_h k T_h \underline{u} \right) + n_h k T_h (\nabla \cdot \underline{u}) = -\nabla \cdot \underline{q}_h - \Pi_c \cdot \nabla \underline{u} + Q_{eh} - Q_{dissh} \quad (2.47)$$

Finally, the electron energy balance is needed:

$$\begin{aligned} \nabla \cdot \left(\frac{3}{2} n_e k T_e \underline{u} \right) + n_e k T_e (\nabla \cdot \underline{u}) &= -\nabla \cdot \underline{q}_e - \Pi_e \cdot \nabla \underline{u} - n_e (n_{ar} - n_{ars}) K_{1+} E_{ion} + \\ &- n_e^2 (K_{+1} \Lambda) \frac{3}{2} k T_e - 4\pi C_1 n_e^2 \langle Z \rangle T_e^{\frac{1}{2}} \frac{k}{hc} \xi_{ff} - Q_{eh} - Q_{line} + \\ &- Q_{rec} - Q_{fric} - Q_{disse} . \end{aligned} \quad (2.48)$$

Here S denotes the source term of the mass balance for species x (see eqs. (2.32) to (2.39)), Q_{dissh} and Q_{disse} the energy losses of the heavy particles and of the electrons respectively due to chemical reactions, Q_{line} and Q_{rec} the energy losses of the electrons caused by escape of line radiation and by escape of radiation resulting from recombination to excited levels. The term containing ξ_{ff} represents the inelastic free-free transitions (Bremsstrahlung) and Q_{eh} denotes the energy transfer from electrons to heavy particles due to elastic collisions (cf eq. (2.26)). Implicitly we have excluded Ohmic dissipation by convective currents which might be set up in the expansion.

If the ionization degree α is defined as $\alpha = n_e/n_h$ the mass density ρ can be expressed by

$$\rho = m_{ar}(n_{ar} + n_e) . \quad (2.49)$$

Furthermore

$$p = k(n_e T_e + n_h T_h) = \frac{k\rho}{m_{ar}}(\alpha T_e + T_h) . \quad (2.50)$$

Now the equations (2.43) to (2.48) can be rewritten as:

$$\nabla \cdot (\rho \underline{u}) = 0 , \quad (2.51)$$

$$\nabla \cdot (\alpha \rho \underline{u}) = \alpha \rho (n_{ar} - n_{ars}) K_1 , \quad (2.52)$$

$$\rho m_{ar} (\underline{u} \cdot \nabla) \underline{u} + \nabla \cdot (k\rho(\alpha T_e + T_h)) = 0 , \quad (2.53)$$

$$\nabla \cdot \left(\frac{3}{2} \alpha \rho T_e \underline{u} \right) + \alpha \rho T_e (\nabla \cdot \underline{u}) = Q_e \frac{m_{ar}}{k} \quad (2.54)$$

and

$$\nabla \cdot \left(\frac{3}{2} \rho T_h \underline{u} \right) + \rho T_h (\nabla \cdot \underline{u}) = Q_h \frac{m_{ar}}{k} \quad (2.55)$$

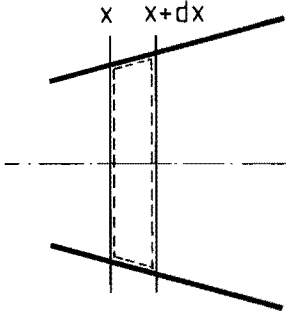


Fig. 2.1. The control volume in the nozzle used to make the transport equations quasi one-dimensional. The dashed curve indicates the boundaries of the reference surface.

respectively, where Q_h and Q_e represent the rhs of eq. (2.47) and of (2.48).

To study the expansion of the chemically active plasma in the supersonic nozzle the equations (2.51) to (2.55) will be applied to a control volume which is depicted schematically in figure 2.1. A quasi one-dimensional approach is followed, as is usual in treating nozzle expansions [OWC-64]. This implies that the energy and momentum transfer of the plasma to the nozzle wall are neglected, the radial diffusion and heat conduction terms are neglected because they are much smaller than the axial expansion terms, and that the parameters in the equations are regarded as constant over the nozzle cross section. If furthermore viscosity effects are assumed to be negligible, then the set of equations transforms to:

$$A \frac{\partial}{\partial x}(\rho u) + \rho u \frac{\partial A}{\partial x} = 0 \quad (2.56)$$

$$A \frac{\partial}{\partial x}(\alpha \rho u) + \alpha \rho u \frac{\partial A}{\partial x} = \alpha \rho (n_{ar} - n_{ars}) K_1 A \quad (2.57)$$

$$\rho m_{ar} u \frac{\partial u}{\partial x} + \frac{\partial}{\partial x}(k \rho (T_h + \alpha T_e)) = 0 \quad (2.58)$$

$$A \frac{\partial}{\partial x}(\frac{3}{2} \alpha \rho T_e u) + \frac{5}{2} \alpha \rho u T_e \frac{\partial A}{\partial x} + \alpha \rho T_e A \frac{\partial u}{\partial x} = Q_e \frac{m_{ar}}{k} A \quad (2.59)$$

$$A \frac{\partial}{\partial x}(\frac{3}{2} \rho T_h u) + \frac{5}{2} \rho u T_h \frac{\partial A}{\partial x} + \rho T_h A \frac{\partial u}{\partial x} = Q_h \frac{m_{ar}}{k} A. \quad (2.60)$$

where A is the nozzle cross section area. This set of equations can be rewritten as

$$\frac{\partial \alpha}{\partial x} = \frac{\alpha}{u} \frac{S_e}{n_e} \quad (2.61)$$

$$\frac{\partial u}{\partial x} = 5u \frac{k T}{3u^2 m_{ar} - 5k T_a} \frac{1}{A} \frac{\partial A}{\partial x} - \frac{Q_e + Q_h}{3u^2 m_{ar} - 5k T_a} \frac{2 m_{ar}}{\rho} \quad (2.62)$$

$$\frac{\partial \rho}{\partial x} = -3\rho \frac{kT}{3u^2 m_{ar} - 5kT_a} \frac{1}{A} \frac{\partial A}{\partial x} - \frac{Q_e + Q_h}{3u^2 m_{ar} - 5kT_a} \frac{2m_{ar}}{u} \quad (2.63)$$

$$\begin{aligned} \frac{\partial T_e}{\partial x} = & -2 T_e \frac{u^2 m_{ar}}{3u^2 m_{ar} - 5kT_a} \frac{1}{A} \frac{\partial A}{\partial x} + \frac{Q_e + Q_h}{3u^2 m_{ar} - 5kT_a} \frac{4m_{ar} T_e}{3\rho u} + \\ & + \frac{2}{3} Q_e \frac{m_{ar}}{\rho \alpha u k} - \frac{1}{2} \frac{\alpha T_e}{u} (n_{ar} - n_{ars}) K_1 \end{aligned} \quad (2.64)$$

$$\begin{aligned} \frac{\partial T_h}{\partial x} = & -2 T_h \frac{u^2 m_{ar}}{3u^2 m_{ar} - 5kT_a} \frac{1}{A} \frac{\partial A}{\partial x} + \frac{Q_e + Q_h}{3u^2 m_{ar} - 5kT_a} \frac{4m_{ar} T_h}{3\rho u} + \\ & + \frac{2}{3} Q_h \frac{m_{ar}}{\rho u k} - \frac{1}{2} \frac{\alpha T_h}{u} (n_{ar} - n_{ars}) K_1 \end{aligned} \quad (2.65)$$

where the effective temperature T_a is defined by

$$T_a = T_h + \alpha T_e, \quad (2.66)$$

and S_e represents the source term for electron production. The rate equations (2.32) to (2.33) for the injected radicals can be transformed into the quasi one-dimensional form using

$$A u \frac{\partial n_x}{\partial x} = -A n_x \frac{\partial u}{\partial x} - n_x u \frac{\partial A}{\partial x} + S_x A. \quad (2.67)$$

where (2.62) can be used to substitute $\partial u / \partial x$. The two-temperature speed of sound c_{pl} can be deduced from the equations (2.61) to (2.65):

$$c_{pl} = \left[\frac{5kT_a}{3m_{ar}} \right]^{1/2}. \quad (2.68)$$

The equations (2.61) to (2.67) describe the evolution of the ionization degree, the plasma velocity, the densities of the several species and the electron and heavy particle temperatures in a chemically active plasma that flows supersonically through a nozzle with no wall friction or wall heat interaction. They can be solved numerically.

2.4.3 Shock wave

For a normal shock wave the conservation equations for mass, momentum and energy when crossing the shock (Rankine–Hugoniot relations) read

$$\rho u = \hat{\rho} \hat{u}, \quad (2.69)$$

$$p + \rho u^2 = \hat{p} + \hat{\rho} \hat{u}^2, \quad (2.70)$$

and

$$h + \frac{1}{2}u^2 = \hat{h} + \frac{1}{2}\hat{u}^2 \quad (2.71)$$

respectively, where \hat{p} , $\hat{\rho}$, \hat{u} and \hat{h} denote the pressure, mass density, velocity and enthalpy after the shock. Hsu has derived an expression for the enthalpy h [HSU-82]. If the temperature dependence of the partition functions is neglected the result reads:

$$h = \frac{1}{\rho} \left(\frac{5}{2} k n_h T_h + \frac{5}{2} k n_e T_e + n_e E^{1+} \right). \quad (2.72)$$

This can be transformed to

$$h = \frac{5}{2} \frac{p}{\rho} + \frac{\alpha E^{1+}}{m_{ar}}. \quad (2.73)$$

As the residence time of the plasma in the shock is small compared to the time needed for substantial recombination the ionization degree α can be kept constant over the shock.

Using the equation of state ($p = \rho R T_a$) and introducing the Mach number $M = u/c_{p1}$ the equations (2.69) to (2.73) can be transformed into

$$\hat{p} = p \left(1 + \frac{5}{4}(M^2 - 1) \right) \quad (2.74)$$

$$\hat{u} = u \left(1 + \frac{3}{4} \left(\frac{1 - M^2}{M^2} \right) \right) \quad (2.75)$$

$$\hat{\rho} = \rho \frac{1}{1 + \frac{3}{4} \left(\frac{1 - M^2}{M^2} \right)} \quad (2.76)$$

$$\hat{T} = T \left(1 + \frac{3}{16} \left(\frac{(5M^2/3+1)(M^2-1)}{M^2} \right) \right). \quad (2.77)$$

Each of the relevant densities will be transformed like the mass density ρ . The plasma equilibrium is assumed frozen in the shock wave. At all considered axial positions in the nozzle these Rankine–Hugoniot relations are used to calculate the pressure if a shock was to occur. If this pressure equals the experimentally determined background pressure the location of the shock is found.

2.4.4 Subsonic relaxation

In this section the equations (2.32–2.39) and (2.61–2.67) will be used again. Since the axial gradients are now no longer larger than the radial gradients, the divergence of the plasma beam will be determined by diffusion. As an approximation the angle φ that the plasma boundary makes with the plasma axis at each axial position can be expressed by

$$\tan \varphi = F \frac{D}{r_p u}, \quad (2.76)$$

where D represents the diffusion coefficient and r_p the plasma radius. As the plasma mainly consists of argon atoms and ions, D can be approximated by the ambipolar diffusion coefficient for an argon plasma [TIM–84]

$$D = 2 \cdot \frac{2.76 \cdot 10^{18}}{n_{ar} + n_e} T_e^{0.64}. \quad (2.77)$$

The coefficient F depends on the actual radial profile of the particle densities in the plasma beam. However, a number of common profiles (Gauss, Lorentz, Bessel, parabola) yield approximately the same result ($F = 2 \pm 20\%$). The radial heat conduction is estimated in a similar way. The approach followed in this section is similar to the one–dimensional treatment of jet and duct flows by Thompson [THO–65].

2.5 Deposition rates

Carbon atoms and especially carbon ions have a sticking probability close to 1. Hydrocarbon radicals are incorporated in the film less easily. If the incorporation probability of a carbon containing species i is represented by X_i , then the growth rate R of the deposited film can be evaluated from:

$$R = \sum_i n_i X_i u V, \quad (2.78)$$

where V represents the mean volume per incorporated carbon atom. Using the mass density ρ_f of the deposited film, V can be estimated by

$$V = \left[\frac{\rho_f}{m_c} \right]^{-1}, \quad (2.79)$$

where m_c denotes the mass of a carbon atom. Here the contribution of hydrogen atoms to the mass density is neglected.

3 EXPERIMENT

3.1 Introduction

In this chapter the experimental techniques will be described. Paragraph 3.2 gives a detailed view of the reactor as far as vacuum system and plasma generation are concerned. Section 3.3 depicts the optical system as it is used for the various spectroscopic techniques. Finally, section 3.4 outlines the practical implementation of ellipsometry.

As already stated in chapter 1, the reactor which is used in the experiments combines the transport properties of an ion beam with the dissociative and ionizing power of a cascaded arc. Figure 3.1 presents an outline of the construction. The reactive gas is injected either in the dense arc plasma itself or further downstream in the expansion area. The cascaded arc is of a special design to allow for the injection of methane avoiding both the destruction of the electrodes and the creation of a short-circuit between two adjacent cascaded plates caused by graphite deposition in the arc channel. The arc will be discussed in section 3.2.1, together with its electrical circuitry.

Through a hole in the anode the plasma is allowed to expand into a large vacuum system (see section 3.2.2). Opposing the arc an electrically floating and water cooled sample support is mounted. It is possible to create an auxiliary discharge between sample support and vacuum system and this discharge influences the intensity of the ion bombardment. This feature will be discussed in section 3.2.3.

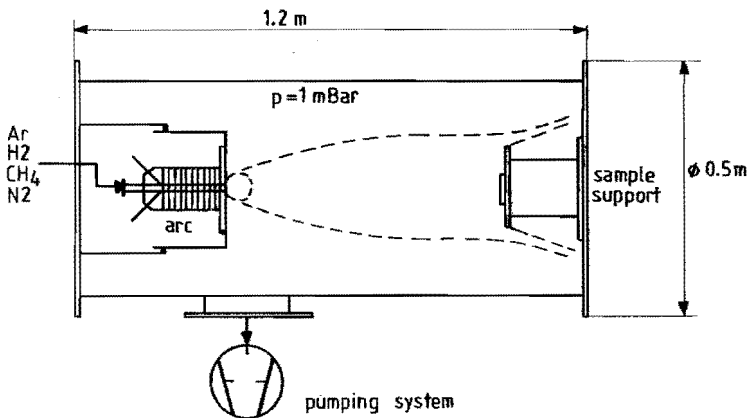


Fig. 3.1. Outline of the reactor for plasma deposition.

3.2 The reactor

3.2.1 The cascaded arc

The cascaded arc was introduced in 1956 by Maecker [MAE-56]. Until now it has been applied almost exclusively for investigations of scientific interest. This type of wall stabilized arc plasmas can be operated under a wide range of pressures (0.1 – 1000 Bar) and currents (5 – 2000 Amp.), and is characterized by large electron densities, high ionization degrees and moderate temperatures. Mostly noble gases or hydrogen are used to feed the plasma, but exceptionally molecular gases like SF₆ are added [VAC-85, GLE-87]. The deviations from local thermal equilibrium (LTE) have been studied by numerous authors [e.g. KAF-79, EDD-75, TIM-85]. At high densities the non-ideal plasma behavior has been explored [BAU-76, TIM-84]. Recently de Haas has investigated the physics of a strongly flowing cascaded arc plasma [HAA-86].

Thermal plasmas in general are increasingly used in technological processes. Atmospheric plasma jets are used in plasma spraying and plasma welding and cutting. High power transferred arcs are employed for melting metal ores in large ovens. Inductively coupled plasmas (ICP's) at moderate power levels are used in spectrochemistry. High power ICP's are applied in gas synthesis reactors. High pressure short arcs in xenon are utilized as a bright light source.

In this study a cascaded arc plasma is employed to dissociate and ionize molecular gases. Therefore a special design has been used (see fig. 3.2 for an overview). Basically the arc consists of an anode, a stack of electrically isolated copper plates, and three cathodes.

The cathodes are made of a sharpened pin of thoriated tungsten, which is pressed into a small copper screw. This screw is mounted in a water cooled copper shaft, which is cemented into a quartz cylinder that isolates the cathode from the support. The cylinder is fixed in the support by a compressed, sliding O-ring of Viton elastomere, which also serves as vacuum seal. The diameter of the tungsten tips is 1 mm for currents up to 30 Amperes per cathode, and 2 mm for higher currents. The thorium which is present in the material segregates to the surface and increases the electron emission. This allows operation at lower temperatures, and prevents the material from melting. The cathode tips are the only parts of the arc system that show any wear. They have to be replaced after about 500 operating hours. The cathode shafts can be removed without taking apart the rest of the

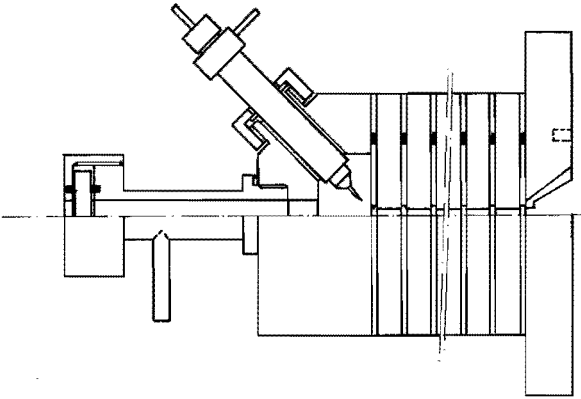


Fig. 3.2. Outline of the cascaded arc used in the reactor for plasma deposition. The various parts are introduced in the text.

construction, so the exchange of the tips only takes a few minutes.

The water cooled cathode support also incorporates a window through which the arc channel can be observed end-on. The gas is fed through the shaft on which this window is mounted.

The cascade plates are of a very simple design (see figure 3.3). They consist of a copper plate with a central bore of 4 mm, which is surrounded by a channel through which the cooling water is flowing. The plate thickness is 5 mm. The arc channel is formed by the central bores of the 10 stacked plates that are kept at an

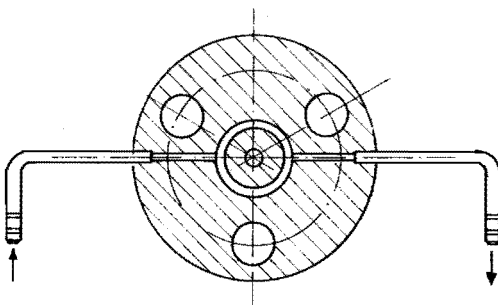


Fig. 3.3. Sectioned view of a cascade plate. The central bores of the stacked plates form the arc channel. The cooling water is supplied through the tubes.

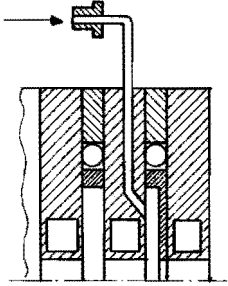


Fig. 3.4. Injection of methane in the arc channel. Three adjacent cascade plates are shown. Methane is injected within the Viton vacuum sealing ring through one of the cascade plates. A boron nitride ring makes sure that no deposition takes place in the arc.

interspacing of 1 mm by PVC spacing rings. Inside the spacers a Viton O-ring is mounted as a vacuum seal. The O-ring is prevented from melting by absorption of plasma radiation by a white ring made of Teflon or boron nitride.

When the methane is injected into the arc channel itself special precautions have to be taken to prevent graphite deposition on the walls which would lead to short-circuiting of the plates. Therefore a boron nitride ring is installed just after the injection (see figure 3.4). This allows the methane to dissociate and ionize before it contacts the cold copper plates. When the injection takes place after the last

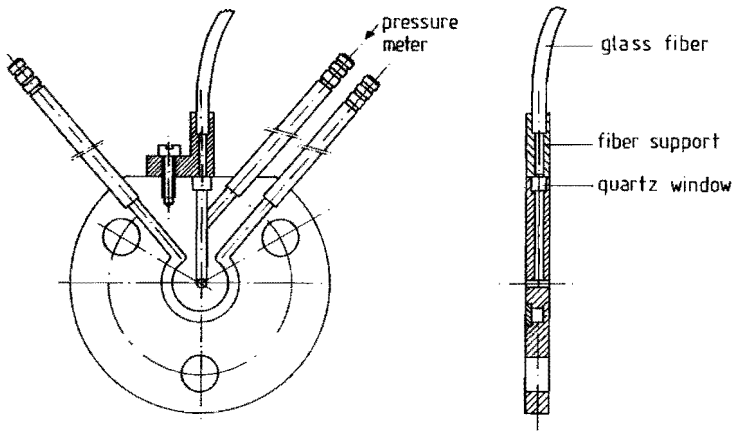


Fig. 3.5. The cascade plate designed to allow for the measurement of the local gas pressure. Side-on optical observation of the arc plasma is carried out through the radial bore (2 mm diameter).

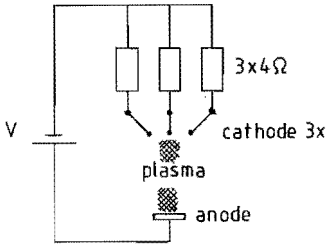


Fig. 3.6. Electrical circuitry of the arc. The series resistors make sure that the current is divided equally over the three cathodes.

plate, just before the anode nozzle is reached, this plate can be omitted. For diagnostic reasons a special set of plates has been constructed that allow side-on observation of the plasma through small quartz windows as well as measurement of the pressure in the arc channel as a function of the axial position (see figure 3.5).

The anode nozzle is made of copper, tungsten or graphite and has a conical shape. It is pressed into the water cooled support. The precision with which the conical hole is fabricated assures good electrical and thermal contact. Sonic as well as supersonic nozzles can be used. This construction of the anode allows exchange of the nozzle insert in a few seconds.

The complete arc assembly is fixed to the anode supporting flange, which is attached to the vacuum system. As the vacuum system is grounded, the anode is grounded too. The electrical circuit is depicted in figure 3.6. The resistors of 4 Ohm in the cathode supply lines make sure that all three cathodes are 'burning' independently. Figure 3.7 shows the I-V curve of one of the electrodes for several gas flows.

3.2.2 Vacuum system and gas handling

The vacuum vessel consists of a stainless steel cylinder with a length of 1.2 m, and a diameter of 0.5 m. It incorporates several windows and flanges that allow the operation of various diagnostics. The end flanges are fixed to the cylinder with hinges, and they can be opened and closed very easily. On one 'door' the cascaded arc is mounted onto a cylinder that can slide in another cylinder over a length of 0.2 m while the vacuum is maintained. This allows axial motion of the arc in the vacuum system without the need of bringing the apparatus up to atmospheric pressure. On the other 'door' the sample support is attached. It can be moved

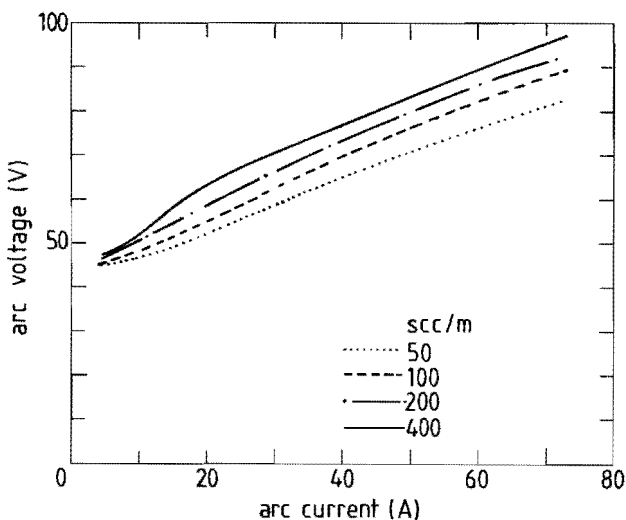


Fig. 3.7. Current-voltage (I - V) plot of the cascaded arc for four values of the gas flow.

axially over a distance of about 1 meter while maintaining vacuum (also a sliding O-ring construction), and is electrically isolated from the vacuum system to allow the creation of an auxiliary discharge (see section 3.2.3).

Essentially two pumping lines are used (see fig 3.8). The first one is used when the reactor is operated. It incorporates a mechanical rotary piston pump and two roots blowers, and is connected to the vacuum vessel by a stepper motor controlled valve. This system makes it possible to set the pumping speed from 10 l/sec up to 700 l/sec. In this way the working pressure in the system and the gas flow can be controlled independently. In figure 3.9 the pumping speed for argon is depicted as a function of gas flow for several valve positions.

The second pumping line consists of a rotary pump and an oil diffusion pump. It is used when the reactor is not operated and keeps the background pressure below 10^{-4} Pa.

The gases are fed through mass flow controllers. Argon and hydrogen are supplied at the arc entrance, whereas methane is added in the arc channel. Special filters have been installed to protect the flow controllers from damaging by small particles in the gas line. Figure 3.10 illustrates the gas handling system.

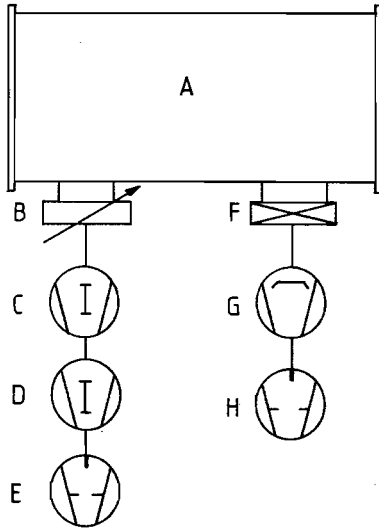


Fig. 3.8. Outline of the vacuum system. The main pumping line, consisting of roughing pump E and two Roots-blowers (C and D) is connected to vacuum chamber A by a controlable valve (B). The second line comprises roughing pump H, oil diffusion pump G and butterfly valve F.

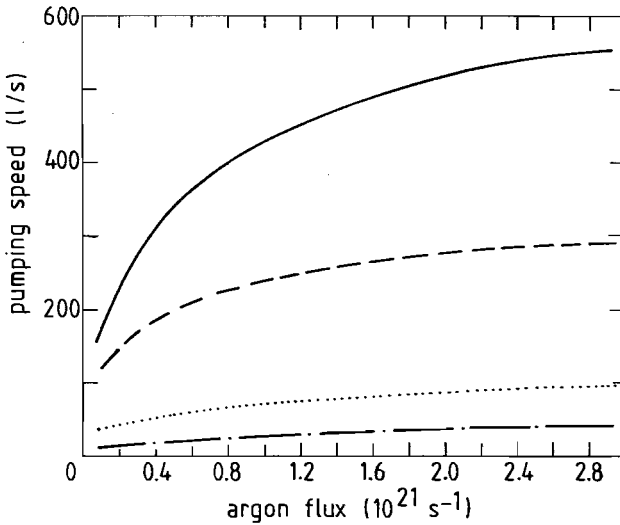


Fig. 3.9. Pumping speed of the main pumping line as a function of argon flux for four valve positions. Friction with the walls of the (2.5 m long) tube that connects the pump with the vacuum vessel causes the pumping efficiency to decrease for small values of the argon flux.

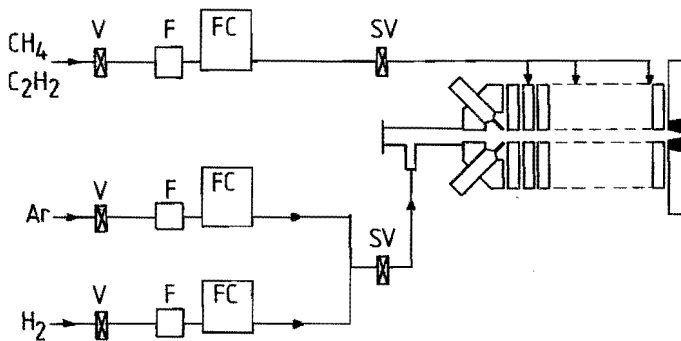


Fig. 3.10. The gas supply system. The gases are fed to the flow controllers FC through the filters F. The valves V and SV shut off the gas line close to the gas bottle and close to the cascaded arc respectively.

3.2.3 The auxiliary discharge

As already mentioned in the previous section the sample support is electrically isolated from the vacuum system. It is connected to a power supply with a series resistance of 1000 Ohms to be able to create an auxiliary discharge which negatively biases the sample support. As the major part of the discharge voltage drop takes place over the cathode fall region, the energy of the ions impinging on the substrate surface can be tuned from 0 to 200 eV. The power that is dissipated in the discharge (about 20 Watts) is small compared to the energy present in the plasma beam, so it is reasonable to assume that the gas temperature and dissociation degree of the plasma beam are hardly influenced by the auxiliary discharge.

Figure 3.11 shows the I-V plot of the auxiliary discharge. It is clear that it is not a self-sustained glow discharge.

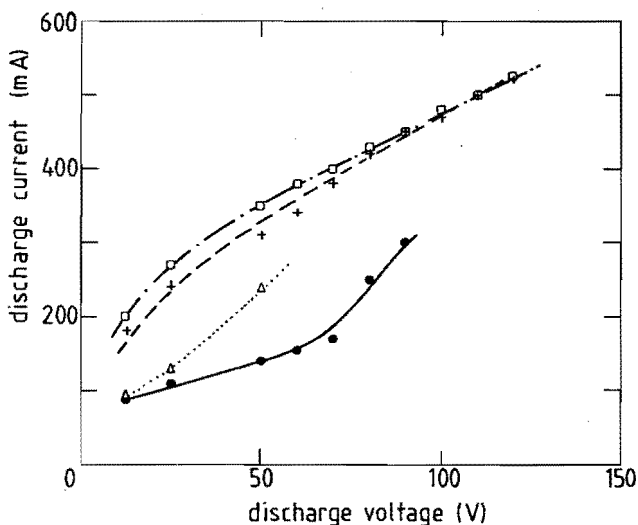


Fig. 3.11. I - V curve of the auxiliary discharge for four gas pressures (20, 50, 100 and 200 Pa).

3.3 The optical system

An optical system has been implemented which makes the application of various spectroscopic techniques possible (see figure 3.12). Lens L_4 and mirror M_4 are mounted together on a support, which is vertically translatable and can be rotated around a vertical axis. Since the part of the lightbeam between the lenses L_4 and L_2 is parallel, this allows lateral scanning of the plasma without significantly changing the image quality. It is also very simple to change the angle which the observation direction makes with the plasma axis. When mirror M_5 is inserted, a small hollow cathode arc will be imaged on the monochromator instead of the expanding plasma. This hollow cathode arc has a spectrum which almost exclusively consists of lines. The continuum radiation is of negligible strength. Furthermore, the lines do not show any Stark- or Doppler-shift, so they can be used as wavelength reference. The Fabry-Pérot interferometer can be inserted in the parallel part of the path of light. Lens L_2 images the detection volume in the plasma on the diaphragm D_1 . Finally, lens L_1 images the diaphragm D_1 on the entrance slit of the monochromator. On the exit slit an RCA 5624 photomultiplier is installed, which is

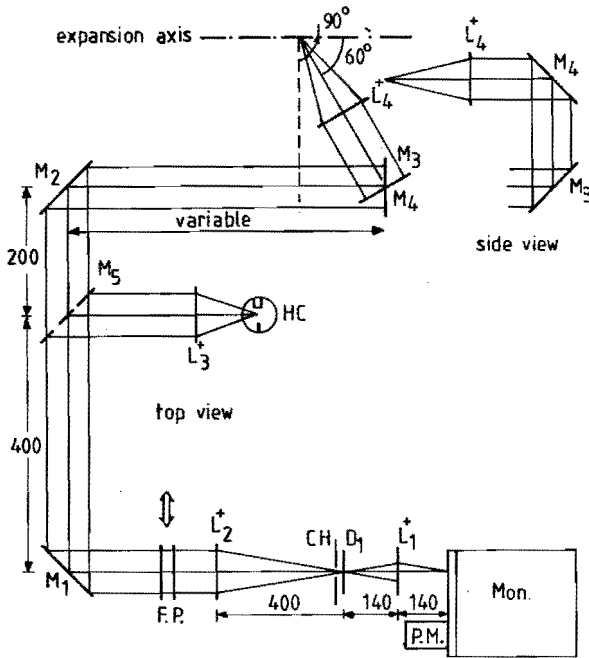


Fig. 3.12. The optical system. The various components are introduced in the text. All indicated distances are in mm.

connected with the data acquisition system. To eliminate most of the signal noise, the lightbeam is chopped by the chopper CH, and the signal is fed to a lock-in amplifier. A Jarrel-Ash 0.5 m. monochromator selects the wavelength, whereas the (pressure scanned) Fabry-Pérot interferometer is added in the case of high resolution spectroscopy. For the monochromator usually slit widths of $100 \mu\text{m}$ were used. With a dispersion of 1.6 nm per mm this results in a spectral width of 0.16 nm.

For observation of the cascaded arc itself the system becomes much simpler: an optical fiber that is connected to a cascaded plate (see fig. 3.5) is put with its other end directly in front of the entrance slit of the monochromator. In this case the quality of the image is not very good, but since only an axial dependence is sought after this is not a problem.

To get an impression of the size of the detection volume the relative transmitted intensity was calculated for a number of points in the plasma with a

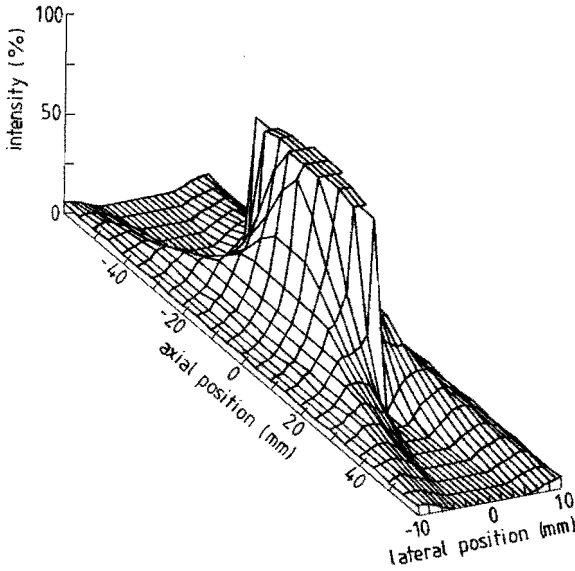


Fig. 3.13. The relative intensity transmitted by the optical system as a function of the position in the detection volume. Basically the volume is a cylinder with a length of 40 mm and a diameter of 4 mm.

matrix method. Figure 3.13 illustrates the shape of this detection volume. One can clearly see that the diameter of the imaged part of the plasma is small, but the length is considerable. With an angle of 67 degrees between the observation direction and the plasma axis (as is used mostly for the Doppler-shift measurements) the axial integration distance values around 1 cm.

The apparatus profiles of the monochromator and of the Fabry-Pérot interferometer were measured with a low pressure argon lamp. The profiles appear to be Voigt profiles. The transmission of a Fabry-Pérot interferometer is given by the Airy-function, which is periodic with a period called the free spectral range (*FSR*). The *FSR* depends on the wavelength λ , the distance d of the two parallel interferometer plates and the refractive index n of the medium between the two plates according to

$$FSR = \lambda^2 / 2nd \quad (3.1)$$

When the reflection coefficient of the mirrors is high enough the maxima of

the Airy profile can be approximated by Voigt profiles. The Lorentz and Gauss fractions of these are caused by different physical phenomena. The surface roughness of the mirrors gives a Gauss profile. The finite size of the pinhole that selects the central part of the diffraction pattern, absorption by mirror surfaces, non parallelism of the mirrors and diffraction from the beam aperture all cause a Lorentz profile. Each effect has its own width. The ratio of the width and the FSR is called the finesse of the instrument. The most important finesses are given by the following relations;

* reflection finesse $F_r = \pi\sqrt{R}/(1-R)$ (3.2)

R : reflection coefficient

* surface roughness finesse $F_s = S/2$ (3.3)

S : surface roughness in λ/k

* pinhole finesse $F_p = 4\lambda f^2/(r^2 d)$ (3.4)

d : diameter pinhole

f : focal length of imaging lens

* non-parallelism finesse $F_n = \lambda/(2d\beta)$ (3.5)

d : mirror distance

β : angle between the two mirrors

From the Gauss component of the measured apparatus profile the surface roughness can be calculated to be $\lambda/100$, which agrees well with the factory specifications. The reflection finesse is in our case 62 and the pinhole finesse is 215.

The signal from the lock-in amplifier is processed by a M68000 microcomputer, which is connected to a LSI11/23 hostcomputer with a background memory of 0.5 Gbyte (see figure 3.14). The operating language is PEP, a Pascal-like, interpreting language [VER-81], that controls the interface system.

The signal of the pressure in the Fabry-Pérot interferometer and the intensity signal of the lock-in amplifier are sampled by a multiplexed 12-bit ADC. The M68000 stores the data on the background memory, and also performs the Voigt-analysis (see section 4.2.1). The line profiles can be plotted on a pen plotter.

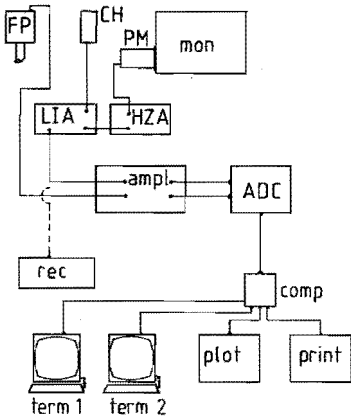


Fig. 3.14. Data acquisition system used for Doppler spectroscopy. Components: monochromator (mon), photo multiplier (PM), chopper (ch), Baratron pressure transducer connected to the Fabry-Pérot interferometer (FP), high-Z amplifier (HZA), lock-in amplifier (LIA), amplifier (ampl), analog to digital converter (ADC), recorder (rec), M68000 laboratory micro computer (comp), text terminal (term1), graphics terminal (term2), plotter (plot) and printer (print).

3.4 Implementation of ellipsometry

Ellipsometry is a technique that uses the difference in reflection ratio that occurs when monochromatic electromagnetic waves, polarized parallel respectively perpendicularly to the plane of incidence, are reflected at a flat surface. Because of the internal reference of the technique (see section 4.3) it is very accurate and relatively insensitive to optical imperfections. Essentially two different systems have been used.

The first one is a monochromatic ellipsometer based on a He-Ne laser that can be used in-situ. It is employed to monitor the plasma deposition process as far as growth rate of the film and its refractive index (at $\lambda=632.8$ nm) are concerned. The second one is a spectroscopic ellipsometer which is used to determine the optical parameters of the produced films. This one has not been used in-situ.

Section 3.4.1 will present the experimental setup of the two systems, where section 3.4.2 will discuss the data reduction techniques.

3.4.2 Experimental setup

The configuration of the rotating analyzer He-Ne ellipsometer is of the standard Polarizer Sample Analyzer (PSA) type [AZZ-79] (see figure 3.15). To

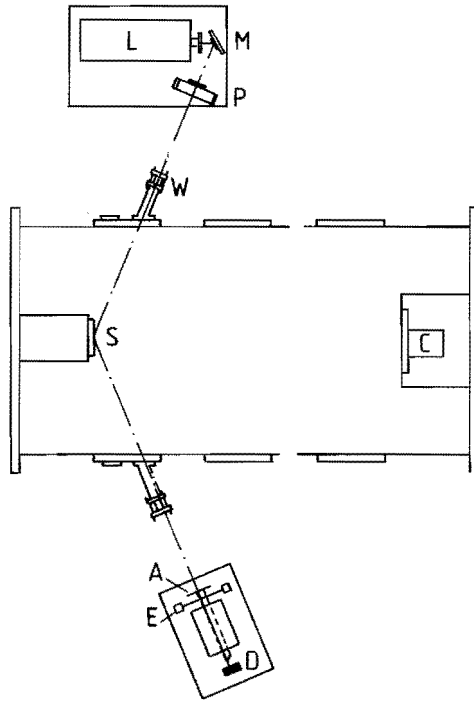


Fig. 3.15. Setup of the *in-situ* He-Ne ellipsometer. Components: laser L, mirror M, polarizer P, window W, substrate s, analyzer A, optical encoder E and detector D.

make sure that the fluctuations of the output power of the laser cannot cause any important inaccuracies an intensity- and frequency stabilized He-Ne laser has been used as a light source [KRO-81]. Since the light of the laser is linearly polarized a circular polarizer is added. Dichroic sheet polarizers are used for analyzer and polarizer. The optical axis of the polarizer is set at an angle of 45 degrees with the p- respectively s-direction of the sample. The angle of incidence is measured by adding a thin piece of glass mounted on a precision rotator in the light beam very close to the sample. First the reflected beam is directed precisely back into the laser. Then the piece of glass is rotated until the reflected beam is parallel to the transmitted beam. The angle of rotation of the piece of glass that can be read from the precision rotator is now exactly equal to the angle of incidence.

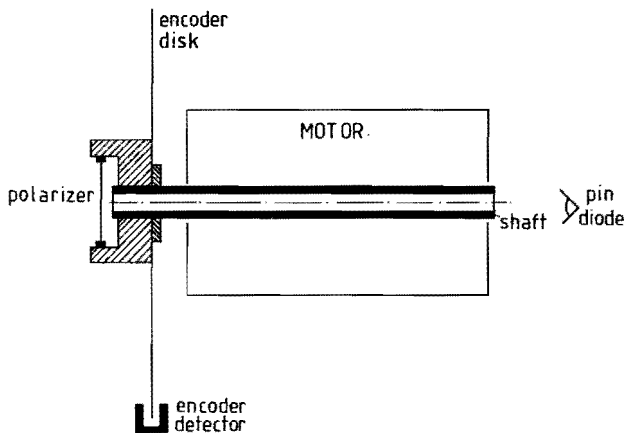


Fig. 3.16. Mounting of the rotating analyzer.

The windows of the vacuum system that are passed by the laser beam are mounted on bellows in order to be able to adjust them to a position perpendicular to the laser beam.

The analyzer is mounted on the axis of a motor with a hollow shaft (see fig. 3.16). An optical encoder which generates 256 TTL-pulses each rotation is also attached to the motor axis. The pulses trigger a 12-bit ADC which samples the signal produced by the detector, an EG+G SGD 100A pin diode. The encoder also generates 2 extra pulses each rotation that are used to calibrate the exact position of the analyzer. The signal $I(t)$ as a function of the time t can be written as (see section 4.3)

$$I(t) = I_0 (1 + a \cos(2\omega_0 t) + b \sin(2\omega_0 t)) \quad (3.6)$$

where ω_0 denotes the angular rotation frequency of the analyzer, and a and b the relative Fourier components of the signal. I_0 , the DC-level of the signal is not used in the data reduction process. Only a and b are needed.

The spectroscopic ellipsometer also has the PSA configuration (see figure 3.17). A cascaded arc in argon is used as a light source. The arc design is identical to the one described in section 3.2.1. The diameter of the arc channel is in this case 3 mm, the arc current is 25 A, and the argon pressure is 1 bar. Under these

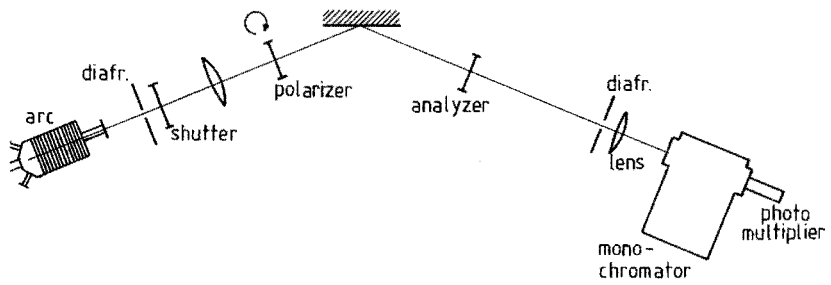


Fig. 3.17. Setup of the spectroscopic ellipsometer.

conditions the plasma will be close to LTE at a temperature of about 11000 K. Especially in the UV-region the spectral emittance is very high. One of the advantages of this light source over conventional sources like xenon short arcs is that the light it emits is not polarized by the envelope, since only flat, parallel quartz windows are used. The birefringence of the window material does not give any problems because the arc light itself is unpolarized. Another advantage is the plasma volume. Because of the small apertures that are generally used in ellipsometry (in our case 1/200) the focal length is large. Since the arc plasma has the shape of a cylinder a large fraction of the plasma volume is imaged on the entrance slit of the monochromator. Matrix calculations yield that 80 % of the plasma volume is used. The arc is imaged on the sample by means of a telecentric system with unity magnification. Diafragma D_2 determines the opening angle of the beam, where diafragma D_1 (the anode nozzle) delimits the size of the illuminated spot on the sample. The focal point on the sample is imaged on the entrance slit of the 0.25 m Jobin-Yvon monochromator by lens L_2 . The linear magnification is 1/20. This means that the light beam at the entrance of the monochromator has an aperture of 1/10 and the image size on the slit is 0.15 mm. This yields a spectral width of about 0.5 nm.

The polarizer and analyzer are Glan-Taylor birefringent polarizing prisms made of calcite (Halle). In this case the analyzer is set to an angle of 45 degrees with the p- and s direction of the sample and the polarizer is rotating. Similar to the He-Ne ellipsometer an optical encoder is calibrating the exact position of the polarizer. The photomultiplier (RCA IP28A) current is converted into a voltage by a series resistor, and the signal is amplified further by a programmable gain

amplifier (PGA). The supply voltage of the photomultiplier is adjusted to give a constant signal level. The dark current is calibrated by closing the electronic shutter S_1 . The signal to noise ratio is about 1000 over most of the covered spectral area (200–600 nm). In this case the signal $I(t)$ as a function of time has exactly the same form as in the case of the He–Ne ellipsometer (see eq. 3.6) so the data reduction procedure is identical.

The wavelength transmitted by the monochromator is set by a stepper motor controlled by a M6800 microcomputer system, connected to the M68000 interface controller. When the wavelength becomes larger than 400 nm a second order filter has to be added that eliminates all radiation below 400 nm.

The fixed analyzer is mounted on a stepper motor controlled precision rotator (0.01 degree per step). This allows very accurate determination of the plane of incidence. The alignment procedure for the analyzer will be discussed in section 4.3.2.

The total system can operate comparatively fast: changing a sample takes 5 seconds, automatic determination of the plane of incidence takes 1.5 minute and recording a spectrum from 200 to 700 nm (with a wavelength step of 10 nm) takes about 5 minutes.

3.4.2 Data reduction

As already stated both ellipsometers yield a signal $I(t)$ as a function of time t following eq. 3.6:

$$I(t) = I_0 (1 + a \cos(2\omega_0 t) + b \sin(2\omega_0 t)) . \quad (3.6)$$

The relative sinus- and cosine coefficients a and b can be determined in various ways. We have chosen two methods: Fourier transform and block transform [ZEE–85]. The transformation formulas are:

$$a = \frac{\int^T I(t) \cos(\omega t) dt}{\int^T I(t) dt} \quad (3.7)$$

$$b = \frac{\int^T I(t) \sin(\omega t) dt}{\int^T I(t) dt} \quad (3.8)$$

for the Fourier transform, and

$$a = \frac{\int_{-T/4}^{-T/2} I(t) dt + \int_{-T/4}^{T/4} I(t) dt - \int_{T/4}^{T/2} I(t) dt}{\int_{-T/2}^{T/2} I(t) dt} \quad (3.9)$$

$$b = \frac{\int_{-T/2}^0 I(t) dt + \int_0^{T/2} I(t) dt}{\int_{-T/2}^{T/2} I(t) dt} \quad (3.10)$$

where

$$T = 2\pi/\omega \quad (3.11)$$

for the block transform. Figure 3.18 illustrates the relative sensitivity of Fourier and block transforms for frequency ω . It is clear that the Fourier transform completely suppresses all higher harmonics whereas the block transform only suppresses the even harmonics completely. The odd harmonics are in that case attenuated, but they can still influence the measurements if non-linearities occur in the data acquisition system. The block transform however has the advantage that it essentially consists of a number of additions, and does not need a cosine table. Therefore it can be made to run very fast on microcomputers.

So by applying either Fourier transform or block transform the number of numbers that has to be stored per half evolution of the polarizer (or analyzer) is reduced to two. When very fast operation is required, as with in-situ measurements, the block transform is used. The small loss in accuracy is then taken for granted. When there is time enough however, Fourier transform is used (e.g. when a spectrum is recorded).

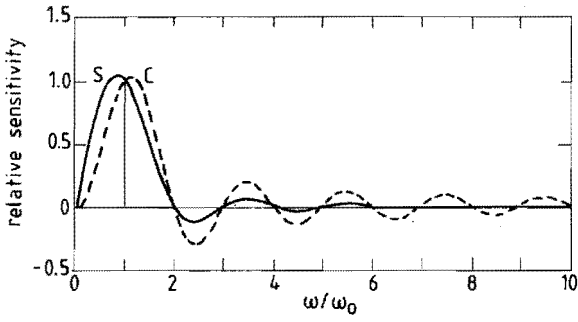
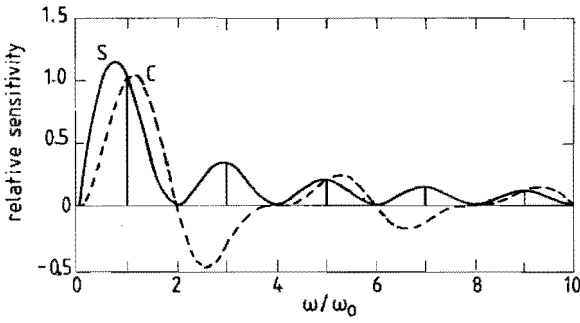


Fig. 3.18. Relative sensitivities of Fourier (upper graph) and block (lower graph) transforms. The full curves represent the sine transform (s) and the dashed curves the cosine transform (c).



4 DIAGNOSTICS

4.1 Introduction

In this chapter the physical principles of the various diagnostics will be discussed. To determine the electron density, the gas temperature, the gas velocity and the electron temperature as a function of the position in the plasma several optical methods have been used, like Stark broadening, Doppler broadening, Doppler shift and line-continuum ratio. They will be discussed in section 4.2, together with some other techniques that are used to study the plasma. Ellipsometry has been employed to monitor the growth of the carbon film, but also to perform a spectral analysis of the deposited material. This technique will be presented in section 4.3.

4.2 Plasma diagnostics

4.2.1 Broadening and shift of spectral lines

The wavelength-dependent intensity profile of a spectral line emitted in the plasma is determined by several physical effects. Each effect can result in a shift of the line position and/or in a broadening of the profile, with either a Lorentz- or a Gauss-like contribution. If the intensity profile $I(\omega)$ is normalized to 1 according to

$$\int_{-\infty}^{\infty} I(\omega) d\omega = 1, \quad (4.1)$$

a Gauss profile $I_g(\omega)$ with central frequency ω_0 and $1/e^2$ -width $\Delta\omega_d$ is represented by

$$I_g(\omega) = \frac{1}{\Delta\omega_d\sqrt{\pi}} \exp\left(-\left(\frac{\omega-\omega_0}{\Delta\omega_d}\right)^2\right) \quad (4.2)$$

and a Lorentz profile $I_l(\omega)$ with a half width γ similarly by

$$I_l(\omega) = \frac{\gamma}{2\pi} \frac{1}{(\omega - \omega_0)^2 + (\gamma/2)^2}. \quad (4.3)$$

If several broadening effects occur simultaneously the line profiles have to be convoluted. The convolution of two Gauss profiles is also a Gauss profile, and the convolution of two Lorentz profiles is again a Lorentz profile. In the case of Gauss profiles the widths have to be added quadratically, in the case of Lorentz profiles linearly. When a Gauss profile (eq. 4.2) is convoluted with a Lorentz profile (eq. 4.3) a Voigt profile results. Two Voigt profiles convolute to again a Voigt profile.

The spectral lines emitted by the plasma show Doppler broadening. The thermal movements of the radiating atoms cause a Doppler shift in all observed frequencies. If the velocity distribution is taken Maxwellian with a temperature T , then the line profile has a Gaussian shape with a full width at half maximum (FWHM) γ (in meters) according to

$$\gamma = \lambda_0 \sqrt{8 \ln 2} \sqrt{kT/mc^2} \quad (4.4)$$

where m denotes the atomic mass. If all the atoms have an average velocity component v in the direction of the observer the wavelength of the spectral line appears to be shifted over a range $\Delta\lambda$, with

$$\Delta\lambda = -\lambda_0 v/c \quad (4.5)$$

where c denotes the velocity of light.

The natural line width γ_n is determined by the lifetimes τ_i and τ_j of the upper and lower levels of the transition respectively. The shape is Lorentzian.

$$\gamma_n = \tau_i^{-1} + \tau_j^{-1} \quad (4.6)$$

The Stark effect is caused by interaction of charged particles and the radiating atom, and usually results in a Lorentzian line broadening profile (with the prominent exception of hydrogen atoms). The width is proportional to the electron density. Griem has accumulated the Stark parameters for a large number of atomic transitions [GRI-64]. For the 420.0 nm argon line that is used in the experiments the Stark width is about 60 fm.

In the case of hydrogen also ion broadening has to be taken into account. Griem calculated the total width of the hydrogen lines as a function of electron

density [GRI-74]. The result is given by:

$$n_e = C \Delta\lambda^{3/2} \quad (4.7)$$

where C is a constant that only slightly depends on the electron temperature, and $\Delta\lambda$ is the full width at half maximum of the line. For the H_β line ($\lambda = 486.1$ nm), for $T_e = 1$ eV, C values $1.2 \cdot 10^{22} \text{ m}^{-3} \text{ nm}^{3/2}$. The other broadening mechanisms, like resonance broadening, van der Waals broadening, etc, all yield negligible contributions to the line broadening.

4.2.2 Line to continuum ratio

The emissivities of line- and continuum radiation, ϵ_l and ϵ_c respectively, can be written as:

$$\epsilon_l(T_e) = n_p A_{pq} (h\nu/4\pi) P_1 = n_p r_{4s} \exp\left(-\frac{E_{1p}}{kT_e}\right) A_{pq} (h\nu/4\pi) P_1 \quad (4.8)$$

$$\epsilon_c(T_e) = C_1 \frac{n_e n_i}{\lambda^2 \sqrt{T_e}} (G_1(\lambda, T_e) + (1 - \exp(-h\nu/kT_e)) \xi_1) \quad (4.9)$$

- where:
- n_p : density of excited level
 - r_{4s} : collisional radiative coefficient
 - E_{1p} : *excitation* energy of level p
 - A_{pq} : transition probability
 - P_1 : normalized line profile
 - C_1 : constant ($1.63 \cdot 10^{-43} \text{ W m}^4 \text{ K}^{\frac{1}{2}} \text{ sr}^{-2}$)
 - G_1 : Gaunt factor ($\approx 1.2 \exp(-h\nu/kT_e)$ at $\lambda=420.0$ nm)
 - ξ_1 : Biberman factor (≈ 1.55 at $\lambda=420.0$ nm)
 - $n_i = n_e$: ion density (only singly charged ions are taken into account).

Taking into account the convolution of both emissivities with the apparatus profile, the line to continuum intensity ratio in the top of the line profile can be calculated. The collisional radiative coefficient r_{4s} is not known accurately for high electron densities and low electron temperatures. Preliminary calculations

[KRO-83] yield values between 0.1 and 1. Therefore the interpretation of the intensity ratios into temperatures has been carried out by taking r_{4s} equal to 1. This is equivalent to the assumption that the argon ion ground level is in Boltzmann-equilibrium with the excited levels. Figure 4.1 illustrates the line to continuum ratio for an argon ion line ($\lambda=480.6$ nm). So, if the electron density is known, the electron temperature can be evaluated.

4.2.3 Plasma conductivity

The electrical conductivity of the plasma in the arc channel according to Frost is given by [FRO-61, VAL-84]:

$$\sigma = \frac{4\pi n_e e^2}{3 k T_e} \int_0^{\infty} \frac{v^4 f_m}{\nu^f} dv \quad (4.10)$$

where

$$\begin{aligned} \nu^f &= \nu_{e0} + \nu_{ei}^f = \\ &\nu_{e0} + 0.476 \frac{0.582}{\gamma_e} \frac{8\pi}{v^2} \left[\frac{e^2}{4\pi\epsilon_0 m_e} \right]^2 \langle z \rangle n_e \ln \Lambda \left[\frac{m_e}{2 k T_e} \right]^{\frac{1}{2}}, \end{aligned} \quad (4.11)$$

- and:
- ν_{e0} : electron-neutral collision frequency
 - ν_{ei}^f : electron-ion collision frequency according to Frost
 - γ_e : peaking factor to compensate for anisotropy in the velocity distribution [SPI-56]
 - v : electron velocity
 - $\ln \Lambda$: Coulomb logarithm
 - $\langle z \rangle$: effective charge of the ions [VAL-84]
 - f_m : reduced Maxwell distribution

Equation 4.11 has been evaluated and the result is illustrated in figure 4.2.

The experimental value of the conductivity is drawn from an approximation assuming a homogeneous current distribution over the effective channel diameter:

$$\sigma_{exp} = Id / (\pi R^2 \Delta V) \quad (4.11)$$

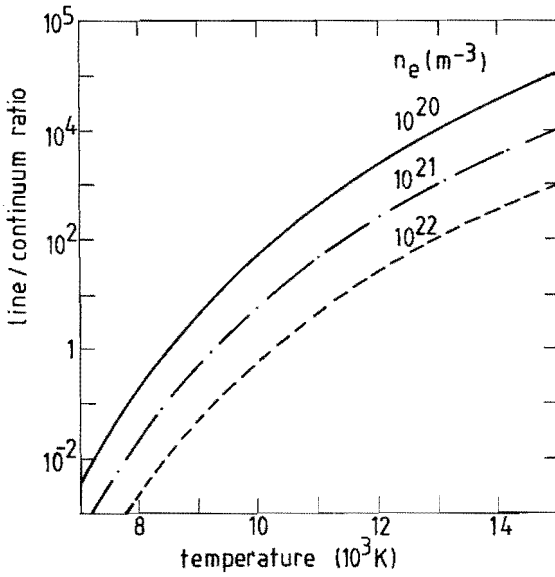


Fig. 4.1. Ratio of line and continuum emissivities ($\lambda=480.6$ nm) as a function of electron temperature for three values of the ratio of the electron density and the collisional radiative coefficient r_{4p}

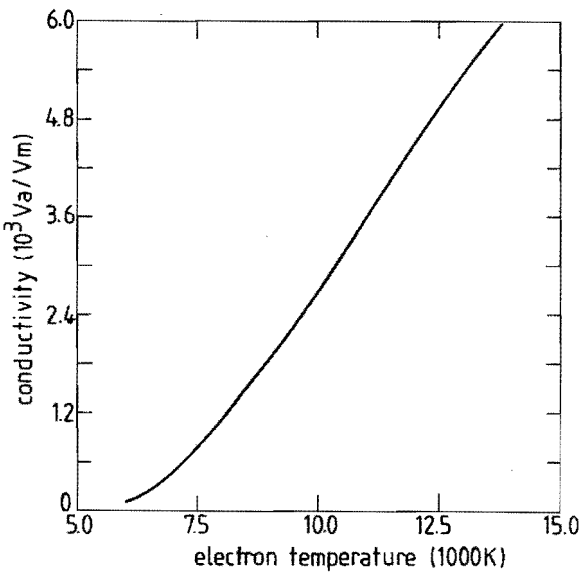


Fig. 4.2. Plasma conductivity as calculated with Frost's mixing rule as a function of electron temperature.

where I denotes the arc current, d the distance of two adjacent cascade plates, ΔV the potential difference between those two plates, and R the effective channel radius (about 0.9 times the real channel radius [TIM-84]).

4.3 Ellipsometry

4.3.1 Reflection of light on stratified structures

If a monochromatic light wave is reflected at an interface between two media with refractive indices n_1 respectively n_0 (see figure 4.3) the p- and the s-components behave differently. The reflection ratios r_p and r_s are dictated by the Fresnel coefficients:

$$r_p = \frac{n_1 \cos(\phi_0) - n_0 \cos(\phi_1)}{n_1 \cos(\phi_0) + n_0 \cos(\phi_1)} \tag{4.13}$$

$$r_s = \frac{n_1 \cos(\phi_1) - n_0 \cos(\phi_0)}{n_1 \cos(\phi_0) + n_0 \cos(\phi_1)} \tag{4.14}$$

Note that the sign of r_s is deviating from the conventions in the literature [HEC-74] because of a different definition of the direction of the s component.

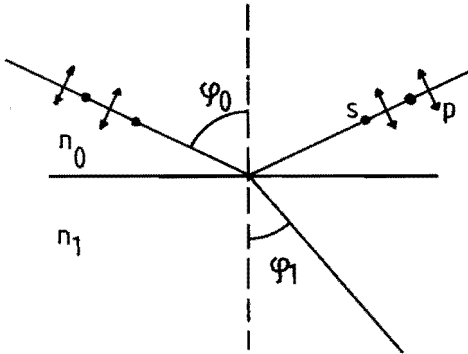


Fig. 4.3. Reflection of light at an interface between two media with different refractive indices (n_0 and n_1).

This is done for mathematical convenience and will be corrected for later. With the definition of the impedance factors g_{si} and g_{pi} [PER-84] for a material with refractive index n_i according to

$$g_{pi} = \frac{n_i}{\cos(\phi_i)} = \frac{n_i^2}{\sqrt{(n_i^2 - n_0^2 \sin^2(\phi_0))}} \quad (4.15)$$

$$g_{si} = n_i \cos(\phi_i) = \sqrt{(n_i^2 - n_0^2 \sin^2(\phi_0))} , \quad (4.16)$$

the Fresnel equations 4.13 and 4.14 can be simplified to

$$r_p = \frac{g_{p1} - g_{p0}}{g_{p1} + g_{p0}} , \quad r_s = \frac{g_{s1} - g_{s0}}{g_{s1} + g_{s0}} . \quad (4.17)$$

Now the mathematical shape of r_p and r_s is identical. If the surface is covered with a film (fig. 4.4) the situation is more complex. Interference can occur inside the film. Define the phase thickness β_i of film i by

$$\beta_i = (2\pi d_i n_i \cos(\phi_i)) / \lambda = g_{si} 2\pi d_i / \lambda . \quad (4.18)$$

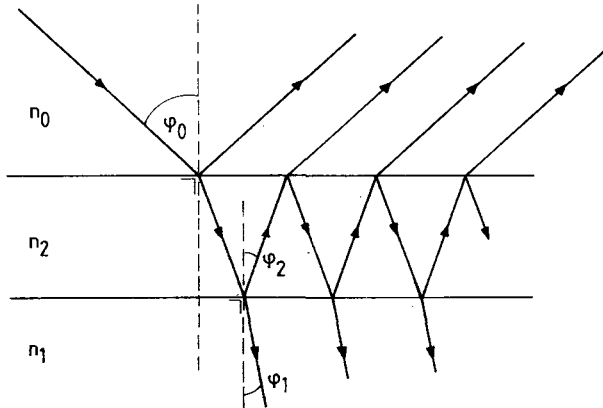


Fig. 4.4. Reflection and interference of light in a single layer system.

If now the complete system of substrate and film is looked upon as a new, semi-infinite substrate with impedance factor g_x (g_{sx} and g_{px} for s and p -components respectively), and if the internal reflections in the film are added, then

$$g_x = g_2 \frac{1 + u}{1 - u}, \quad (4.19)$$

where

$$u = \frac{g_1 - g_2}{g_1 + g_2} \exp(-2j\beta_2). \quad (4.20)$$

If more films are present this procedure can be repeated for each film, starting with the first one that contacts the semi-infinite substrate.

From the impedance factor g_x the reflection ratios r_{ox} can be calculated by

$$r_{ox} = \frac{g_x - g_o}{g_x + g_o}. \quad (4.21)$$

If the ellipsometric angles Ψ and Δ and the complex reflection ratio ρ are defined by

$$\rho = \tan(\Psi) \exp(j\Delta) = -r_p/r_s, \quad (4.22)$$

then the refractive index n_x of a semi-infinite substrate x is expressed by

$$n_x = n_o \tan(\phi_o) \left[1 - \frac{4\rho}{(1+\rho)^2} \sin^2(\phi_o) \right]^{\frac{1}{2}}. \quad (4.23)$$

Equation 4.22 differs from the conventional definition ($\rho = \tan(\Psi)\exp(i\Delta) = r_p/r_s$) in a minus sign. This is done to correct for the deviating definition of the s -direction. If the media i show anisotropic behavior, that is, if the refractive indices n_{pi} and n_{si} for waves parallel resp. perpendicular to the surface plane are not identical, then the impedance factors g_{si} and g_{pi} are defined by

$$g_{si} = n_{si} \cos(\phi_{si}) = \sqrt{(n_{si}^2 - n_o^2 \sin^2(\phi_o))} \quad (4.24)$$

$$g_{pi} = \frac{n_{si}}{\cos(\phi_{pi})} = \frac{n_{pi} n_{si}}{\sqrt{(n_{pi}^2 - n_o^2 \sin^2(\phi_o))}} \quad (4.25)$$

and the phase thicknesses β_{si} and β_{pi} by

$$\beta_{\text{si}} = 2\pi g_{\text{si}} d_i / \lambda \quad (4.26)$$

$$\beta_{\text{pi}} = 2\pi n_{\text{si}}^2 d_i / (g_{\text{pi}}\lambda) . \quad (4.27)$$

Ellipsometers measure the complex ratio ρ . Therefore, if the substrate is semi-infinite, its complex refractive index can be calculated directly from the ellipsometer data. If films are present on the surface the total complex number ρ can be calculated with equations 4.15 to 4.22 (if necessary 4.23 to 4.27). Either a time-dependent profile or a spectrum of experimental values is fitted in a least squares procedure using the distance in the complex plane between the experimental and the theoretical reflection ratio (ρ_{exp} and ρ_{mod} respectively) as the error function. The film parameters like deposition rate, refractive index, optical bandgap, etc. can now be determined.

4.3.2 Fundamentals of the setup

The two used ellipsometer systems (see section 3.4.2) both have the polarizer-sample-analyzer (PSA) configuration. Figure 4.5 outlines the basic elements of the instruments. The light emitted by the source is polarized linearly by the polarizer in a direction that makes an angle P with the plane of incidence. After reflection at the sample it is polarized again by the analyzer in a direction A . In the He-Ne ellipsometer the analyzer is rotating, in the spectroscopic ellipsometer the polarizer rotates. The intensity $I(t)$ as a function of time t is expressed by

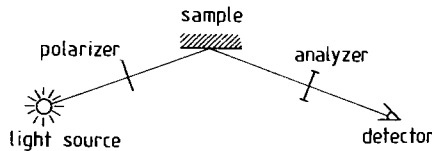


Fig. 4.5. Outline of the setup of a polarizer-sample-analyzer (PSA) ellipsometer. Either the polarizer or the analyzer is rotating.

$$\begin{aligned}
I(t) = I_0 (K_a K_s K_p) \{ & \cos 2A (\cos 2P (\rho\rho^\dagger+1) + (\rho\rho^\dagger-1)) + \\
& + \sin 2A \sin 2P (\rho-\rho^\dagger) + \\
& + \cos 2P (\rho\rho^\dagger-1) + \rho\rho^\dagger + 1 \} \quad (4.28)
\end{aligned}$$

where K_a and K_p represent the transmission coefficients of the polarizer and the analyzer respectively, and K_s is the total intensity reflection coefficient of the sample; ρ denotes the complex reflection ratio of the sample (see equation 4.22) and ρ^\dagger is the complex conjugate of ρ . It is clear that equation 4.28 is symmetrical in A and P , that is, if A and P are exchanged the equation remains identical. In the following we will assume that the analyzer is rotating with a constant frequency ω_0 (A increases linearly with time: $A=2\pi\omega_0 t$). This is the case in the He-Ne ellipsometer. If the polarizer is rotating instead, the formulas and the data interpretation do not change. If eq. 4.28 is splitted into Fourier components according to

$$I(t) = g (1 + \alpha \cos 2A + \beta \sin 2A) , \quad (4.29)$$

then the coefficients g, α and β are expressed by

$$\alpha = \frac{\cos 2P (\rho\rho^\dagger+1) + (\rho\rho^\dagger-1)}{\cos 2P (\rho\rho^\dagger-1) + (\rho\rho^\dagger+1)} = \frac{\cos 2P - \cos 2\Psi}{1 - \cos 2P \cos 2\Psi} \quad (4.30)$$

$$\beta = \frac{(\rho+\rho^\dagger) \sin 2P}{\cos 2P (\rho\rho^\dagger-1) + (\rho\rho^\dagger+1)} = \frac{\sin 2\Psi \cos \Delta \sin 2P}{1 - \cos 2P \cos 2\Psi} \quad (4.31)$$

$$\begin{aligned}
g &= I_0 (K_a K_s K_p) 2 \{ (1+\rho\rho^\dagger) \cos 2P (\rho\rho^\dagger-1) / (\rho\rho^\dagger+1) + 1 \} = \\
&= F K_s (1 - \cos 2P \cos 2\Psi) \quad (4.32)
\end{aligned}$$

where $F = I_0 (K_a K_p)^2$ does not depend on the sample. If the polarizer angle is chosen 45 degrees, then

$$\alpha = -\cos 2\Psi \quad (4.33)$$

$$\beta = \sin 2\Psi \cos \Delta \quad (4.34)$$

$$g = F K_s . \quad (4.35)$$

The signal $V(t)$ and its Fourier coefficients a and b that are measured by the data acquisition system (see section 3.4.2) can differ from the intensity $I(t)$ and its coefficients α and β . Let $1/\eta$ be the relative attenuation of the ac component of the signal readout with respect to the ac component of the intensity. Let θ be the phase angle between the two components. Then one can calculate from eq. 3.6 and eq. 4.29 that

$$\alpha = \eta (a \cos 2\theta + b \sin 2\theta) \quad (4.36)$$

$$\beta = \eta (- a \sin 2\theta + b \cos 2\theta) . \quad (4.37)$$

The attenuation η and the phase angle θ are calibrated with a method described by Aspnes [ASP-75]. If the polarizer angle P is set to zero then the intensity is expressed by

$$I(t) = F K_s (1 - \cos\Psi) (\cos 2A + 1) . \quad (4.38)$$

The relative modulation is now 100 %, i.e. the ac component amplitude equals the dc component. Now first the signal offset is nulled with covered light source. Then a series of residuals $r_j(P)$ is taken for a number of polarizer angles close to $P=0$, where

$$r_j(P) = 1 - a^2 - b^2 . \quad (4.39)$$

Aspnes has shown that the residuals follow a parabola:

$$r(P) = c_0 + c_1 P + c_2 P^2 \quad (4.40)$$

of which the minimum value r_{\min} is related to η by:

$$r_{\min} = 1 - \eta^{-2} = c_0 - c_1/4c_2 . \quad (4.41)$$

The location of the minimum defines the angle readout where actually $P=0$. The phase angle θ can be evaluated from a measurement of a and b at $P=0$:

$$\theta = \frac{1}{2} \tan^{-1}(b/a) \Big|_{P=0} . \quad (4.42)$$

The calibration procedure as described above is repeated each time a sample is exchanged. As already stated this procedure has been formulated for a rotating analyzer system, but the rotating polarizer system is mathematically equivalent. Therefore the data acquisition and calibration procedures are identical in the two systems.

5 RESULTS AND DISCUSSION

5.1 Introduction

This chapter presents the results of model calculations and diagnostics in the three basic sections: plasma production, transport to the substrate and deposition. Section 5.2 starts with the presentation of the calculated and measured axial profiles of the most relevant plasma parameters in the cascaded arc. Then the results of the calculations concerning the dissociation and ionization of the injected methane gas will be reviewed. Finally the electron temperature and the electron density at the location where methane is injected are presented as a function of the system parameters gas flow and arc current.

In section 5.3 the calculated profiles of electron density, gas velocity and gas temperature in the expansion zone are compared with the experimental values obtained with the various diagnostics. The development of the most important parameters concerning the chemical activity will be illustrated.

Section 5.4 presents the results of *in situ* ellipsometry. The deposition rates obtained will be compared with the model calculations.

Finally, section 5.5 gives a short review of the measurements concerning the quality of the deposited films.

Table 5.1 gives the macroscopic plasma parameters of the standard condition used. All measurements have been carried out at standard conditions or at conditions that differ from the standard condition in only one parameter.

Arc current	:	50 A
Argon flow	:	100 scc/s
Methane flow	:	1.85 scc/s
Arc diameter	:	4 mm
Pressure vacuum system	:	100 Pa

5.2 The cascaded arc

The plasma is flowing through the arc channel at a relatively large velocity. This flow is associated with a pressure drop. Friction with the wall causes the pressure to drop faster than would be expected for an accelerating duct flow without wall interaction. Figure 5.1 pictures the axial profile of the measured plasma pressure for three different gas flows. In the beginning of the channel the pressure drops linear with the axial position. At the end the decrease is more than linear because of acceleration of the plasma towards sonic conditions.

De Haas has numerically analyzed the equations (2.40) to (2.42) to evaluate the evolution of the gas pressure, the plasma velocity and the temperature in the case of a plasma in complete LTE. The wall friction is taken into account by the friction factor f . This numerical program has been used to evaluate f from the pressure measurements presented in figure 5.1. It appears that the friction factor is

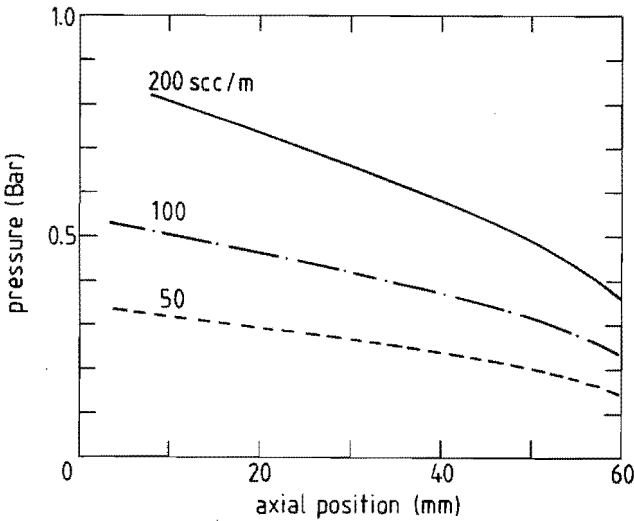


Fig. 5.1. Plasma pressure as a function of axial position in the arc channel. Parameter is the argon flow (50, 100 and 200 scc/s); 1 scc/s is defined as 1 cc/s at 1 bar and 273 K. The axial position is defined zero at the location of the cathodes at the beginning of the arc. The length of the channel (ending in the anode nozzle) is 60 mm.

not constant throughout the plasma channel. In the first part of the channel f has values around 0.11, independent of the gas flow. In the last part of the channel, close to the sonic plane, f has decreased to about 0.05. For large gas flows f appears to be slightly smaller than for small gas flows. In the case of perfect laminar flow the friction factor f can be expressed by [BEN-83]

$$f = \frac{64}{R_d}, \quad (5.1)$$

using the familiar Reynolds number R_d , based on the channel diameter D , defined by

$$R_d = \frac{\rho u D}{\eta}, \quad (5.2)$$

where η represents the viscosity coefficient. The viscosity coefficient η is taken from a table given by Vargaftik [VAR-75]. Figure 5.2 shows the viscosity as a function of temperature for a number of plasma pressures. Figure 5.3 compares the friction

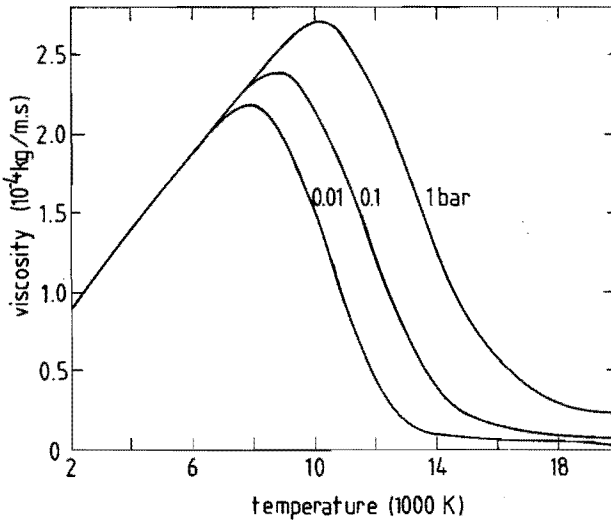


Fig. 5.2. Viscosity of an LTE argon plasma as a function of temperature for three different pressures. The values are taken from Vargaftik [VAR-75].

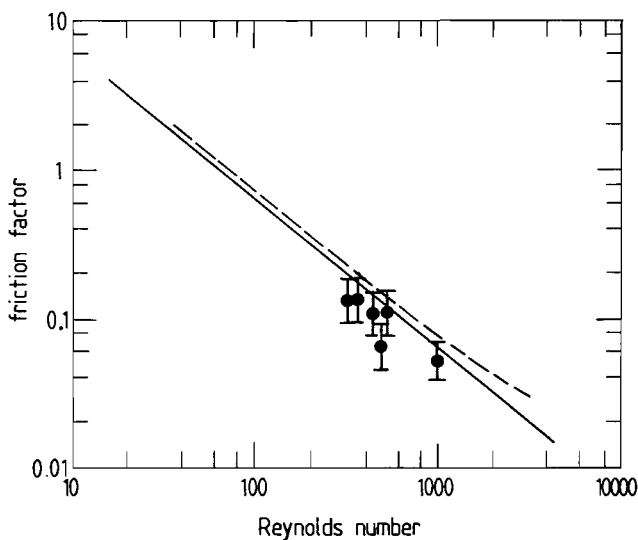


Fig. 5.3. The wall friction factor f plotted versus the Reynolds number. The full curve corresponds to the ideal laminar case ($f=64/R_d$) and the dashed curve represents the measurements without a plasma being present in the arc channel (room temperature) [HAA-87]. The points are obtained from measurements at the beginning and at the end of the channel for a number of discharge conditions.

factor as a function of the Reynolds number according to eq. (5.1) with accumulated values measured for the arc channel with and without [HAA-87] the plasma being present for a variety of gas flows. As only minor differences occur between the ideal curve according to eq. (5.1) and the experimental points, the corrections of the friction coefficient proposed by Prandtl and von Karman (described in Benedict's book [BEN-83]) for the transition towards turbulent flow are not needed. The flow can be regarded to be laminar. The fact that the points representing a flow with plasma are below the ideal curve might indicate that the viscosity coefficient shown in fig. 5.2 should be corrected for non-equilibrium effects.

In figure 5.4 the plasma potential is illustrated as a function of the axial position. Again an almost linear profile has been obtained. From the known current density and the theoretical values of the electrical conductivity the electron temperature has been estimated using this curve. The electron temperature has also been determined by line-continuum ratio. The differences between the results of the two methods are negligible. Figure 5.5 demonstrates the axial profile of the

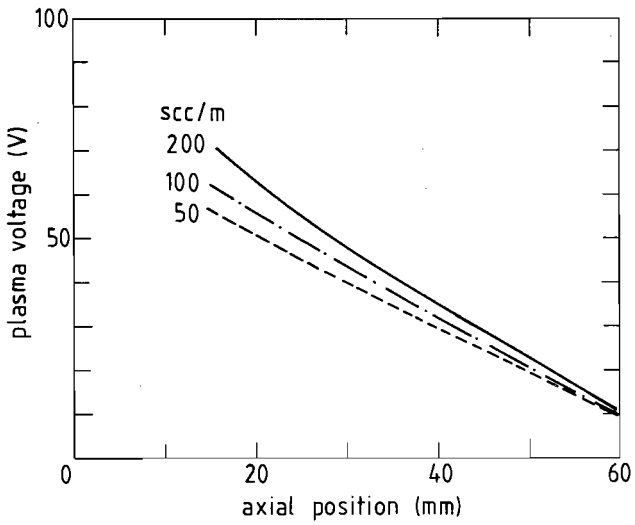


Fig. 5.4. The plasma voltage as a function of axial position in the arc channel. Parameter is the argon flow (50, 100 and 200 scc/s).

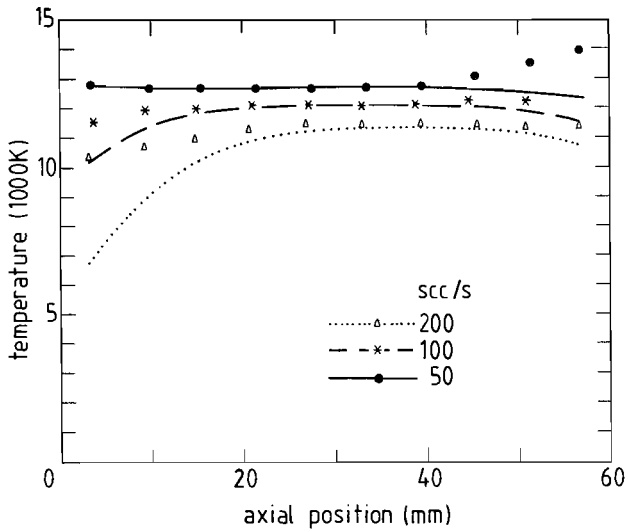


Fig. 5.5. The various temperatures as a function of axial position. Parameter is the argon flow (50, 100 and 200 scc/s). The points represent the values of the electron temperature as measured with line-continuum ratio, whereas the curves correspond to the calculations for the gas temperature.

experimentally determined *electron* temperature (points), as well as the profiles of the *gas* temperature as they are calculated using eq. (2.28) and (2.20) in combination with the measured profiles for pressure and electron temperature. Especially for large gas flows the gas temperature is initially lower than the electron temperature. The plasma needs about 20 mm of axial length to relaxate towards temperature equilibrium. For small gas flows this equilibrium is established almost instantaneously. At the end of the channel the gas temperature decreases because of acceleration of the flow.

The calculations also yield axial profiles of the electron density. In figure 5.6 the calculated profiles are compared with the results of measurements using the Stark broadening of the H_{β} line (486.1 nm), again for three values of the gas flow. The agreement between theory and experiment is good, the only exception occurring for a small gas flow at the end of the channel. Here the measured values are about 40 % lower than the calculated values. This might be an indication that for these conditions the assumption that the axial gradients are stronger than the radial gradients is no longer valid. Radial diffusion and recombination at the arc wall will lead to lower calculated densities.

The calculated profiles have been obtained by taking the first measured value of the electron density as a starting value, and adjusting the starting value of the gas temperature to give a best fit to the measurements. Once the starting conditions (in this case the electron density and gas temperature at the beginning of the arc channel) are set the complete axial profile is determined by Runge-Kutta integration of eq. (2.20) and (2.28).

A remarkable feature is that the measured electron density does not differ very much for the three values of the gas flow, in spite of the fact that the pressure does differ strongly (see figure 5.1). This can be explained by analyzing the electron energy balance terms in the first part of the arc channel. Equation 2.48 of chapter 2 represents the total electron energy equation without Ohmic input. If Ohmic input is included, and heat conduction, viscosity, radiative losses and expansion terms are neglected, the net electron energy balance reads:

$$j \cdot \underline{E} = n_e n_{ars} K_{1+} (b_1 - 1) E^{1+} + 3 \frac{m_e}{m_{ar}} n_e \left(\frac{1}{\tau_{e1}} + \frac{1}{\tau_{e0}} \right) k (T_e - T_h), \quad (5.3)$$

where the overpopulation b_1 of the argon neutral ground level is defined by

$$b_1 = n_{ar} / n_{ars}. \quad (5.1)$$

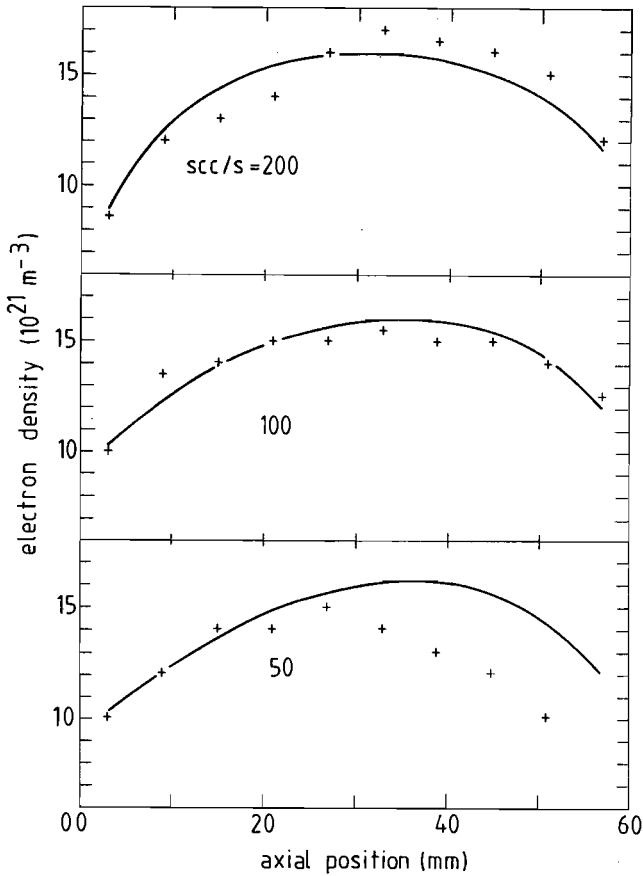


Fig. 5.6. Comparison of the measured (points) and calculated (curves) axial profiles of the electron density in the arc channel for three values of the argon flow (50, 100 and 200 scc/s).

The Saha density n_{ars} is defined by the modified Saha equation (2.9). The term on the left hand side represents the Ohmic heating, the terms on the right hand side represent the electron energy loss because of ionization of argon atoms and heat exchange between electrons and heavy particles because of elastic collisions respectively.

In words: the Ohmic input balances the heating of the heavy particles by electrons and the net ionization. With an Ohmic heating power of (in this case)

5.10^9 Wm^{-3} and a temperature difference between electrons and heavy particles of 3000 K (see figure 5.5), which leads to an energy exchange term of 3.10^9 Wm^{-3} , the overpopulation factor b_1 can be estimated to value around 60. In the beginning of the arc channel temperature equilibration takes about 60 % of the Ohmic input and ionization of argon atoms needs the other 40 %.

Figure 5.7 shows the axial profiles of the overpopulation factor as it is obtained from the measured electron densities (fig. 5.6) and gas pressures (fig. 5.1) in combination with the calculated gas temperatures (fig. 5.5). At the beginning of the arc channel this experimentally determined overpopulation factor values around 40, which agrees fairly well with the value estimated from the electron energy balance. At the end of the channel b_1 values around 10. The overpopulation factor b_1 essentially determines the net electron production by ionization of argon atoms by electron impact. Therefore we can conclude that at the beginning of the arc channel a large fraction (about 60 %) of the energy supplied to the plasma is used to heat the originally cold gas until its temperature equals the electron temperature. The remaining energy (around 40%) is used to ionize the argon atoms. This gives rise to a constant production of electrons and thus of ions. Once the gas is heated and

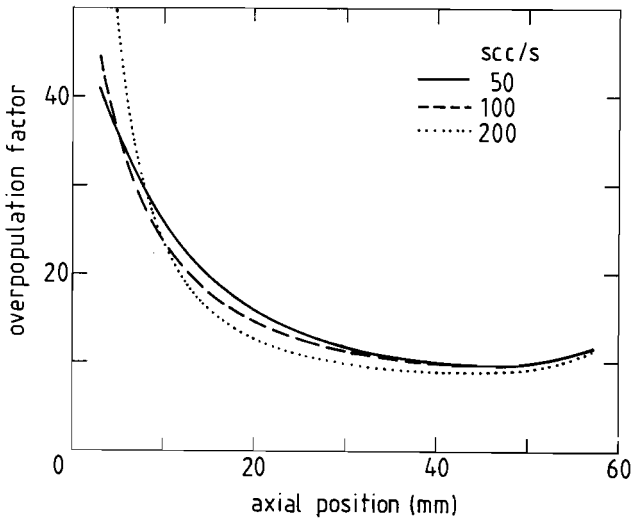


Fig. 5.7. The experimentally determined overpopulation factor b_1 of the argon neutral ground level as a function of axial position. Parameter is the argon flow.

ionized, the (now smaller) net electron- and ion production is compensated by expansion because of the pressure drop. While the total ion flux still increases slightly, the ion density does not.

The dissociation and ionization of methane following its injection into the channel are analyzed by numerical integration of the equations (2.20), (2.29) and (2.31) to (2.39), using the experimentally determined values for electron density, pressure and electron temperature. Figure 5.8 illustrates that the injected species are heated until they have the same temperature as argon atoms (and electrons). The temperature of the argon atoms decreases slightly because of the energy they lose while dissociating the methane fragments. Full temperature equilibration takes place at a length scale of about 10 mm. With a plasma velocity of ca. 2000 m/s this length is equivalent to a time of 5 μ s.

Figure 5.9 presents the evolution of the densities of the neutral and ionized fragments of methane. The electrons and the argon atoms are responsible for about 30% and 70% of the total number of dissociations respectively. The carbon atom density is relatively low at all positions. Resonant charge exchange with argon ions

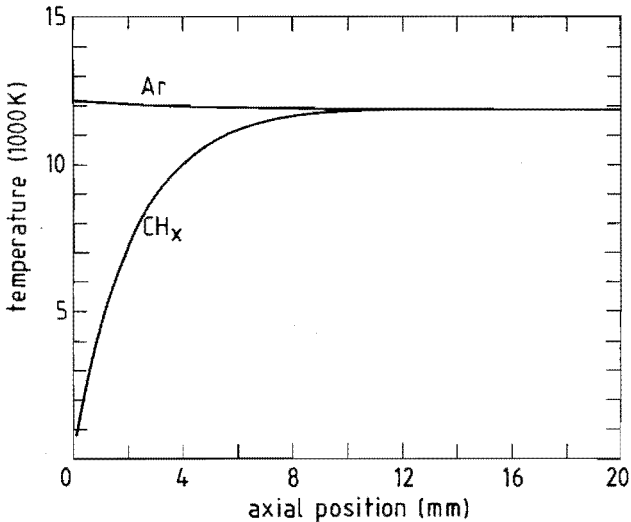


Fig. 5.8. Calculated axial temperature profiles for argon atoms and injected CH radicals.

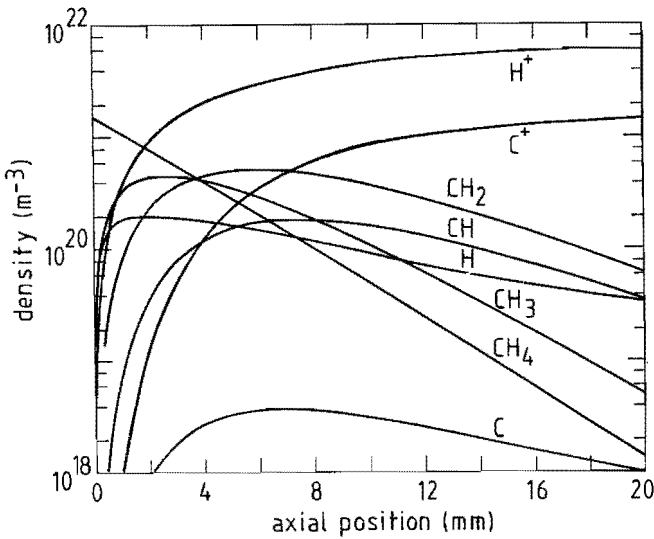


Fig. 5.9. Evolution of the densities of the various particles present in the plasma following the injection of methane in the arc channel. The axial profiles are calculated using the model developed in section 2.3.2.

eliminates the carbon atoms very efficiently after they have been produced by dissociation of CH. Figure 5.9 demonstrates that chemical equilibrium is established at a length scale of, again, 10 mm. Then methane is dissociated totally and carbon and hydrogen are ionized completely.

One has to notice that non-resonant dissociative charge exchange between argon ions and neutral CH_x fragments has not been included in the calculations. This could result in a quicker dissociation of methane and different developments of the several radical densities.

The equilibration length hardly depends on the temperature. This is shown in figure 5.10, where the carbon ion density is plotted as a function of the axial position in the arc channel for four values of the temperature. The temperature only slightly influences the equilibrium density. The gas pressure does have an influence on the equilibration length. Figure 5.11 pictures the evolution of the carbon ion density for a number of gas pressures. The injected percentage of methane is kept constant. At a pressure of 0.5 bar (occurring at a gas flow of 100 scc/s) the total length needed is 10 mm. At a pressure of 0.125 bar this length increases to about 40 mm. When the amount of methane is increased, the time needed to build up the

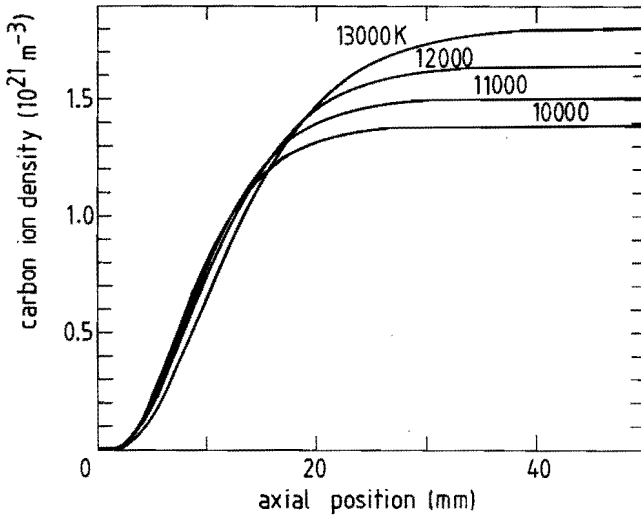


Fig. 5.10. Evolution of the carbon ion density following injection of methane. Parameter is the plasma temperature.

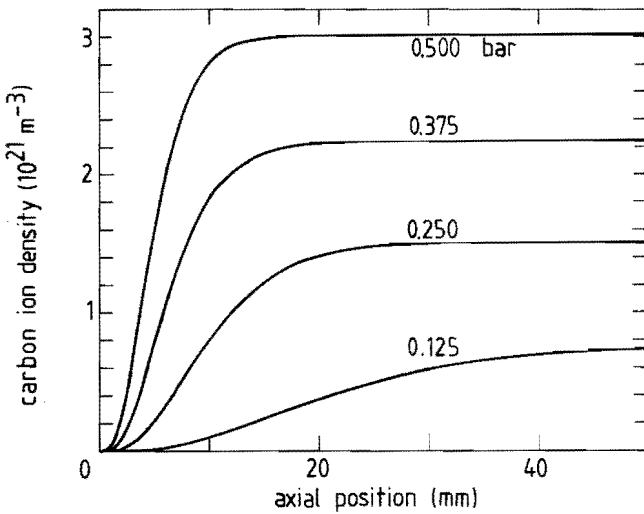


Fig. 5.11. Evolution of the carbon ion density following injection of methane. Parameter is the plasma pressure at the injection location.

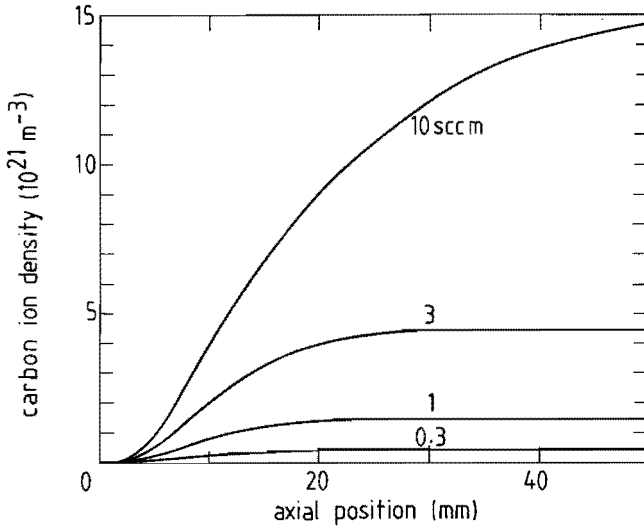


Fig. 5.12. Evolution of the carbon ion density following injection of methane. Parameter is the methane flow (0.3, 1, 3, and 10 scc/s).

carbon ion density hardly increases (see figure 5.12). Only when the admixed amount of methane approaches 10% (occurring at a flow of 10 scc/s) the equilibration time increases. In this case the argon ion density has been strongly decreased by charge exchange, and the ionization of carbon now is determined by collisional ionization by electron impact. In words: the injected flux of carbon atoms must be smaller than the argon ion flux for efficient production of carbon ions.

From the figures 5.1 to 5.12 the minimum arc length needed to obtain full ionization of the admixed methane can be estimated. Figures 5.1 to 5.6 demonstrate that about 30 mm is needed for heating and ionization of argon atoms. Figures 5.7 to 5.12 show that full dissociation and ionization of methane takes place at a length scale of 20 mm. Therefore, in this geometry the total arc length needed for complete dissociation and ionization of methane is about 50 mm.

Most of the measurements of which the results are presented in this chapter are carried out while methane is injected 5 mm upstream of the nozzle throat. Therefore the injected gas will not yet be dissociated completely. To be able to continue the calculations in the expansion the chemical plasma composition will be taken from the figures 5.8 and 5.9 at an axial position of 5 mm.

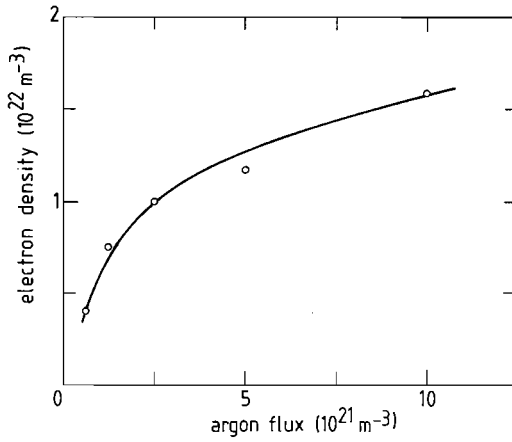


Fig. 5.13. Measured electron density versus argon flow.

The figures 5.13 to 5.16 show the measured electron density and electron temperature at the location where methane is injected in the plasma as a function of arc current and argon flux. A large argon flux causes the electron density to increase, but at the same time the temperature is decreased. Increasing the arc

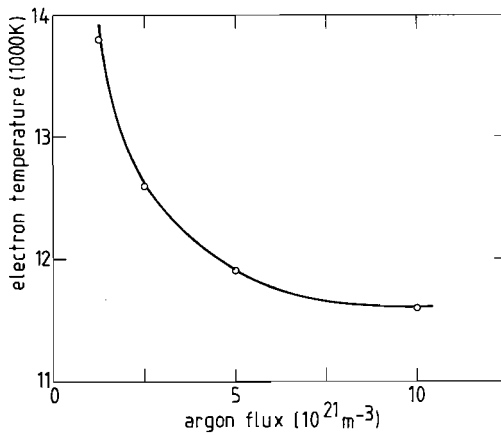


Fig. 5.14. Measured electron temperature versus argon flow.

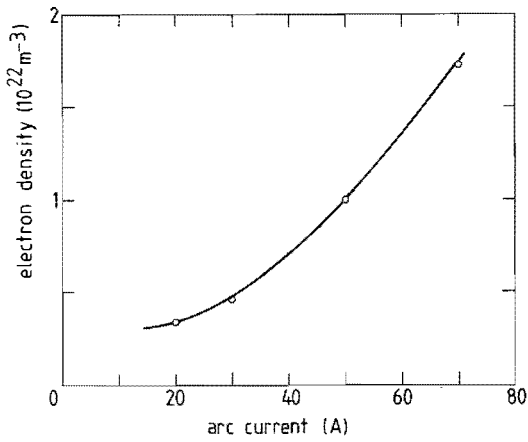


Fig. 5.15. Measured electron density versus arc current.

current results in an increase of the electron density as well as of the electron temperature.

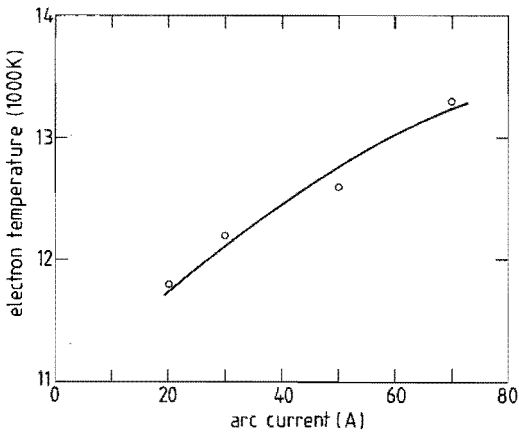


Fig. 5.16. Measured electron temperature versus arc current.

5.3 The expansion.

In the expansion of the plasma into the vacuum system the temperature and velocity of the argon atoms have been determined by Doppler spectroscopy. Figure 5.17 presents typical examples of normalized line profiles measured by the Fabry-Pérot interferometer. These profiles are subjected to Voigt-analysis on the laboratory computer to extract the Doppler shift and the Doppler width. The Doppler shift yields the gas velocity directly, whereas the Doppler width has to be extracted from the total Gaussian line width (taking into account the apparatus profile) to be able to calculate the gas temperature. Figure 5.18 shows the axial profiles of the centerline velocities of argon atoms and CH radicals for a number of discharge compositions. The argon velocity appears to be almost independent of the plasma composition. The sharp decrease in the velocity indicates the beginning of the shock wave. Note that the CH-radicals have their

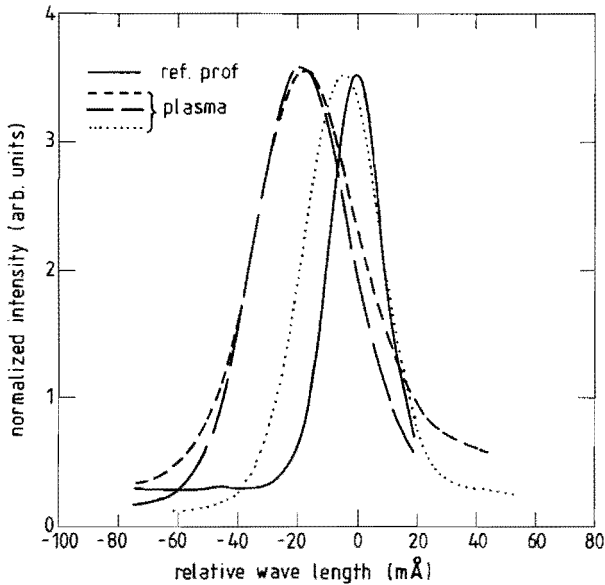


Fig. 5.17. Examples of normalized line profiles as measured with the Fabry-Pérot interferometer. Also shown is the reference profile (ref. prof.) as obtained from the low pressure argon lamp.

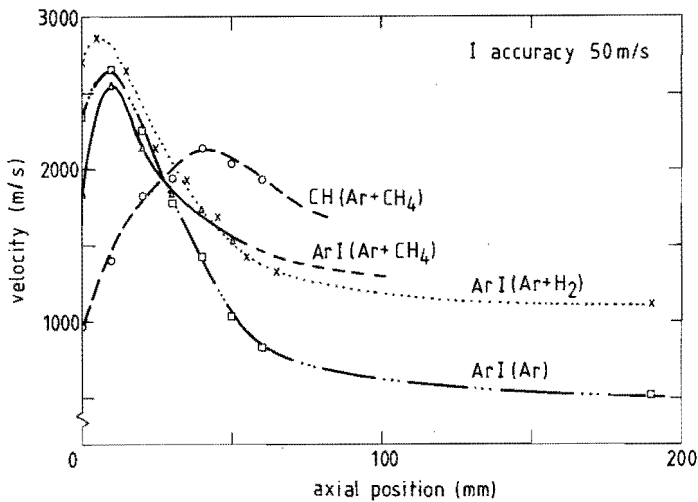


Fig. 5.18. The axial component of the measured velocity of argon atoms and CH radicals as a function of the axial position in the expansion. Three plasma compositions are shown: pure argon and argon with an admixture of 1 % of hydrogen or methane.

velocity maximum further downstream than the argon atoms. Because methane is in this case injected only 5 mm before the end of the arc channel the velocity of its fragments is not yet equal to the plasma velocity at the arc exit. It will continue to increase until the velocity of the argon atoms becomes smaller than the CH-velocity. Then also the CH-radicals slow down.

Figure 5.19 presents a three-dimensional impression of the velocity profile. The beam-behavior can be seen clearly in this graph: the width of the lateral velocity profile increases and the centerline velocity decreases when moving downstream. The same trend is observed with respect to the gas temperature (see figure 5.20). The electron density seems to behave somewhat differently (fig. 5.21). The centerline value decreases with increasing distance to the nozzle, but the width of the profile does not increase. The electron densities at the plasma boundary have values significantly smaller than $1 \cdot 10^{29} \text{ m}^{-3}$. As Griem's data [GRI-64] for the Stark parameters are only listed for larger values of the electron density an extrapolation has been used. It is not expected however that the error made in this extrapolation causes dramatic errors in the determined electron density. Therefore we might

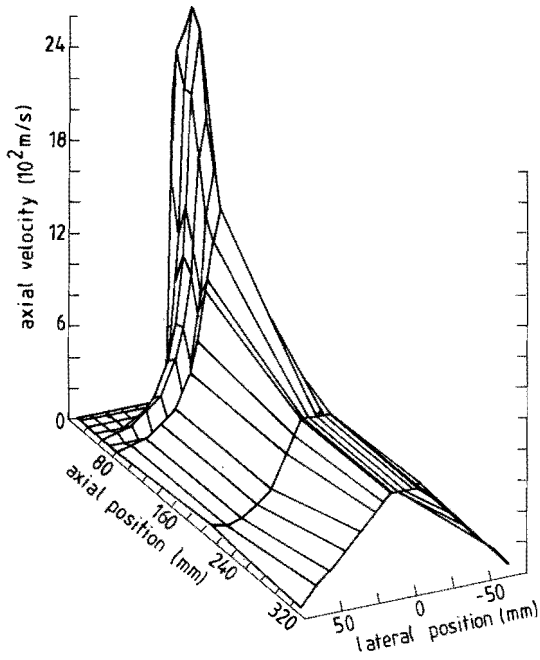


Fig. 5.19. Three-dimensional view of the spatial profile of the plasma velocity in the expansion of the arc plasma into the vacuum system.

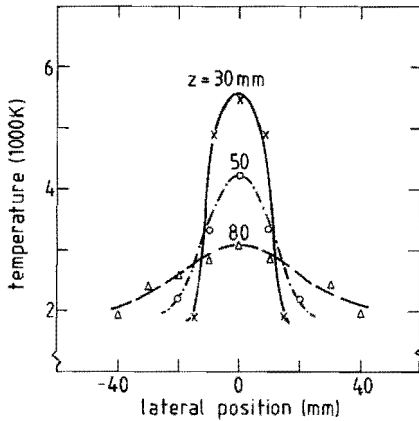


Fig. 5.20. The measured lateral profiles of the gas temperature at three axial positions (30, 50 and 80 mm).

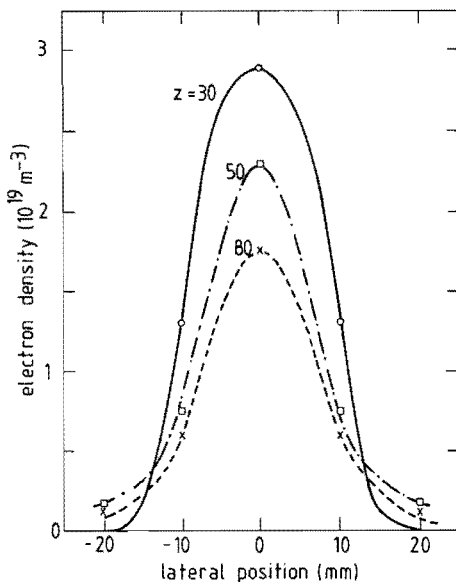


Fig. 5.21. The measured lateral profiles of the electron density at three axial positions (30, 50 and 80 mm).

conclude that the lateral profile of the electron density is narrower than the temperature profile.

Figure 5.22 presents the axial profile of the centerline values of the electron density. The local maximum at axial position $z = 50$ mm is not very pronounced but significant. It might again indicate the beginning of the shock wave. As the density decreases the inaccuracy (and the scatter in the experimental points) increases. In this region, similar to the previously mentioned plasma boundaries, Griem's data start losing their validity. After about 80 mm the electron density remains almost constant. The supersonic plasma expansion has come to an end.

In figure 5.23 the centerline axial profile of the gas temperature is given for an argon plasma with and without methane injected. Again a local maximum occurs at $z = 50$ mm, indicating the shock wave boundary. When methane is added at the end of the arc channel the temperature is lower than when no methane is added. This is caused by the energy the argon atoms lose while heating and dissociating the hydrocarbon molecules and radicals. The inaccuracy of the temperature values arising from noise and (slight) asymmetry in the line profiles (cf. figure 5.17) is

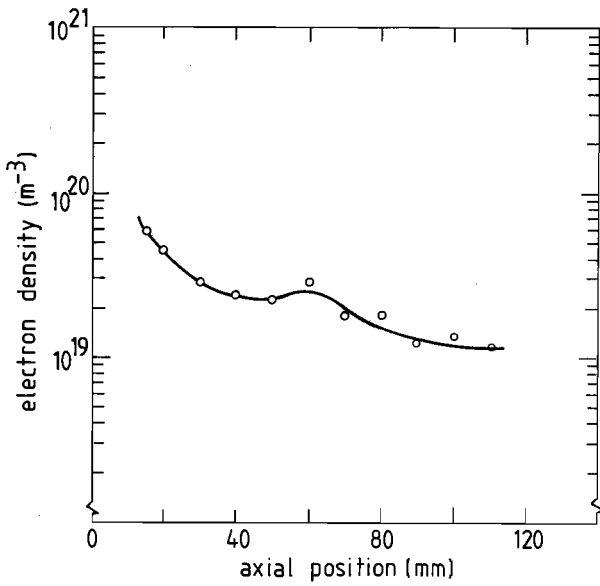


Fig. 5.22. Axial profile of the electron density as measured with H_β -broadening.

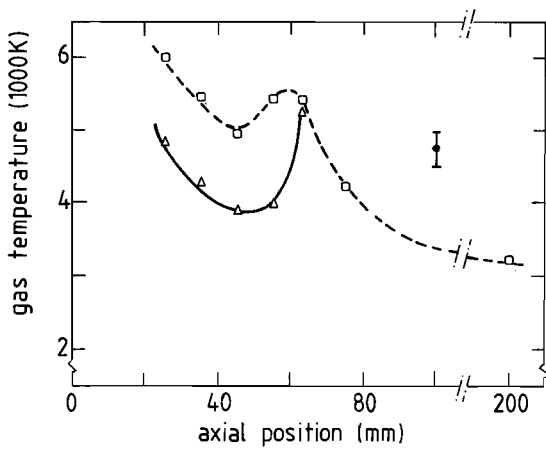


Fig. 5.23. Axial profile of the measured temperature of argon atoms in the supersonic expansion. The full and dashed curves represent a methane-seeded and a pure argon plasma respectively.

about 200 K. In the interpretation of the measurements however no Abel inversion has been used. As the intensity is observed to be higher at the plasma boundaries than in the center, the integration of the intensity in the detection volume (about 40 mm long, see fig. 3.13) might cause systematic deviations. If the temperature in the beam boundaries would be considerably higher than in the center (as often occurs in supersonic expansions surrounded by a shock wave) a lateral scan would give a flat profile. The experimentally determined lateral profiles however (fig. 5.20) do not show such an extremely flat behavior. Therefore the errors induced by lateral integration are believed to be small (of the order of 500 K).

The expressions derived in section 2.4 lead to a set of 13 coupled differential equations that are solved by Runge–Kutta integration using MicroSoft Pascal on an IBM PC/AT compatible. Figure 5.24 compares the calculated axial velocity profiles with the values measured by Doppler–shift. Measurements at the standard condition (100 Pa) and at a background pressure of 20 Pa are shown. There is a good

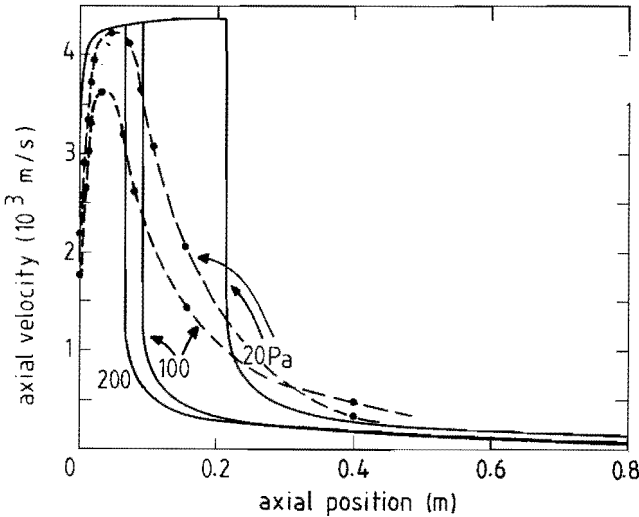


Fig. 5.24. Comparison of measured and calculated axial profiles of the plasma velocity in the supersonic expansion followed (after passing the shock wave) by the subsonic relaxation zone. Parameter is the background pressure (20, 100 and 200 Pa). The dashed curves and the points represent the measurements. The full curves correspond to the calculated profiles.

qualitative agreement between model and measurements, especially in the first (supersonic) part. In the supersonic part of the flow field the calculated profiles agree with the results of calculations by Chou and coworkers [CHO-67]. In the subsonic relaxation zone the velocity profile agrees qualitatively with centerline profiles calculated by Witze [WIT-74]. Poissant and Dudeck found an identical profile in the subsonic part. The model predicts the position of the shock wave (at standard conditions) at $z = 80$ mm, whereas the measurements indicate that the shock starts at about 50 mm. In the relaxation zone just after the shock the measured and calculated velocities differ by a factor 3. The integration over the detection volume implies in this case not only a lateral integration over 40 mm, but also an axial integration over ca. 20 mm. The measured axial profile is therefore integrated over 20 mm. This length is much smaller than the length scales over which the velocity changes (at least in the subsonic relaxation zone), so the errors are small. In the relaxation zone the measured gradients are much smaller than the calculated ones. This is probably caused by the omission in the models of viscosity and of convective currents. Both phenomena have a smoothing effect on the velocity profile.

It is observed that the quasi one-dimensional model yields results that agree qualitatively with the measurements. Although the expansion is essentially three-dimensional, quasi one-dimensional calculations predict the location of the shock wave and the trends in the axial velocity profile fairly well.

The calculated axial profile of the electron density is shown in figure 5.25 together with the measurements (cf. fig. 5.22). Again there is a good agreement between model and experiment. After having passed the shock wave the electron density increases in the relaxation zone because of deceleration and cooling of the plasma. After some time three-particle recombination starts to eliminate electrons and ions. This is illustrated clearly in figure 5.26. Here the axial profile of the total electron flux is plotted. Again the experimental points (in the supersonic part) approximately fit the model curves. Poissant and Dudeck [POI-85] used crossed electrostatic probes to determine the plasma parameters in a supersonically expanding argon arc. They found similar axial profiles for the electron density, including the increase in the first part of the relaxation zone. Goldfarb [GOL-68] also reported an increase of the electron density in a paper discussed by Igra [IGR-75]. In the supersonic part the profiles are similar to those obtained by Jenkins [JEN-71], Bowen et al. [BOW-71] and Chou and coworkers [CHO-67].

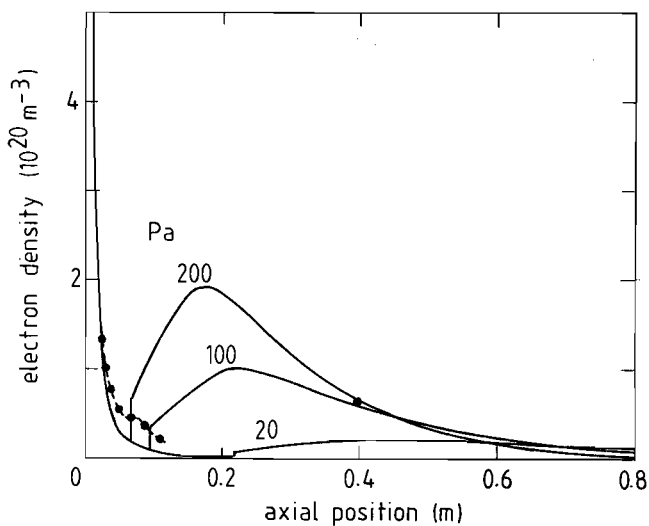


Fig. 5.25. The measured (points and dashed curve) and calculated axial profiles of the electron density in the plasma expansion. Parameter is the background pressure.

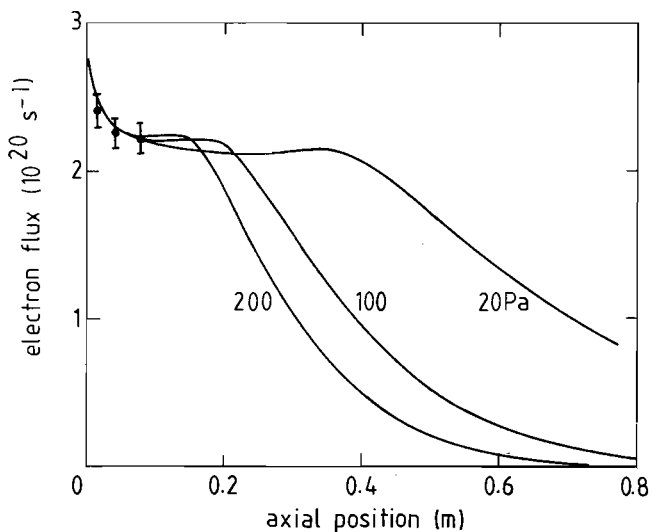


Fig. 5.26. The calculated (full curves) and experimentally obtained (points) axial profiles of the total electron flux. The electron flux $\phi_e(z)$ is defined as $\phi_e(z) = \int_r 2\pi r n_e(r,z) u dr$.

The electron flux is equal to the total ion flux. The ion flux consists of the fluxes of argon, hydrogen and carbon ions. In figure 5.27 these three composing fluxes as resulting from the model are illustrated. After passing the shock wave the argon ion flux decreases because of recombination, but also because of charge exchange with carbon and hydrogen ions. Therefore the carbon ion flux slightly increases until all argon ions have been eliminated. Then three-particle recombination starts eliminating carbon ions. When the background pressure is lowered this does not occur. Then the carbon ion density remains constant (see figure 5.28). If the recombination of carbon ions is not wanted it can be eliminated by creating an auxiliary discharge (e.g. RF) at the location of the sample support.

The second electron carries the ionization energy after three-particle recombination. This energy is dissipated in elastic collisions with other electrons. Therefore the electron temperature remains higher than the gas temperature. Figure 5.29 shows the calculated axial profiles of electron- and gas temperature. The measured values of the gas temperature (cf. figure 5.23) are also included.

The temperatures decrease strongly in the supersonic part of the expansion. The shock front converts axial translational energy into temperature. Then the temperature decreases because of heat interaction with the surroundings.

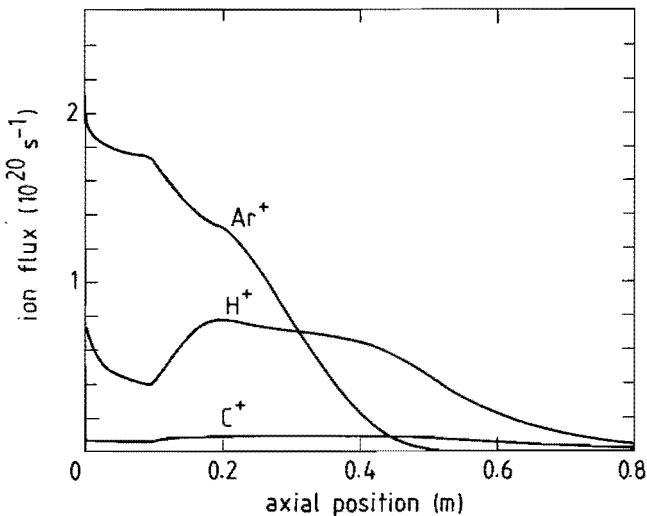


Fig. 5.27. The axial profiles of the fluxes of argon, hydrogen and carbon ions.

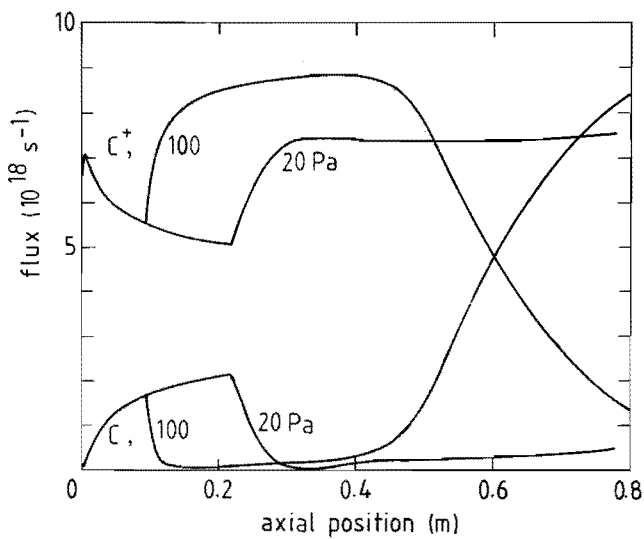


Fig. 5.28. The axial profiles of the fluxes of carbon atoms and of carbon ions. Parameter is the background pressure (20 and 100 Pa).

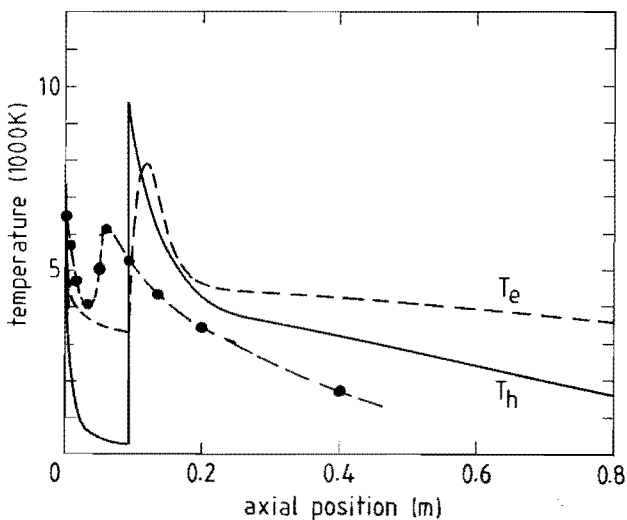


Fig. 5.29. Axial centerline profiles of the various temperatures in the plasma expansion. The emphasized dashed curve with the points represents the measurements of the gas temperature T_h using Doppler broadening. The solid and dashed curves correspond to calculated profiles of gas- and electron temperature respectively.

The experimental values appear to be higher than the calculated ones. Again this is probably caused by defects in the model. In the supersonic part additional heating by viscosity, convective currents and absorption of radiation emitted in the arc and in the subsonic relaxation zone might diminish the temperature drop due to expansion.

The calculated profiles for the electron- and gas temperature agree qualitatively with profiles calculated by Bowen and Park [BOW-71], Chou and Talbot [CHO-67], Goldfinch [GOL-71] and Zakrewskii and coworkers [ZAK-82]. Fraser, Robben and Talbot [FRA-71] used an electron beam to excite an argon-ion line in a supersonically expanding low-density RF-plasma torch and analyzed the decay of the transition with a Fabry-Pérot interferometer. They determined the electron temperature with probe measurements. Their axial profiles for electron temperature, gas temperature and gas velocity are very similar to the ones presented in this work.

Figure 5.30 compares the boundary of the plasma as assumed by the models with the dimension of the radiating part of the plasma as measured with a cathetometer. The agreement is fairly good. The experimentally determined beam shapes are similar to the profiles calculated by Love [LOV-59] for jets exhausting into still air, although the pressures are not in the same range.

Finally, figure 5.31 illustrates the calculated axial profile of the total gas pressure. In the supersonic expansion the pressure drops drastically. Across the shock wave the pressure increases strongly (cf. fig. 5.15 in Owczarek's book [OWC-64]). Then the background pressure is gradually approached.

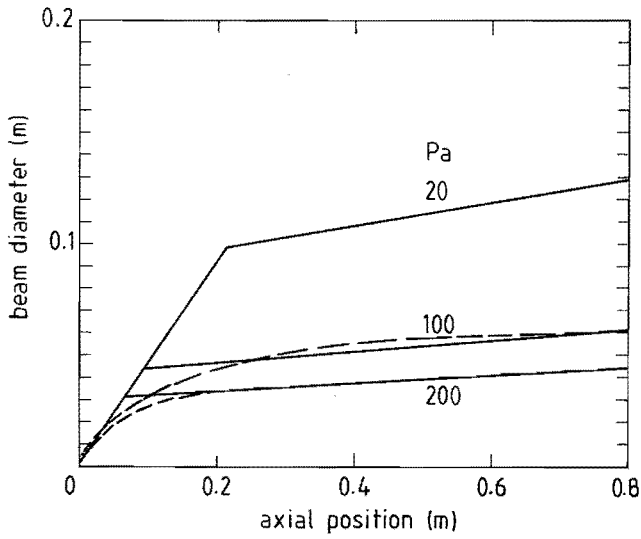


Fig. 5.30. The calculated shape of the plasma beam (full curve) and the experimentally determined profile (dashed curve). The experimental profiles are obtained using a cathetometer to determine the boundaries of the radiating part of the beam. Parameter is the background pressure.

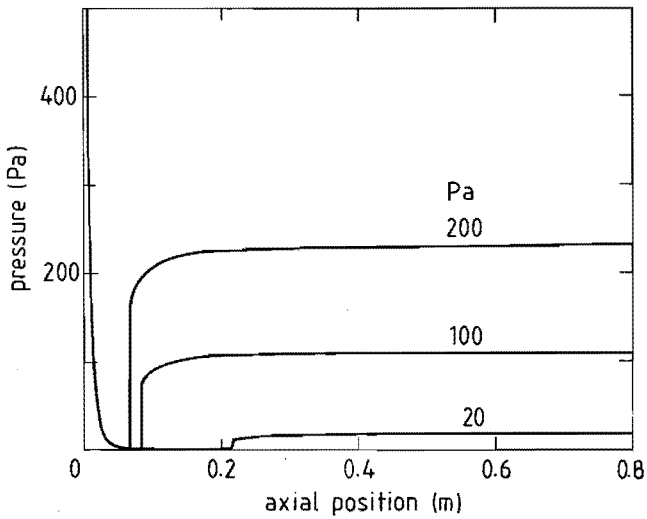


Fig. 5.31. Axial profile of the plasma pressure. Parameter is the background pressure.

5.4 In situ ellipsometry

The deposition rate and the refractive index of the produced film have been measured with *in situ* ellipsometry. As an illustration figure 5.32 shows two measured Ψ - Δ curves together with their simulations. The two curves correspond to the deposition of an amorphous carbon film on the standard substrate used for ellipsometry, a gold coated piece of Corning glass. The distinctly different appearance of the two curves illustrates that the optical properties of the films can cover a wide range. The Δ -variation of the curves is determined by the refractive index of the growing film: the larger the Δ -variation the higher the refractive index. The degree of spiralization is strongly linked to the absorption coefficient. The good agreement between measurements and simulation indicates that no secondary effects occur, like formation of a rough top layer, changes in the refractive index during growth, etc. The accuracy and stability of the instrument is demonstrated by the small scatter of the experimental points. The regions around $\Delta=180^\circ$ are very sensitive to offsets and noise in the ellipsometer signal: 1% offset can in this range cause an error in Δ of 5 degrees. A closer examination of the figures 5.32 learns that also around $\Delta=180^\circ$ the instrument is reliable. With an averaging of 2 measurements a sample rate of 50 Hz is obtained. Each 20 ms a Ψ - Δ pair can be recorded. In that case the noise in Ψ values around 0.005 degree, in Δ around 0.03 degree. When 10 measurements are averaged the noise in Δ is reduced to less than 0.01 degree. This corresponds to a thickness resolution of 0.01 nm at a sample frequency of 10 Hz. By fitting the simulated profiles to the measured points the refractive index can be determined with an accuracy of less than 1 %. This implies that also the deposition rate has an accuracy of about 1%.

The absolute accuracy of the ellipsometer has been checked with a magnetic film thickness meter [WER-87]. The results of the two instruments agree within ca. 1%, which is the accuracy of the magnetic system.

At the acquisition of each experimental point also the time is stored. This information is needed when the film thickness has to be calculated as a function of time (see figure 5.33). It appears that the deposition rate is not constant in time. It gradually decreases because of heating of the surface of the (in this case glass) substrate. Warner [WAR-85] also observed a decreasing deposition rate with increasing surface temperature. When thermally conducting substrates are used, this decrease is not observed [KER-87].

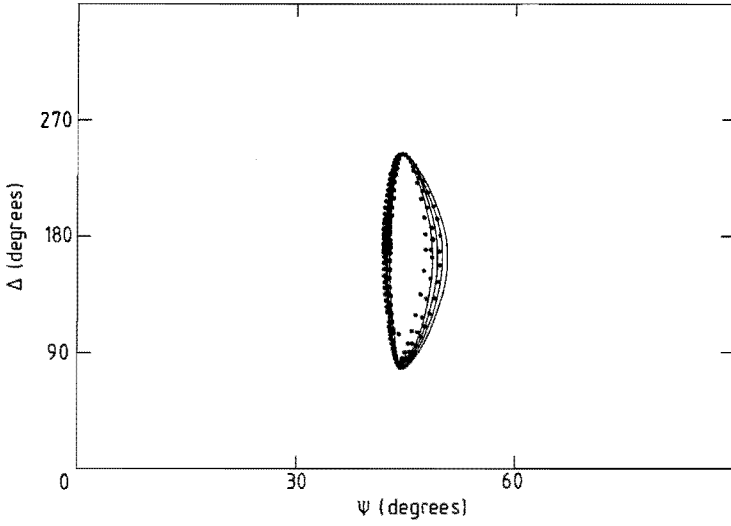
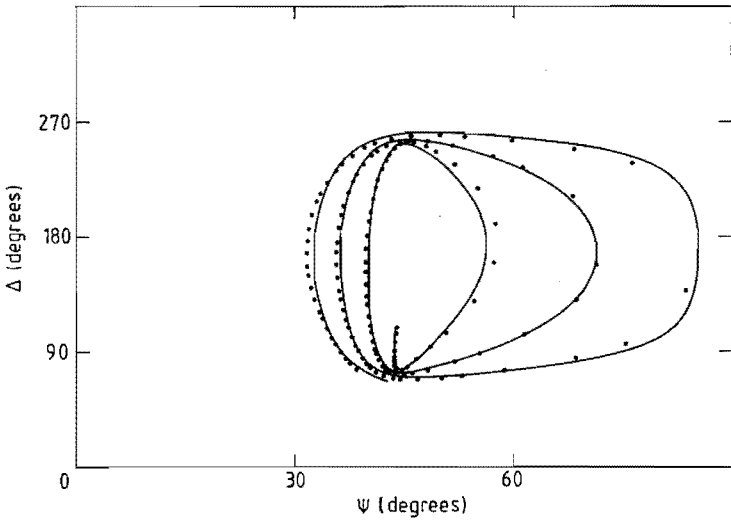


Fig. 5.32. Two examples of ψ - Δ curves as measured with the *in-situ* He-Ne ellipsometer (points) during the deposition (from an argon-methane mixture) of amorphous carbon films on gold. The full curves correspond to a simulation using the algorithm described in section 4.3.1.



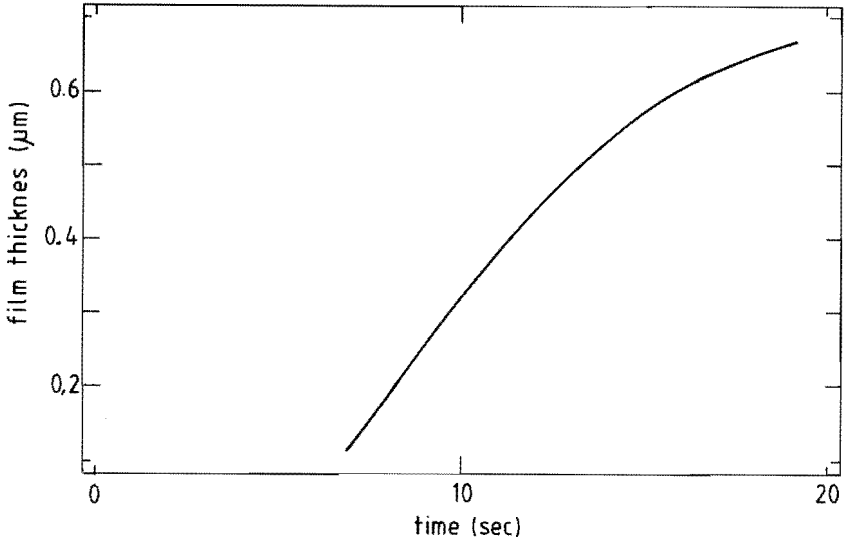


Fig. 5.33. Film thickness as a function of time.

Figure 5.34 presents the experimentally determined deposition rate as a function of carbon flux. Also included are the rates according to the model of section 2.5. Figure 5.35 does the same as a function of background pressure. For a large range of carbon fluxes and gas pressures the deposition rate is proportional to both the pressure and the carbon flux. In the model calculations the incorporation probability for carbon atoms and ions is taken 1; for CH_x radicals it is assumed 0. The agreement between model and measurements is fairly good. For very small carbon fractions no deposition occurs at all. This is probably caused by etching by atomic hydrogen [ENK-87]. A similar threshold behaviour is also observed by Nir [NIR-86]. He attributes it to removal of already deposited carbon atoms by impinging argon ions.

The refractive index is mainly determined by the total amount of energy available to each incorporated carbon atom. To illustrate this all measurements are accumulated in figure 5.36, where the refractive index is plotted versus the energy coefficient Q , which equals the ratio of the carbon flux and the power product P . The power product P is a measure for the total energy flow. It is defined as the product of argon flow and arc power. The refractive index hardly depends on the background pressure. The range of the refractive indices is very common to amorphous carbon films [ANG-87, DIS-83, WAG-86]. The energy coefficient Q can be interpreted as a measure for the reciprocal value of the energy available to every

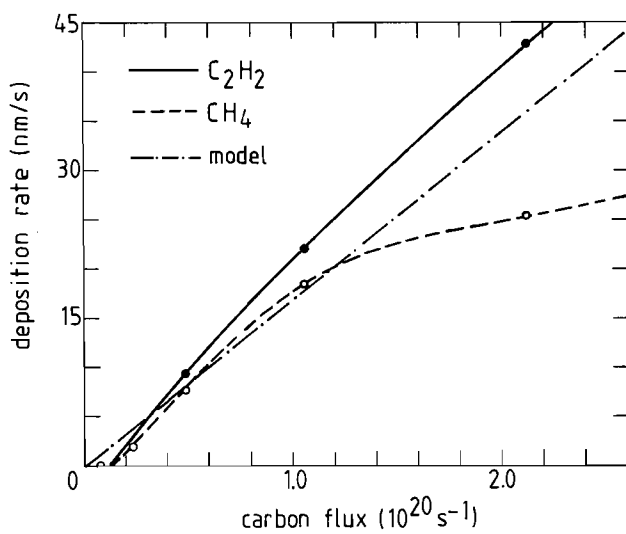


Fig. 5.34. The deposition rate as a function of the injected number of carbon atoms for an argon plasma with an admixture of methane (CH_4) or acetylene (C_2H_2). The dash-dotted curve represents the calculated values.

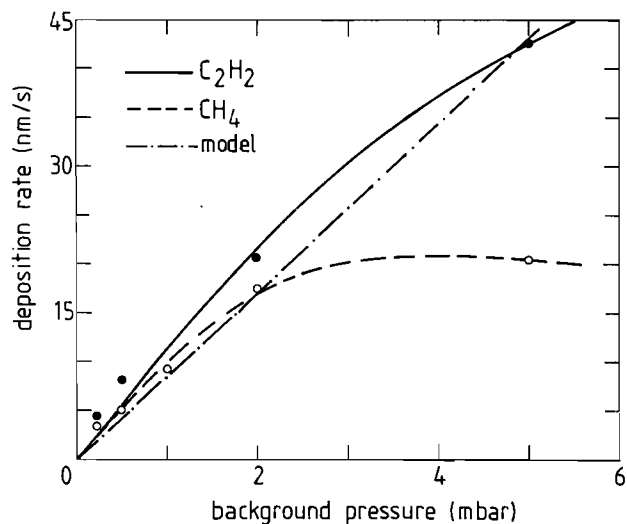


Fig. 5.35. The deposition rate as a function of background pressure.

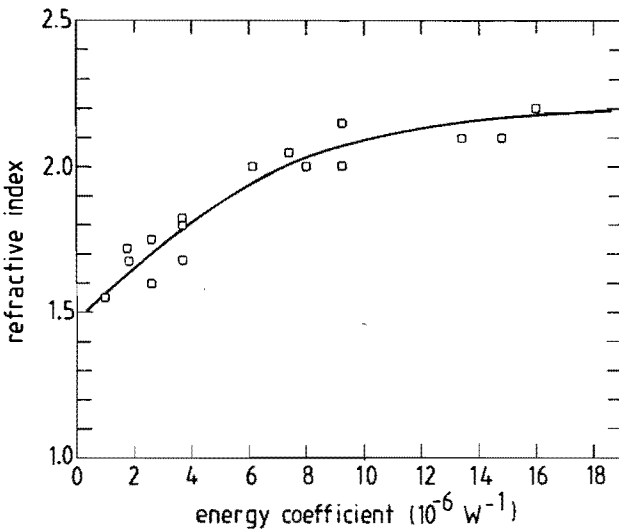


Fig. 5.36. All measurements using the *in-situ* ellipsometer accumulated in a plot of the refractive index versus the energy coefficient Q , defined as the ratio of the carbon flux and the power product P (argon flux in scc/s times arc power in W).

incorporated carbon atom. The refractive index increases with increasing Q . This implies that the energy per carbon atom has to be decreased to obtain a higher refractive index. This is in contradiction with observations by Alterovitz and coworkers [ALT-86], who found an increase in the refractive index with increasing deposition power. They used a 30 kHz HF plasma in methane to grow films on the grounded electrode. Bubenzer et al. [BUB-83] found a similar result for a plasma in benzene vapour. On the other hand Savvides [SAV-86, SAV-85] found a decreasing refractive index if the carbon ion energy or the argon/carbon ratio is increased in a graphite sputtering process. In the latter case deposition takes place with carbon atoms and ions (no hydrocarbon radicals are present) in the presence of low-energy argon ion bombardment (10–20 eV). Therefore the behaviour of the refractive index could be a confirmation that in our case the deposition is also mainly determined by the fluxes and energies of carbon atoms or ions and argon ions rather than hydrocarbon radicals.

Figure 5.37 shows the ratio of deposition rate and carbon flow divided by the background pressure as a function of the power product P , i.e. the product of arc

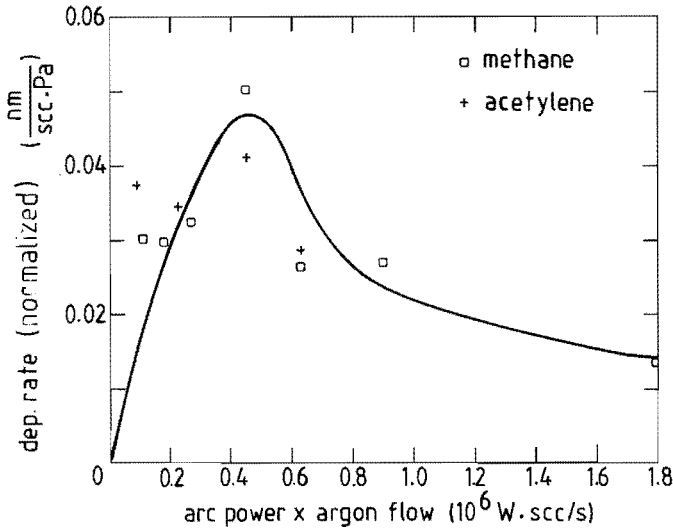


Fig. 5.37. The normalized deposition rate, defined by the deposition rate divided by the product of carbon flow (in scc/s) and background pressure (in Pa), plotted against the power product (the product of arc power in W and argon flow in scc/s). Some points represent accumulated measurements at several values of the background pressure and of the carbon flux.

power and argon flow. For small values of this power product the deposition rate increases with the power product because the dissociation degree of the injected methane increases. When a critical value is exceeded the deposition rate decreases because the surface temperature of the substrate increases [WAR-85].

By increasing arc current, argon flow and carbon flow at the same time deposition rates up to 200 nm/s have been obtained. Also at these extremely high rates the growth appears to be constant and regular. The corresponding Ψ - Δ plots do not deviate from the general shape illustrated in figure 5.32.

5.5 Film quality

The spectroscopic ellipsometer described in section 3.4 and 4.3 has been used to study the optical parameters of the film in the wavelength region 200–700 nm. Figure 5.38 shows examples of plots of the refractive index and the absorption

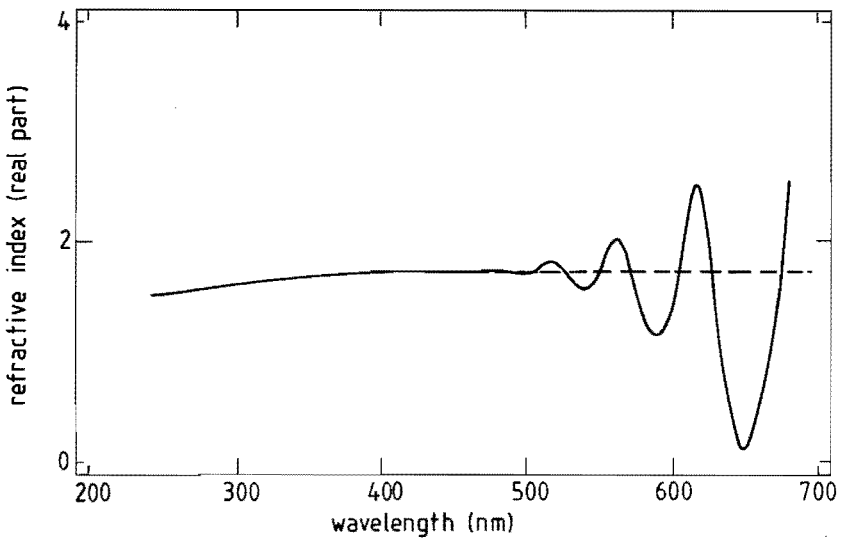
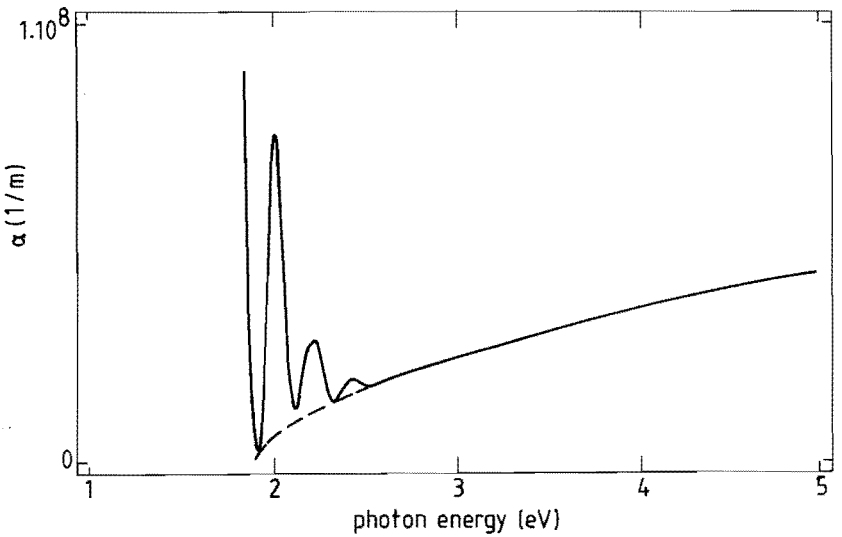


Fig. 5.38. An example of the simulated (dashed curves) and measured (full curves) spectra of the refractive index. The spectra are recorded using the spectroscopic ellipsometer. (a) presents the real part of the refractive index as a function of wavelength. In (b) the absorption coefficient α as determined from the imaginary and real parts of the refractive index is shown as a function of photon energy. In the simulation the interference is eliminated.



coefficient as a function of wavelength and photon energy respectively. The figures include the curves 'as measured' as well as interpreted using polynomial approximations for the real and imaginary parts of the refractive index. The algorithm of section 4.3 is used to convert the spectrum of the complex refractive index into "as measured" spectra. The measured curves show interference in the film, which has been corrected for by the simulation program. The absorption coefficient appears to obey the Tauc-relation [TAU-66]

$$\sqrt{\alpha E} = G(E - E_0), \tag{5.3}$$

where E represents the photon energy, G is a constant, E_0 the optical gap, and α the absorption coefficient. This relation also holds for the absorption edge of amorphous silicon [COD-81] and other amorphous materials. Figure 5.39 shows the value of the Tauc-parameter $\sqrt{(\alpha E)}$ as a function of the photon energy. The curve is approximately linear. The intersection with the E -axis indicates the bandgap. The optical bandgap is, like the refractive index, a function of the energy coefficient Q , defined in the previous section. Figure 5.40 displays the optical gap as a function of the energy coefficient Q . The bandgap appears to widen when the power product P

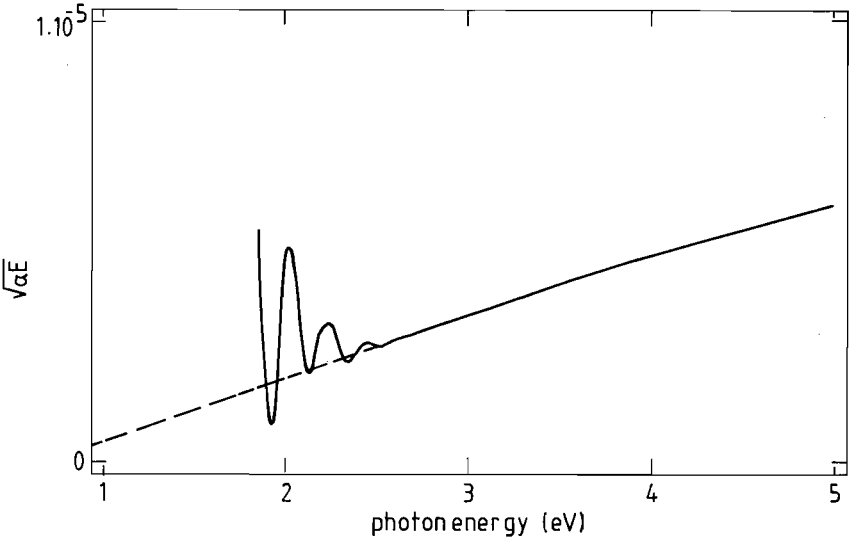


Fig. 5.39. The Tauc parameter ($= \sqrt{\alpha E}$) as a function of photon energy. The section with the horizontal axis corresponds to the optical bandgap.

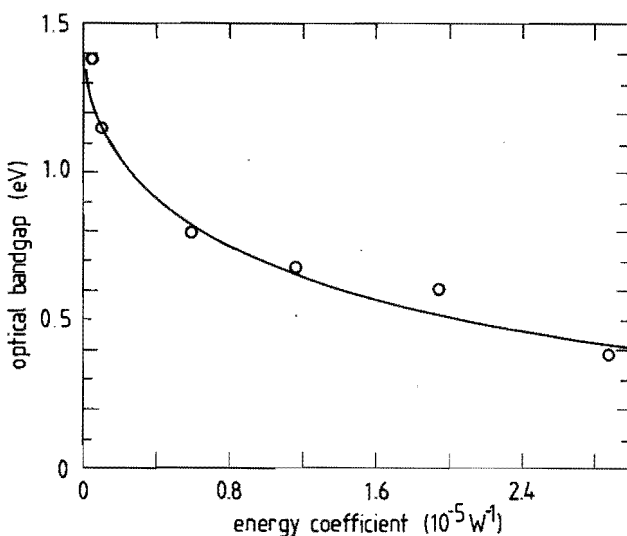


Fig. 5.40. The optical bandgap as determined with the spectroscopic ellipsometer as a function of the energy coefficient Q .

per injected carbon atom ($=1/Q$) is increased. The bandgaps and the values of the gradient coefficient G agree with measurements of Bubbenzer [BUB-83], Dischler [DIS-83], Jansen [JAN-85] and Ishikawa [ISH-87]. In all cases the gradient G appears to be approximately constant. Dischler for instance reports $G = 7.0 \cdot 10^{22} \text{ m}^{-\frac{1}{2}} \text{ J}^{-\frac{1}{2}} (=280 \text{ cm}^{-\frac{1}{2}} \text{ eV}^{-\frac{1}{2}})$, whereas our films yield $G = 6.9 \cdot 10^{22} \text{ m}^{-\frac{1}{2}} \text{ J}^{-\frac{1}{2}} (=277 \text{ cm}^{-\frac{1}{2}} \text{ eV}^{-\frac{1}{2}})$. Angus, Koidl and Mirtich have accumulated the Tauc plots of a large number of authors [ANG-86]. Also they find in almost all cases the same gradient G . The bandgap of the films produced by Savvides [SAV-86] using graphite sputtering also values around 1 eV. Alterovitz [ALT-86] and Natarajan [NAT-85] attained slightly higher bandgaps (around 2 eV). Their absorption coefficients are in the same range. Memming [MEM-86] also reports bandgaps around 2 eV, but his absorption coefficients are substantially (a factor 10) higher than the average. Almost all authors observe that a high refractive index is associated with a low optical bandgap [e.g. ALT-86, BUB-83 and SAV-85]. Films with a small bandgap ($<1\text{eV}$) and a high refractive index (>2.0) are often called "diamond-like" and films with a large bandgap and a low refractive index are usually called "polymer-like". Comparison of the figures 5.36 and 5.40 learns that

this trend is also observed in our films. For small values of Q the films are polymer-like, for large values of Q they are diamond-like. We might conclude that the optical parameters of the produced films in the photon energy range 1–5 eV correspond to the values reported in the literature, in absolute value as well as in the intercorrelation between the various film parameters.

Elastic scattering of α -particles was used to perform a depth analysis of the carbon, hydrogen and oxygen concentrations [KLE-87]. Figure 5.41 compares the depth profile of oxygen of a deposited carbon film and a sheet of Mylar. The channel number is a measure for the energy of the detected α 's, which is in its turn a measure for the distance of the scatterer to the film surface. The amount of oxygen incorporated in the film appears not to be detectable (<1%). The carbon depth profile (see figure 5.42) shows that the number density of carbon atoms in the film is larger than in the case of Mylar. The hydrogen content of the polymer-like films can be as high as 60 atomic percent, independent of the relative hydrogen content of the original gas. The more diamond-like films contain about 40 at. % hydrogen. Values in this range have also been reported in the literature [e.g. ANG-86, WEI-85, KAP-85, DIS-83]. Nir has succeeded in reducing the hydrogen content to 10 % by adding CO to the gas mixture.

The contamination level of the films with metals like copper, tungsten and thorium (present in the arc walls and electrodes of the arc and touching the plasma) has been investigated with X-ray photoelectron spectroscopy (XPS) and secondary ion mass spectroscopy (SIMS). No contamination has been found, which means that the concentration is below the detection limit of the diagnostics (for SIMS about 1 ppm). The contamination caused by the observed cathode wear can be estimated to amount to a maximum of about 1 ppb.

The diamond-like films are not soluble in any organic solvent. They are not attacked by inorganic acids, including HF. The polymer-like films may be soluble in concentrated H₂SO₄. Both qualities of the films can be etched in a dense oxygen/argon discharge.

The films adhere well on steel substrates after proper cleaning using a 3 kV sputtering discharge. The adhesion on the standard ellipsometry substrate (a gold coated piece of Corning glass) is bad, as is to be expected. When the thickness exceeds 1 micron most of the (harder) films peel off spontaneously while being fragmented into pieces of about 1 mm² that are "launched" at high velocities. The spontaneous peeling of the film is one of the manifestations of the usually large internal compressive stress [ENK-85, PRI-85].

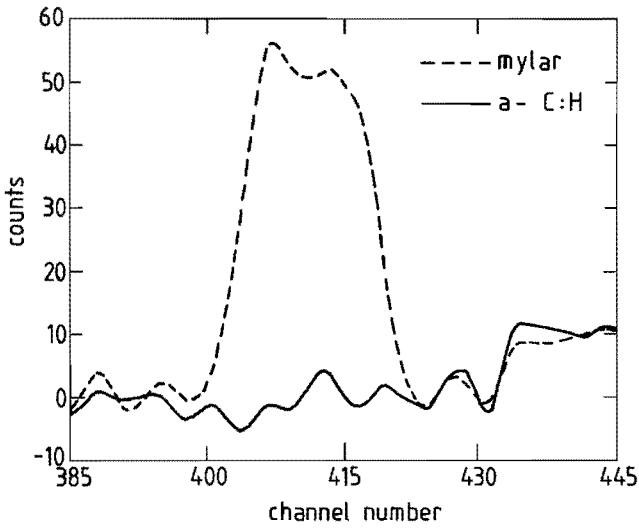


Fig. 5.41. The number of detected recoils of α -particles scattered elastically at oxygen atoms as a function of the channel number in the multi-channel analyzer. This graph can be interpreted as a depth profile of the oxygen concentration in the film. The dashed curve corresponds to a reference sample (2 microns of Mylar). The full curve represents an amorphous carbon film. No oxygen contamination can be detected.

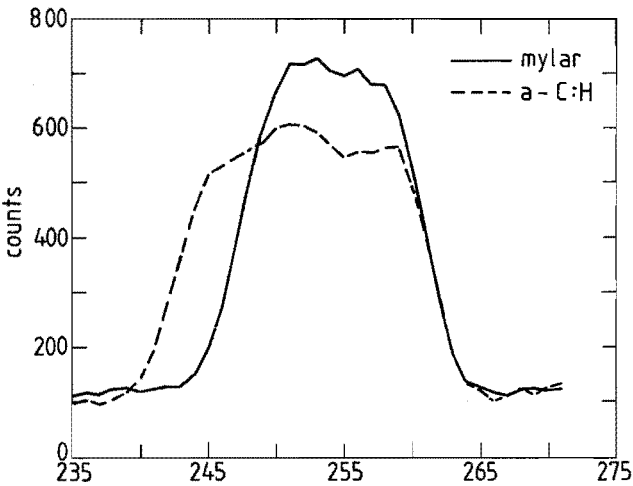


Fig. 5.42. Carbon depth profile. See fig. 5.41 for an explanation.

Some preliminary results of scratch tests using sharpened pieces of minerals with increasing hardness learn that the films can be very hard: corresponding to 6-→20 GPa Vickers hardness (10 GPa = 1000 kgf/mm²). This has been confirmed by measurements using an extrapolation of Vickers measurements with decreasing load towards zero load [LIE-87], a method also used by Whitmell and Williamson [WHI-76]. With this method an estimation of 40 GPa was found for the hardest films. Although the hardness values measured with the scratch tests are very inaccurate, one can still observe that the hardness, like the bandgap and the refractive index, depends on the energy coefficient Q . Figure 5.43 shows the hardnesses of some films plotted against the energy coefficient Q . The diamond-like films appear to be the hardest ones, whereas the polymer-like films are very soft. The hardness range is very common to a-C:H films [ANG-86]. Weissmantel [WEI-85] has also reported hardnesses of about 20 GPa, but he was able to increase it to 40 GPa by applying a bias voltage of 1 kV. Enke [ENK-85, ENK-81] reported hardnesses in the range of 20-50 GPa. Pethica and coworkers [PET-85] used micromechanical methods to analyse the hardness of films produced in a DC glow discharge. They obtain values from 5-20 GPa, the highest hardness occurring at the highest bias voltages (up to 1500 V). Koskinen et al. [KOS-85] claim to have achieved a hardness of 180 GPa (diamond: 100) using ion beam deposition.

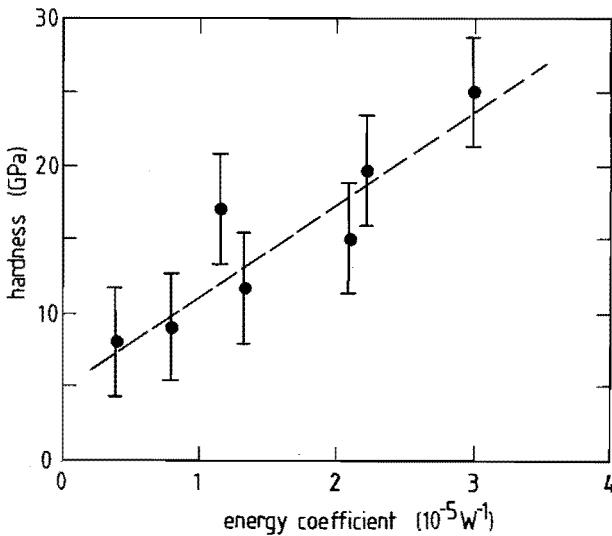


Fig. 5.43. Hardness of the deposited films as a function of the energy coefficient Q . The experimental values are obtained with scratch tests.

6 CONCLUSIONS

A: General

- The subject of this work is a new method for plasma deposition. The essential concept of this method is the spatial separation of plasma production by a cascaded arc on one hand and the actual deposition process on the other hand. Extremely high deposition rates (up to 200 nm/s) have been obtained while the film quality is similar to the one obtained with conventional RF-discharges.

B: Dynamics of the arc plasma

- The energy needed to operate the cascaded arc is used efficiently. At the beginning of the channel about 60 % of the local Ohmic input energy is used to heat the argon gas, and the other 40 % is used to ionize the argon atoms. As the Ohmic input is almost independent of the gas flow the number of created electrons depends only weakly on the gas flow. For temperature equilibration about 20 mm of arc length are needed. The heating of the gas and the creation of the argon ions both use about 10 % of the total arc power.
- The description according to De Haas of a flowing cascaded arc plasma with the three transport equations, where the wall friction is taken into account by a friction factor that only depends on the wall shape and the Reynolds number, adequately explains the pressure drop over the channel. There are indications that the flow in the arc channel is laminar.
- The overpopulation of the argon neutral ground level in the arc channel never becomes smaller than 10. This means that the plasma is strongly ionizing.
- The arc length needed for full dissociation and ionization of the injected material (methane) is about 30 mm. By changing the injection location the degree of dissociation and ionization can be tuned.
- Carbon atoms are ionized mainly by resonant charge transfer from argon to carbon. The contribution of direct ionization by electron impact is negligibly

small as long as the amount of admixed carbon atoms remains smaller than the argon ion flux. In that case 5 % of the arc power is used to heat and dissociate the methane, and another 10 % is needed to ionize the methane fragments.

C: Dynamics of the plasma beam

- The measurements of gas velocity, gas temperature and electron density clearly indicate that the plasma of the cascaded arc expands supersonically into the vacuum system. The velocity increases from 1700 m/s to over 4000 m/s, whereas the temperature and the electron density decrease.
- The supersonic expansion is limited by a shock wave. Here the directed motion of the particles present in the plasma is randomized; kinetic energy is partially converted to thermal energy.
- Doppler shift of a spectral line provides an accurate means of determining the plasma velocity. With the present setup a detection limit of 50 m/s has been obtained. The relative accuracy is about 5 %.
- Errors in the afore described velocity measurements might be introduced by integration over the detection volume. The spatial resolution could be increased if this technique would be combined with optical pumping of the used transition with a pulsed dye-laser.
- The measured spatial profiles of gas velocity, gas temperature and electron density clearly indicate that the plasma does not expand isotropically: an intense beam with a diameter of ca. 10 cm is formed.
- Modeling of the plasma using a quasi one-dimensional approach yields results that agree well with the measurements. The existing discrepancies are mainly due to the omission of the viscosity in the calculations and to neglecting convective currents and capture of radiation. The essential three-dimensional nature of the expansion is also expected to cause some discrepancies.
- The chemical equilibrium of the arc plasma is almost frozen in the supersonic expansion. The relative densities of the various fragments of methane hardly

change during the flight of the plasma from the arc exit to the substrate. Carbon ions however can be neutralized by three particle recombination. This does not occur for low values of the gas pressure (e.g. 20 Pa).

D: Deposition

- *In situ* ellipsometry provides for accurate determination of the deposition rate and the complex refractive index of the growing film as a function of time. The present setup offers an accuracy of about 0.01 degree in the ellipsometric angles Ψ and Δ . This corresponds to a thickness resolution of 0.01 nm. The refractive index can be determined within 1 %.
- The growth is adequately described by a single-layer model. No evidence has been found for the occurrence of top- or intermediate layers.
- When acetylene is used the deposition rate is proportional to the admixed carbon flux and to the background pressure in the vacuum system. In the case of methane saturation of the deposition rate occurs for large values of carbon flux and pressure.
- On thermally isolating substrates the deposition rate decreases as a function of time because of heating of the substrate surface.
- The refractive index of the film is determined by the amount of energy per carbon atom supplied by the plasma. High energies yield low refractive indices and vice versa. This is in contradiction with the observations reported in the literature for conventional deposition processes using RF plasmas.
- A cascaded arc is well suited to be used as a light source for spectroscopic ellipsometry. The intensity in the UV region of the spectrum is high and the light is totally unpolarized.
- The optical absorption coefficient as a function of photon energy (as analyzed with the spectroscopic ellipsometer) follows the Tauc-relation. The bandgap of the deposited material varies between 0.5 and 1.5 eV.

- The intercorrelation of the measured film parameters (refractive index, optical bandgap and hardness) agrees with the trends reported by others in the literature.
- The deposited films are characterized by a low contamination level, a relatively high hydrogen content and large compressive stresses. They are chemically inert.

REFERENCES

- ALT-86 S.A. Alterovitz, J.D. Warner, D.C. Liu and J.J. Pouch, J. Electrochem. Soc. 133(1986)2339.
- ANG-86 J.C. Angus, P. Koidl and S. Domitz, "Carbon thin films" in "Plasma deposited thin films", J. Mort and F. Jansen, editors, CRC press Inc, Boca Raton, USA (1986).
- ASP-75 D.E. Aspnes and A.A. Studna, Appl. Opt. 14(1975)220.
- AZZ-77 R.M.A. Azzam and N.M. Bashara, "Ellipsometry and polarized light", North Holland, Amsterdam, the Netherlands (1977).
- BAU-76 U.H. Bauder, Appl. Phys. 9(1976)105.
- BEN-70 S.W. Benson and H.E. O'Neal, "Kinetic data on gas phase unimolecular reactions", National standard reference data series, National Bureau of Standards, Washington DC, USA (1970).
- BEN-83 R.P. Benedict, "Fundamentals of gas dynamics", Wiley, New York, USA (1983).
- BOR-86 H. Borning, Plasma News Report, Carlsbad, CA, USA, sept. 1986.
- BOW-71 S.W. Bowen and C. Park, AIAA-Journal 9(71)493.
- BRA-65 S.I. Braginskii, in "Reviews of plasma physics", Ed. M.A. Leontovich, Consultants Bureau, New York, USA (1965).
- BUB-83 A. Bubenzer, B. Dischler, G. Brandt and P. Koidl, J. Appl. Phys. 54(83)4590.
- COD-81 G.D. Cody, T. Tiedje, B. Abeles, B. Brooks and Y. Goldstein, Phys. Rev. Lett. 47(1981)1480.
- CAT-81 Y. Catherine, Ph. D. Thesis, Université de Nantes, Nantes, France (1981).
- CHO-67 Y.S. Chou and L. Talbot, AIAA-Journal 5(1967)2166.
- DIS-83 B. Dischler, A. Bubenzer and P. Koidl, Appl. Phys. Lett. 42(1983)636.
- DON-85 T.J. Donahue and R. Reif, J. Appl. Phys. 57(1985)2757.
- EBI-85 K. Ebihara and S. Maeda, J. Appl. Phys. 57(1985)2482.

- EDD-75 T.L. Eddy, C.J. Cremers and H.S. Hsia, JQSRT 17(1975)287.
- EDD-87 A. Sedginasab and T.L. Eddy, Proceedings ICPIG XVIII, Swansea, U.K. (1987)724.
- ENK-81 K. Enke, Thin Solid Films 80(1981)227.
- ENK-85 K. Enke, Applied Optics 24(1985)508.
- ENK-87 K. Enke, Proceedings E-MRS 1987 meeting, symposium C, Stasbourg, France (1987), to be published.
- FRA-71 R.B. Frazer, F. Robben and L. Talbot, Phys. Fluids 14(1971)2317.
- FRO-61 L.S. Frost, J. Appl. Phys. 32(1961)2029.
- GLE-87 A. Gleizes, I. Sakalis, M. Razafinimanana and S. Vacquie, J. Appl. Phys. 61(1987)510.
- GOL-68 V.M. Goldfarb, E.V. Ilyina, I.E. Kostigova and G.A. Lukyonov, AIAA-paper No. 68-682 (1968).
- GOL-71 J. Goldfinch, J. Plasma Phys. 6(1971)153.
- GRI-64 H.R. Griem, "Plasma Spectroscopy", MacGraw-Hill, New York, USA (1964).
- GRI-74 H.R. Griem, "Spectral line broadening by plasmas", Academic press, New York, USA (1974).
- HAA-86 J.C.M. de Haas, Ph. D. Thesis, University of Technology, Eindhoven, the Netherlands (1986).
- HAA-87 J.C.M. de Haas, University of Technology, Eindhoven, the Netherlands, private communication (1987).
- HAS-72 J.B. Hasted, "Physics of atomic collisions", Butterworth & Co., London, U.K. (1972).
- HEC-74 E. Hecht and A. Zajac, "Optics", Adisson-Wesley publ. comp.Inc., Reading, USA (1974).
- HOL-79 L. Holland, SPIE 197(1979)319.
- HSU-82 K-C. Hsu, Ph. D. Thesis, University of Minnesota, Minneapolis, USA (1982).
- IGR-75 O. Igra, Prog. Aerospace Sc. 16(1975)299.

- ISH-87 J. Ishikawa, Y. Takeiri, K. Ogawa and T. Takagi,
J. Appl. Phys. 61(1987)2509.
- JAN-85 F. Jansen, M. Machonkin, S. Kaplan and S. Hark,
J. Vac. Sci. Technol. **A3**(1985)605.
- JEN-71 R.C. Jenkins, AIAA-Journal **9**(1971)1383.
- KIE-84 J. Kieser and M. Neusch, Thin Solid Films **118**(1984)203.
- KAF-79 H. Kafrouni, J.M. Bagneaux, A. Gleizes and S. Vacquie,
JQSRT **21**(1979)457.
- KAP-85 S. Kaplan, F. Jansen and M. Machonkin,
Appl. Phys. Lett. **47**(1985)750.
- KER-87 H. Kersten, Internal report VDF/NT 87-25, University of Technology,
Dept. of Physics, Eindhoven, the Netherlands (1987).
- KLE-87 S.S. Klein and G.M.W. Kroesen, to be published.
- KON-72 V.N. Kondratiev, "Rate constants of gas phase reactions", National
standard reference data series, National Bureau of Standards,
Washington DC, USA (1972).
- KOS-85 J. Koskinen, J-P. Hirvonen and A. Anttila,
Appl. Phys. Lett. **47**(1985)941.
- KRA-73 M. Kraus and P.S. Julienne, Astrophys. J. **183**(1973)1139.
- KRO-81 G.M.W. Kroesen, Internal report VDF/NT 81-06, University of
Technology, Dept. of Physics, Eindhoven, the Netherlands (1981).
- KRO-83 G.M.W. Kroesen, Internal report VDF/NT 83-07, University of
Technology, Dept. of Physics, Eindhoven, the Netherlands (1983).
- LIE-87 W.A.M. Liebregts, Internal report VDF/NT 87-06, University of
Technology, Dept. of Physics, Eindhoven, the Netherlands (1987).
- LUN-86 A. Lunk and M. Schmidt, Proc. ESCAMPIG VIII, Greifswald,
DDR, (1986)37.
- LOV-59 E.S. Love, C.E. Grigsby, L.P. Lee and M.J. Woodling, "Experimental
and theoretical studies of axisymmetric freejets", TR-R-6 (1959)
NASA.

- MAE-56 H. Maecker, Z. Naturforsch. 11a(1956)457.
- MAI-75 H.N. Maier and R.W. Fessenden, J. Chem. Phys. 62(1975)4790.
- MAT-85 S. Matsumura, K. Sakurai, A.A. Berezin, R.M. Hobson, S. Teii and J-S. Chang, Can. J. Phys. 63(1985)826.
- MAT-84 T. Matsushita, K. Komori, M. Konagai and K. Takahashi, Appl. Phys. Lett. 44(1984)1092.
- MEM-86 R. Memming, Thin Solid Films 143(1986)279.
- MIT-73 M. Mitchner and C.J. Kruger Jr., "Partially ionized gases", Wiley, New York USA (1973).
- NAT-85 V. Natarajan, J.D. Lamb, J.A. Woollam, D.C. Liu and D.A. Gulino, J. Vac. Sci. Technol. A3(1985)681.
- NIR-86 D.Nir and M. Mirtich, J. Vac. Sci. Technol. A4(1986)560.
- OWC-64 J.A. Owczarek, "Fundamentals of gas dynamics", International Textbook Company, Scranton USA (1964).
- PER-83 J. Perrin, Ph. D. thesis, Université Paris VII, Paris, France (1983).
- PER-84 J. Perrin, B. Drevillon, École Polytechnique, Palaiseau, France, private communication (1985).
- POI-85 G. Poissant and M. Dudeck, J. Appl. Phys. 58(1985)1772.
- PET-85 J.B. Pethica, P. Koidl, J. Gobrecht and C. Schüler, J. Vac. Sci. Technol. A3(1985)2391.
- PRI-62 W.C. Price, P.V. Harris and T.R. Passmore, JQSRT 2(1962)327.
- PRI-85 E.T. Prince and M.M. Romach, J. Vac. Sci. Technol. A3(1985)694.
- RUT-86 P. Rutérana, P. Friedel, J. Schneider and J.P. Chevalier, Appl. Phys. Lett. 49(1986)672.
- SAA-85 M.A. Saad, "Compressible fluid flow", Prentice-Hall, Englewood Cliffs USA (1985).
- SAV-85 N. Savvides and B. Window, J. Vac. Sci. Technol. A3(1985)2386.
- SAV-86 N. Savvides, J. Appl. Phys. 59(1986)4133.
- SHI-84 M. Shindo, S. Sato, I. Myokan, S. Mano and T. Shibata, Jap. J. Appl. Phys. 23(1984)273.

- SOK-81 M. Sokolowski, A. Sokolowski, A. Michalski, Z. Romanowski, A. Rusek-Masurek and M. Wronikowski, *Thin Solid Films* **80**(1981)249.
- SPI-56 L. Spitzer, "Physics of fully ionized gases", Interscience Publishers Inc., New York, USA (1956).
- TAU-66 J. Tauc, R. Grigorovici and A. Vancu, *Phys. Status Solidi* **15**(1966)627.
- THO-65 P.A. Thompson, *AIAA-Journal* **3**(1965)212.
- TIM-84 C.J. Timmermans, Ph. D. thesis, University of Technology, Eindhoven, the Netherlands (1984).
- TIM-85 C.J. Timmermans, R.J. Rosado and D.C. Schram, *Z. Naturforsch.* **40a**(1985)810.
- TOY-85 Y. Toyoshima, . Kumata, U. Itoh, K. Arai, N. Matsuda, N. Washida, G. Inoue and K. Katsumi, *Appl. Phys. Lett.* **46**(1985)584.
- UME-84 K. Umeda, Y. Kawashimo, M. Nakasone, S. Harada and A. Tasaki, *Jap. J. Appl. Phys.* **23**(1984)1576.
- VAC-85 S. Vacquie, A. Gleizes and H. Kafrouni, *J. Phys. D.* **18**(1985)2193.
- VAL-84 P.M. Vallinga, Internal report VDF-NT/84-02, University of Technology, Dept. of Physics, Eindhoven, the Netherlands (1984).
- VAN-84 P.E. Vanier, F.J. Kampas, R.R. Corderman and G. Rajeswaran, *J. Appl. Phys.* **56**(1984)1812.
- VAR-75 N.B. Vargaftik, "Table on the thermophysical properties of liquids and gases", Hemisphere publ. comp. (Wiley), Washington, USA (1975).
- VER-81 P.W.E. Verhelst, internal report VDF/CO 79-18B, University of Technology, Dept. of Physics, Eindhoven, the Netherlands (1981).
- WAG-86 J. Wagner and P. Lautenschlager, *J. Appl. Phys.* **59**(1986)2044.
- WAR-85 J.D. Warner, J.J. Pouch, S.A. Alterovitz, D.C. Liu and W.A. Landford, *J. Vac. Sci. Technol.* **A3**(1985)900.
- WAT-86 T. Watanabe, K. Azuma, M. Nakatani, K. Suzuki, T. Sonobe and T. Shimada, *Jap. J. Appl. Phys.* **25**(1986)1805.
- WEI-85 C. Weissmantel, *J. Vac. Sci. Technol.* **A3**(1985)2384.

- WER-87 J. Werner, A. van der Scheer, Shell laboratory KSLA, private communication (1987).
- WHI-76 D.S. Whitmell and R. Williamson, Thin Solid Films 35(1976)255.
- WIN-75 H.F. Winters, J. Chem. Phys. 63(1975)3462.
- WIT-74 P.O. Witze, AIAA-Journal 12(1974)417.
- WON-85 J. Wong, T.M. Lu and S. Mehta, J. Vac. Sci. Techn. B(1985)453.
- YAM-87 H. Yamada and Y. Torii, Appl. Phys. Lett. 50(1987)386.
- ZAK-82 N.V. Zakrewskii, G.A. Luk'yanov and S.I. Tserkovni, Sov. Phys. Techn. phys. 27(82)801.
- ZAR-86 C.B. Zarowin, N. Venkataramanan and R.R. Poole, Appl. Phys. Lett. 48(1986)759.
- ZEE-85 C.J.H. de Zeeuw, Internal report VDF-NT/85-12, University of Technology, Dept. of Physics, Eindhoven, the Netherlands (1985).

SAMENVATTING

In de afgelopen 20 jaar zijn er verschillende industriële processen ontwikkeld waarbij plasma's een belangrijke rol spelen. Deze processen worden vaak toegepast bij de bewerking van oppervlakken. Eén daarvan is plasmadepositie. Deze techniek, waarmee een dunne laag van een bepaald materiaal op een substraat wordt aangebracht, onderscheidt zich van de gebruikelijke CVD-methodes (chemical vapour deposition) doordat de dissociatie van het (meestal gasvormige) ingangsmateriaal nu niet thermisch wordt bewerkstelligd, maar verzorgd wordt door botsingen met electronen. Hiervoor wordt in verreweg de meeste gevallen een radiofrequente (RF) of continue (DC) glimontlading toegepast. Het grote nadeel van deze beide configuraties is dat één ontlading een aantal functies tegelijk moet vervullen. Zo zal zij zorg dienen te dragen voor de dissociatie en partiële ionisatie van het ingangsmateriaal, maar tevens zal zij de geproduceerde radicalen en ionen naar het substraat moeten transporteren. Bovendien moeten er aan het te bedekken oppervlak zodanige condities geschapen worden dat de aangevoerde reactieve deeltjes op een efficiënte manier in de groeiende laag ingebouwd kunnen worden. In het algemeen zal het niet mogelijk zijn om met één plasma alle drie genoemde deelprocessen zo goed mogelijk te laten verlopen.

Daarom zijn bij de reactor die in dit proefschrift wordt beschreven de drie functies (dissociatie en ionisatie, transport en depositie) ruimtelijk gescheiden en apart geoptimaliseerd. Een cascadeboog in argon wordt gebruikt als dissociatief medium. In dit plasma wordt methaan of acetyleen geïnjecteerd. De geproduceerde reactieve deeltjes worden door een supersonische expansie in vacuüm, gevolgd door een subsone plasmabundel, op een efficiënte manier naar het substraat getransporteerd. Daar wordt dan een amorfe, gehydrogeneerde koolstoflaag gedeponeerd.

Het stromende plasma in de cascadeboog is geanalyseerd door middel van diagnostieken en modellen. De electronendichtheid en de electronentemperatuur zijn als functie van de plaats in de boog gemeten met behulp van respectievelijk de Stark-verbreding van de waterstof β -lijn (486.1 nm) en de verhouding tussen lijn- en continuümmissie. Samen met de opgemeten drukprofielen zijn deze metingen gebruikt om de profielen van de gastemperatuur uit te rekenen aan de hand van een aanpassing van de resultaten van een quasi-ééndimensionaal model aan de metingen. Daarna kon de overbezettingsfactor van het grondniveau van argonatomen bepaald worden. In het begin van het boogkanaal bedraagt deze overbezetting

ruwweg een factor 40, onafhankelijk van de hoeveelheid argon gas die de boog doorstroomt. Uit energiebeschouwingen blijkt dat hier een groot deel (60%) van de gedissipeerde elektrische energie gebruikt wordt om het koude gas op te warmen. Voor de ionisatie van de argonatomen is dan nog maar ca. 40 % beschikbaar. Dit zorgt ervoor dat het totale aantal geproduceerde electronen (en dus ook de electronendichtheid) nauwelijks afhangt van de gasstroom. De booglengte moet minimaal 2 cm bedragen wil men het gas kunnen opwarmen tot zijn temperatuur gelijk is aan de electronentemperatuur (12000 K).

De drukval over het boogkanaal hangt sterk samen met het optreden van visceuse wrijving tussen boogwand en plasma. Analyses aan de hand van de behoudswetten voor massa, impuls en energie wijzen uit dat het gemeten verband tussen de zgn. wrijvingsfactor en het Reynoldsgetal de theoretische curve voor laminaire stroming in een volkomen gladde buis dicht benadert.

De dissociatie van het geïnjecteerde methaan is beschreven aan de hand van de behoudswetten voor massa en energie. De berekeningen wijzen uit dat een booglengte van ca. 2 cm ná de injectie van methaan voldoende is om volledige ionisatie en dissociatie te bereiken. De koolstofatomen worden voornamelijk geïoniseerd door resonante overdracht van de lading van argonionen.

In de supersone expansie van het boogplasma zijn de gassnelheid, de gastemperatuur en de electronendichtheid bepaald met behulp van respectievelijk Dopplerverschuiving en -verbreding van een argonspectraallijn en Stark-verbreding van de H_{β} -lijn. De stromingssnelheid neemt toe van ca 1700 m/s in de anode-uitstroomopening tot ca. 4000 m/s na 50 mm. Ondertussen vindt er een drastische daling van de temperatuur plaats (tot minder dan 2000 K). Hierdoor wordt de samenstelling van het plasma als het ware ingevroren: de verhoudingen van de dichtheden van de verschillende componenten van het plasma veranderen nauwelijks. Driedeeltjesrecombinatie van argonionen zorgt ervoor dat de electronentemperatuur hog r blijft dan de gastemperatuur. Het supersoon expanderende plasma is beschreven met wederom de behoudswetten voor massa, impuls en energie. Ook hier is de overeenstemming tussen model en experiment goed.

Na ongeveer 50 mm treedt er een schokgolf op. De energie van de sterk voorwaarts gerichte beweging wordt nu gedeeltelijk omgezet in thermische energie. De snelheid neemt af (tot 2000 m/s), en de temperatuur neemt toe (naar 6000 K). Na de schokgolf wordt er een subsone, maar toch nog met hoge snelheden (ca. 1000 m/s) stromende plasmabundel gevormd. De argonionen worden geleidelijk geneutraliseerd door ladingsoverdracht aan koolstofatomen. De zo gecreëerde kool-

stofionen recombineren daarna weer snel. Op deze manier blijft de dichtheid van koolstofionen nagenoeg constant tot de argonionen volledig geëlimineerd zijn. Daarna zakt ook de dichtheid van de koolstofionen. Dit proces kan worden vertraagd door de druk te verlagen.

De groei van de amorfe koolstoflaag is bestudeerd met *in situ* He-Ne ellipsometrie. Deze techniek, die gebruik maakt van de veranderende polariserende eigenschappen van een groeiende laag, levert naast de groeisnelheid ook waarden voor de brekingsindex en de absorptiecoëfficiënt van het materiaal. Het voor deze experimenten ontwikkelde model bezit een gevoeligheid die overeenkomt met een laagdikte van 10 pm. De lagen zijn ook onderzocht wat betreft het gedrag van hun optische parameters in een groot golflengtegebied. Hiervoor is een spectroscopische ellipsometer ontwikkeld. Tenslotte is systematisch de hardheid van de lagen geschat door middel van krasproeven.

De kwaliteit van de gedeponeerde laag wordt vooral bepaald door de hoeveelheid energie die per koolstofatoom door het plasma aan het oppervlak wordt afgegeven. Is deze energie laag, dan is de brekingsindex hoog (2.4), de optische bandafstand klein (0.5 eV) en de hardheid groot (30 GPa). De laag wordt dan "diamant-achtig" genoemd. Is deze energie hoog, dan wordt de laag "polymeer-achtig". De brekingsindex krijgt dan een waarde van 1.5, de bandafstand een van 1.5 eV en de hardheid een van 5 GPa. Deze tendens lijkt er op te wijzen dat de groei van de laag in dit geval beheerst wordt door koolstofatomen en -ionen in plaats van, zoals dat bij conventionele processen het geval is, door radicalen, .

De bereikte groeisnelheden overtreffen de grootste tot nu toe in de literatuur gerapporteerde waarden (voor wat betreft amorfe koolstoflagen) met een factor 30. Concluderend kan men stellen dat de in dit proefschrift beschreven nieuwe methode voor plasmadepositie leidt tot een drastische verhoging van de depositiesnelheid terwijl de kwaliteit van de geproduceerde laag daar allerminst onder lijdt.

DANKWOORD

Dit proefschrift vormt de neerslag van een periode van bijna 5 jaar onderzoek. Als niet velen hun steentje zouden hebben bijgedragen zou het project "plasmadepositie" nooit zo succesvol hebben kunnen verlopen. Daarom wil ik hier iedereen bedanken die mij in de afgelopen 5 jaar heeft bijgestaan.

Allereerst natuurlijk de beide promotoren Daan Schram en Frits de Hoog. Daan Schram was degene die eind 1983 voorstelde naast de aanwezige etsreactor een depositie-experiment te starten. Ook heeft hij het idee geleverd om de zaak op deze onconventionele manier aan te pakken. De vele vruchtbare discussies die ik met hem heb gevoerd tijdens het onderzoek en tijdens het opzetten van de modellering hebben mij vaak van een dwaalspoor doen terugkeren. Ook heeft hij mij altijd gesteund als ik weer eens geld nodig had voor een uitbreiding van de opstelling of het diagnostiekenapparaat. In de laatste fase bestudeerde en becommentariëerde hij het geschrevene herhaaldelijk en zeer aandachtig. Voor dit alles mijn oprechte dank.

Frits de Hoog heeft waardevolle bijdragen geleverd bij de oriënterende studies die voorafgingen aan de implementatie van ellipsometrie. In een latere fase heeft hij veel werk verzet bij de interpretatie van de resultaten van deze methode. Bovendien heeft hij mij de vrijheid gegund mijn promotiewerk in het door mij gekozen tempo af te maken.

Bij de opbouw en het onderhoud van experiment en diagnostieken was de hulp van Ries van de Sande onmisbaar. Hij realiseerde altijd prompt en op een voortreffelijke wijze de meest extravagante wensen op technisch gebied. Zonder zijn niet aflatende inzet zou één en ander nooit zo (voor)spoedig zijn verlopen. De kwaliteit van het ontwerp van de reactor door Piet Magendans zorgde er onder meer voor dat er geen vertragingen ontstonden bij de start van de bouw. In dit verband wil ik ook Lambert Bisschops bedanken, die mijn ideeën voor de constructie van de cascadeboog uitwerkte en omzette in leesbare tekeningen. Ook John Bleize en Bertus Hüsken droegen hun steentje bij, ieder op hun eigen specialisme. De medewerkers van de afdelingswerkplaats waren altijd bereid mij snel te helpen, ook als de klus eigenlijk te omvangrijk was om als "klus" aan te merken. Hiervoor wil ik met name mijn erkentelijkheid betuigen aan Henk Heller, Marius Bogers, Henk van Helvoirt, Gerard Weijers, Rien de Koning, Frank van Hoof en Jan van Asten. Vrijwel alle geleidingen van de centrale technische dienst (CTD) waren betrokken bij de realisatie van experiment en diagnostieken.

Het gebruik van de computers bij de metingen werd mogelijk gemaakt door de hulp van de medewerkers van de onderwerpgroep FIV. Met name wil ik hier noemen Fred van Nijmegen, Jan Voskamp, Wijnand Dijkstra, Jos van Erum, Jeroen Lebbink en Arien van der Wal. Van de vakgroep Vaste Stof heeft Willem van der Vleuten mij meermaals geholpen te achterhalen welke verontreinigingen er op het oppervlak van de gedeponeerde lagen aanwezig waren. Bij de modellering van het plasma hebben de tips van Rini van Dongen mij flink verder geholpen. Van de faculteit Werktuigbouwkunde hebben Gijs van Liempd en prof. Klostermann de Vickers hardheidsmetingen ondersteund.

Ik heb het geluk gehad te mogen profiteren van de inspanningen van een aantal postdoc's. Lex Straaijer heeft veel explorerend werk gedaan bij het opstarten van zowel de *in situ*- als de spectroscopisch ellipsometer. Jos de Haas heeft gerekend en gemeten aan het boogplasma. Theo Bisschops heeft de hulpontlading geperfectioneerd. Ook een tweetal gasten uit het buitenland hebben een bijdrage geleverd. Holger Kersten verrichtte enthousiast metingen aan de temperatuurafhankelijkheid van de depositiesnelheid. Andrei Misiura maakte mij op zijn eigen wijze duidelijk dat de taak van een fysicus niet altijd gemakkelijk is.

Ook alle collega's van de groep Atoom- en Plasmafysica wil ik bedanken voor hun bijdragen. Ik wil hier speciaal Theo Bisschops noemen. Ik heb veel van hem geleerd over vacuüm- en electrotechniek.

Jacques Schmitt, Ramdane Benferhat, Jérôme Perrin en Bernard Drevillon van de École Polytechnique te Parijs hebben mij tijdens een aantal werkbezoeken ontvangen in hun laboratorium. Ik heb daar veel inspiratie opgedaan op het gebied van ellipsometrie.

Huib Schuurmans, At van der Scheer, Jan Werner en Henk Vasmel van het KSLA hebben tijdens enige perioden van intensieve samenwerking het toepassingsgebied van de reactor vergroot. Hun daadwerkelijke bijdrage heeft de instandhouding en uitbreiding van de infrastructuur van het lab vergemakkelijkt. Voor dit alles mijn hartelijke dank. Het KSLA als geheel wil ik bedanken voor het aan mij toekennen van de reisprijs 1986. Deze reis heeft mij in staat gesteld een conferentie in de USA bij te wonen en een tocht langs een aantal laboratoria te maken.

Een groot deel van de uitvoering van de diagnostieken dreef op de inspanningen van studenten. Ik ben in het bijzonder natuurlijk de afstudeerders dankbaar. Kees de Zeeuw heeft de *in situ* ellipsometer opgezet. Van zijn bijdragen aan de signaalverwerking worden nu nog dagelijks de vruchten geplukt. Arno Wilbers heeft een groot gedeelte van de in dit proefschrift gerapporteerde spectroscopische metingen

verricht. Menige figuur zal hem bekend voorkomen. Ton Broekhuizen studeerde af in Parijs. Zijn afstudeerverslag heeft sterk bijgedragen tot de begripsvorming omtrent foton-geïnduceerde depositie. Col Offermans heeft de infrarode straling die een cascadeboog uitzendt geanalyseerd.

Het aantal stagiairs en pré-stagiairs die een wezenlijke bijdrage hebben geleverd tot het welslagen van het geheel is groot geweest. In alfabetische volgorde luiden hun namen: Ton Broekhuizen, Peter van de Camp, Martijn Creuwels, Yves Creyghton, Guido Dalessi, Peter van den Donk, Frank Feij, Huub de Grefte, Fons Jansen, Hans Kuppens, André van Lammeren, Wilfried Liebrechts, Rob Miesen, Gijs Meeusen, Col Offermans, Peter van Oorschot, René Sanders, Frank Schnitzeler, Marcel Schröer, Erik Seelen, Camiel Severijns, George Sips, Martie Timmers en Frans van de Weijer. Als student-assistent hebben Kees de Zeeuw en Gijs Meeusen mij veel werk uit handen genomen. Ik wil hen allen hartelijk danken.

Voor wat betreft de totstandkoming van het proefschrift wil ik Ruth Gruyters bedanken voor het tekenen van de vele figuren. Bij de ingebruikname van de nieuwe tekstverwerker was de hulp van Bertus Hüsken onmisbaar.

CURRICULUM VITAE

10 mei 1958 geboren te Heerlen

- mei 1977 Diploma Atheneum-B (met lof), Eijkhagen College Schaesberg
- mei 1983 Doctoraal examen Technische Natuurkunde (met lof), afdeling der
 Technische Natuurkunde, Technische Hogeschool Eindhoven
- mei 1983 – december 1986: In dienst van de Stichting FOM als wetenschappelijk
 medewerker
- december 1986 – heden: Universitair docent, faculteit der Technische Natuurkunde,
 Technische Universiteit Eindhoven.

STELLINGEN

behorend bij het proefschrift
"Plasma deposition: investigations on a new approach"

door

Gerrit Kroesen

Eindhoven, 18 maart 1988

I

Het ruimtelijk scheiden van dissociatie en depositie biedt, in combinatie met het gebruik van een cascadeboog als dissociatief medium, de mogelijkheid om de depositiesnelheid te verhogen van gemiddeld 1 nm/s tot meer dan 200 nm/s terwijl de kwaliteit van de gedeponeerde laag minstens vergelijkbaar is met die van films welke met conventionele methoden zijn geproduceerd.

Dit proefschrift.

II

Het doorberekenen van de kosten van universitaire diensten zoals het Rekencentrum en de Centrale Technische Dienst aan de gebruikende groepen zal op den duur een herbezinning over de omvang en de taakstelling van deze diensten onvermijdelijk maken.

III

Bij de modellering van radio-frevente (RF) plasma's in CF_4 moet men de invloed van de aanwezigheid van negatieve ionen in beschouwing nemen.

*T. Akitsu, H. Matsuzawa en S. Suganomata,
proceedings ISPC-8, Tokio, Japan 1987, p. 215.*

IV

De reactor voor plasma depositie zoals deze in het bij deze stellingen behorende proefschrift wordt beschreven kan ook gebruikt worden voor het met hoge snelheid etsen van materialen.

V

Bij de modellering van plasma's die gebruikt worden bij thermisch spuiten wordt vaak ten onrechte aangenomen dat de druk in het plasma uniform is.

*D.C. Schram, P.H.M. Vaessen, L.U.E. Konings en G.M.W. Kroesen,
proceedings ISPC-7, Eindhoven, 1985, p. 794.*

VI

In-situ infra-rood ellipsometrie maakt het mogelijk om tijdens een ontladingspuls de laagdikte, het waterstofgehalte en de bindingshybridisatie van de amorfe, gehydrogeneerde koolstoflaag op de wanden van een fusiereactor te volgen en analyseren.

*J. Winter, H.G. Esser, F. Waelbroeck en P. Wienhold,
proceedings E-MRS meeting, Strasbourg, Frankrijk, 1987, p. 405.*

VII

De populatie-inversie van koolstofatomen in een expanderend argon/methaan plasma biedt mogelijkheden om een continue laser te construeren met een golflengte van 247.9 nm.

S.W. Bowen en C. Park, AIAA-journal 10(1972)522

VIII

Het feit dat een cascadeboog in het spectrale gebied van 1-10 μm binnen een openingshoek van 1/20 radiaal een lichtemissie heeft die 1 à 2 ordes groter is dan die van een standaard IR-bron maakt hem zeer geschikt als lichtbron voor Fourier-interferometrie en IR-ellipsometrie.

*N.J.F. Offermans, afstudeerverslag Technische Universiteit Eindhoven,
faculteit Technische Natuurkunde, februari 1988.*

IX

Binnen het kader van een algehele heroriëntatie op de orgelbouw in de 17^e en de 18^e eeuw worden de ergonomische verbeteringen aan de speeltafel die sinds die tijd zijn ingevoerd door veel tegenwoordige nederlandse orgelmakers weer verwijderd. Dit schiet, aangezien de genoemde heroriëntatie geïnitieerd is door overwegingen op het gebied van klankschoonheid en reproduceerbaarheid van de tractuur, zijn doel voorbij.

X

Gezien het zeer hoge niveau waarop de beste van de nederlandse amateur harmonie-orkesten musiceren zouden de schouwburgen en muziektheaters in overweging moeten nemen deze orkesten, naast de gebruikelijke regionale professionele symfonie-orkesten, in hun reguliere concertprogramma op te nemen.